The Dissertation Committee for David Thomas A. Fuentes
certifies that this is the approved version of the following dissertation:

Computational Modeling and Real-Time Control of Patient-Specific Laser Treatment of Prostate Cancer

Committee:

J. Tinsley Oden, Supervisor

Ivo Babuška

Leszek Demkowicz

Kenneth Diller

Omar Ghattas

Computational Modeling and Real-Time Control of Patient-Specific Laser Treatment of Prostate Cancer

by

David Thomas A. Fuentes, B.S., M.S.

DISSERTATION

Presented to the Faculty of the Graduate School of
The University of Texas at Austin
in Partial Fulfillment
of the Requirements
for the Degree of

DOCTOR OF PHILOSOPHY

THE UNIVERSITY OF TEXAS AT AUSTIN
May 2008

To my father and my mother
David and Norma Fuentes

Acknowledgments

First and foremost, I would like to thank my advisor and mentor, Dr. J. Tinsley Oden. He has provided an exceptional academic environment with great opportunities and was the catalyst for my growth as a researcher. I am deeply appreciative of his time spent guiding and motivating me along this intellectual journey. The many lessons I have learned from him will never be forgotten.

This work would not be possible if not for the many questions from everyone in the weekly DDDAS group meeting. I am very fortunate to have my committee members in attendance of the weekly meetings. The constant feedback was crucial to the progress made in this project. Dr. Omar Ghattas provided the initial spark for the solution method to problems of PDE constrained optimization. The insightful questions of Dr. Ivo Babuša constantly forced me to treat every aspect of the mathematical modeling of cancer treatment as a single entity. The coding foundations upon which every result of this dissertation was obtained was forged by the hands of Dr. Leszek Demkowicz. Dr. Kenneth Diller very patiently provided insight to my many questions on the subject of bioheat transfer. The many perceptive questions and comments by Dr. James Browne and Dr. Chandrajit Bajaj are also appreciated. The initial work of Dr. Yusheng Feng, Dr. Jon Bass, and Dr. Nichole Rylander provided the impetus for this dissertation.

I am also in deeply indebted to our colleagues at M.D. Anderson Cancer Center in Houston, Texas. The imaging expertise of Dr. John Hazle and Dr.

Jason Stafford, and Dr. Andrew Elliott's long hours in the M.D. Anderson laboratory were indispensable to this project. The experimental expertise of Dr. Anil Shetty of M.D. Anderson Cancer Center and Dr. Roger McNichols of BioTex Inc. was crucial to the success of the *in-vivo* experiments. I would also like to thank my office-mate Chetan Jhurani, I learned a great deal from his programming expertise. And finally, my dear friend and colleague Paul Bauman. His competitiveness, sense of humor, and good nature have made graduate school a truly memorable portion of my life.

The support of this research by the National Science Foundation under grant CNS-0540033, Dr. Frederica Darema, program director, is greatly appreciated.

Computational Modeling and Real-Time Control of Patient-Specific Laser Treatment of Prostate Cancer

Publication No. ________________

David Thomas A. Fuentes, Ph.D.
The University of Texas at Austin, 2008

Supervisor: J. Tinsley Oden

Hyperthermia based cancer treatments delivered under various modalities have the potential to become an effective option to eradicate the disease, maintain functionality of infected organs, and minimize complications and relapse. Moreover, hyperthermia therapies are a form of minimally invasive cancer treatment which are key to improving the quality of life post-treatment. Many modalities are available for delivering the heat source. However, the ability to control the energy deposition to prevent damage to adjacent healthy tissue is a limiting factor in all forms of thermal therapies, including cryotherapy, microwave, radio-frequency, ultrasound, and laser. The application of a laser heat source under the guidance of real-time treatment data has the potential to provide unprecedented control over the temperature field induced within the biological domain.

The computational infrastructure developed in this work combines a computational model of bioheat transfer based on a nonlinear version of the

Pennes equation for heterogeneous media with the precise timing and orchestration of the real-time solutions to the problems of calibration, optimal control, data transfer, registration, finite element mesh refinement, cellular damage prediction, and laser control; it is an example of Dynamic-Data-Driven Applications System (DDDAS) in which simulation models interact with measurement devices and assimilates data over a computational grid for the purpose of producing high-fidelity predictions of physical events. The tool controls the thermal source, provides a prediction of the entire outcome of the treatment and, using intra-operative data, updates itself to increase the accuracy of the prediction. A precise mathematical framework for the real-time finite element solution of the problems of calibration, optimal heat source control, and goal-oriented error estimation applied to the equations of bioheat transfer is presented. It is demonstrated that current finite element technology, parallel computer architecture, data transfer infrastructure, and thermal imaging modalities are capable of inducing a precise computer controlled temperature field within a biological domain. The project thus addresses a set of problems falling in the intersection of applied mathematics, imaging physics, computational science, computer science and visualizations, biomedical engineering, and medical science. The work involves contributions in the three component areas of the CAM program; A, Applicable Mathematics; B, Numerical Analysis and Scientific Computing; and C, Mathematical modeling and Applications. The ultimate goal of this research is to provide the medical community a minimally invasive clinical tool that uses predictive computational techniques to provide the optimal hyperthermia laser treatment procedure given real-time, patient specific data.

Table of Contents

List of Tables

List of Figures

Chapter 1

Introduction

The prostate, Figure 1.1, is a firm, partly muscular, partly glandular organ in males located in front of the rectum and beneath the bladder. The prostate is perforated by the urethra and ejaculatory ducts. The function of the prostate is to produce a fluid that provides a protective environment for the sperm in semen. The prostate is the region of the male anatomy that has the highest morbidity to developing cancer. According to the latest statistics of the American Cancer Society [8], estimates are that 218,890 new prostate cancer diagnoses occurred in 2007 (30% of all new cancer cases). Furthermore, it is estimated that there will be 27,050 prostate-cancer-related deaths in 2007, which is the third leading cause of cancer deaths in males (9% of all cancer related deaths). Survival of the patient with prostatic carcinoma is directly related to the extent of the tumor.

The medical community has classified the degree of the disease into four stages, Figure 1.1. Stage I and Stage II prostate cancer are identified by the cancerous cells being entirely contained within the prostatic capsule. The tumor spreads beyond the prostatic capsule and invades nearby tissue such as the seminal vesicles in Stage III. Advanced cases, Stage IV, of prostate cancer in which cancerous cells have metastasized to distant organs are not curable with current therapy. Even patients with locally advanced cancer, Stage III, are not usually curable, and a substantial fraction will eventually die of their tumor.

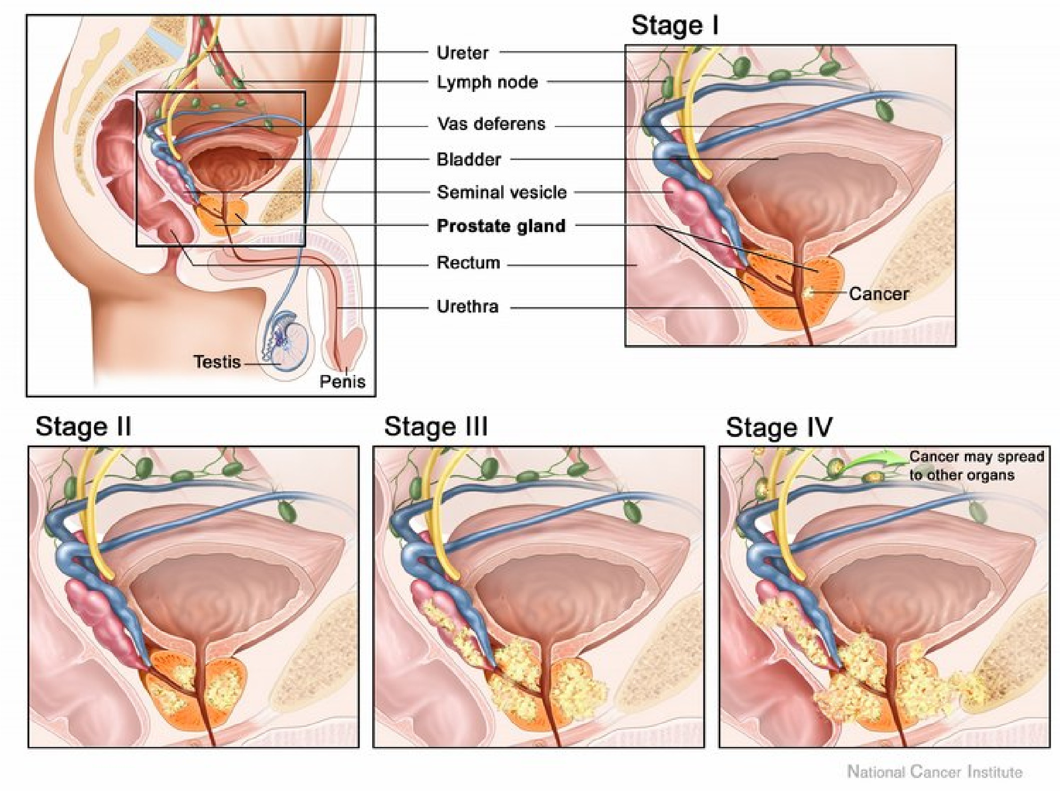

Figure 1.1: Stages of Prostate Cancer. Reproduced public domain image from National Cancer Institute [1]

Current detection technology is facilitating discovery of 90% of all prostate cancers in local and regional stages and statistics show that detection within these stages is enough to ensure a five year survival rate very close to 100% [8]. Given these survival rates, the quality of life of the patient post-treatment is a very important factor. Traditional medical treatment of early stage prostate cancer includes radical prostatectomy, removal of the prostate, and pelvic lymphadenectomy, removal of pelvic lymph nodes, which may or may not be followed by external radiation therapy or brachytherapy, interstitial implantation of radioactive material near cancerous cells. Surgery is typically reserved for healthy patients younger than 70 years of age because of expected surgical complications, which may include urinary incontinence, urethral stricture, impotence, and the morbidity associated with general anesthesia for major surgical procedures. Complications associated with radiation therapy include acute cystitis, (inflammation of the bladder) proctitis, (inflammation of the rectum) and sometimes enteritis (inflammation of the intestines).

Ablation therapies delivered under various treatment modalities are a very promising, minimally invasive, alternative to standard treatment and show significant potential to irradicate the disease with minimal impact, complications, and relapse. The physical basis, Figure 1.2, for thermal therapies is that exposing cells to temperatures outside their nature environment for certain periods of time can damage and even destroy the cells. However, one of the limiting factors in all forms of ablation therapy, including cryotherapy, microwave, radio-frequency, and laser, is the ability to control the energy deposition to prevent damage to the urethral, sphincter and neurovascular bundles [38].

This dissertation focuses on the development of an adaptive control system driven by the interaction of computer simulations of hyperthermic laser treatment therapies on living laboratory subjects and real time feedback of MRTI data. Recent advances in imaging technology allow the imaging of the geometry of tissue and an overlaying temperature field using MRI and new MRTI technology. MRI has the desirable properties of excellent soft-tissue contrast, the ability to provide fast, quantitative temperature imaging in a variety of tissues, and the capability of providing biologically relevant information regarding the extent of injury immediately following therapy [23].

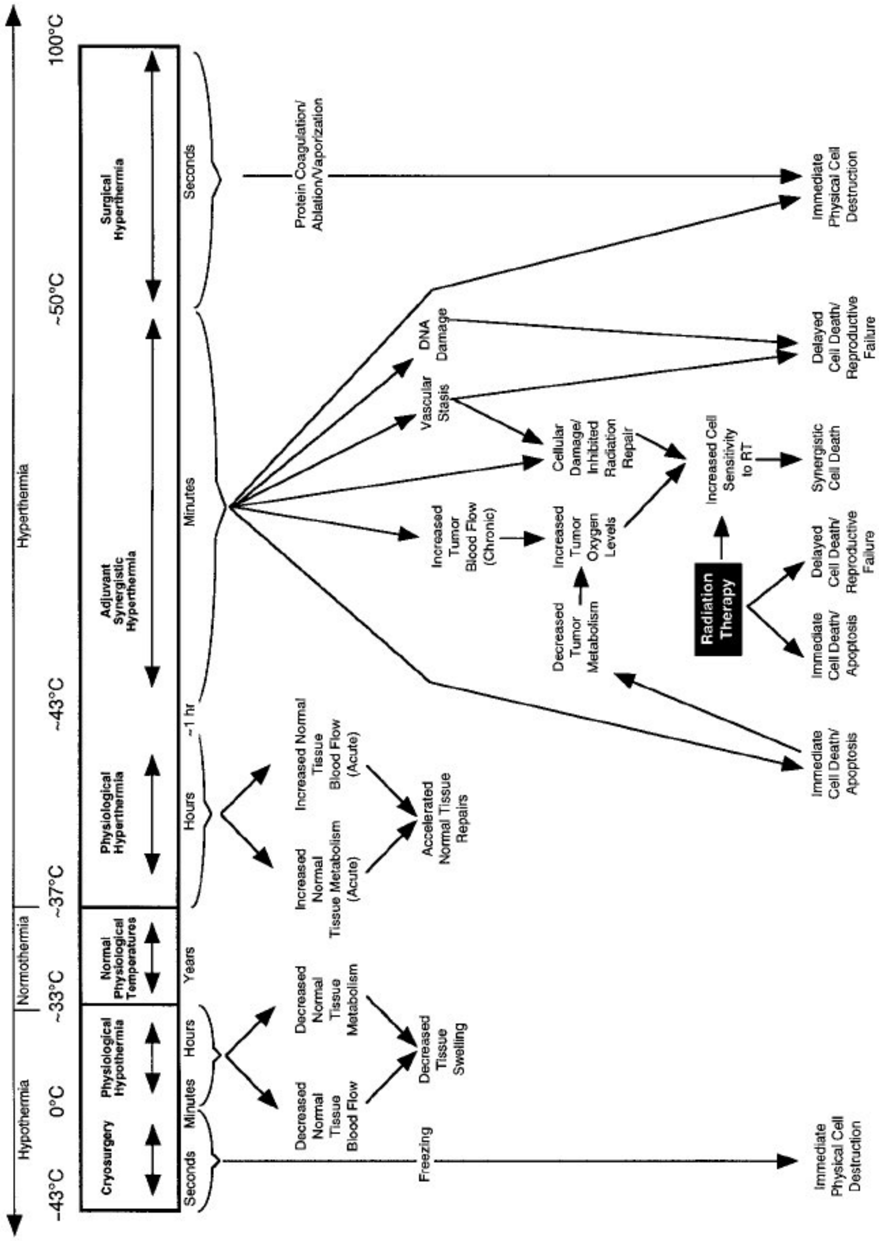

Figure 1.2: Cellular response to thermal stress [35]. Reprinted, with permission, from the Annual Review of Biomedical Engineering, Volume 1 (c)1999 by Annual Reviews www.annualreviews.org

Image guidance [37, 43] has the potential to facilitate unprecedented control over bioheat transfer by providing real time treatment monitoring through temperature feedback during treatment delivery. A similar idea using ultrasound guided cryotherapy has been studied and shows good results [38]. However, the hypothermic regime requires temperature differentials of 70^oK from normothermia to ablate the tissue, Figure 1.2. Tissue ablation in the hyperthermic regime requires substantially less energy deposition at differences of 10^oK, suggesting that MRTI guidance under laser therapy could provide superior control over the bioheat transfer.

In addition to ablation therapy, the ability to precisely predict and control the temperature field generated by a laser heat source within biological tissue would be highly desirable and enable the application of mild levels of hyperthermia. Such levels are also known [17] to sensitize the cells to subsequent treatments of radiation and chemotherapy. The inherent difficultly in predicting the outcome of laser treatment is further complicated by the expression of heat shock proteins (HSP), a latent defense mechanism built into all cells, including cancer cells. In regions of stress, such as that induced by the thermal laser source, heat shock proteins enhance cancer cell viability indirectly by preventing a damaged cell from going into apoptosis. Consequently, the combination of accurately predicting the bioheat transfer with the knowledge of the thermal dose necessary to deactivate HSP [36] expression in cancerous cells will drastically enhance the effectiveness of thermal treatment.

The final goal is to deliver a clinical tool that provides real-time high fidelity predictions of the bioheat transfer to be used concomitantly by the surgeon in the laser treatment processes. The target of this research is adenocarcinomas localized to the prostate, but as results will show, the procedures developed also have the potential to provide a viable option to treatment in other parts of the anatomy, including brain tissue and any tissue where an well-defined tumor mass has formed. This research also describes a potential option for patients with more advanced and aggressive forms of cancer who have reached their limit of radiation and chemotherapy treatment. More broadly, the methodologies developed here provides a special dynamic data-driven framework that brings together recent advances for controlling discretization and modeling errors through adaptive control strategies and the related methods of inverse analysis, calibration, uncertainty quantification, sensitivity analysis, and optimization [49, 31, 30, 33, 5, 27, 29, 28, 4, 7] into a single application. The evaluation of temperature fields in canine prostates is simulated using a nonlinear calibrated bioheat transfer model. A computational grid is developed that facilitates the transfer of MRTI data and FEM visualization data between M.D. Anderson in Houston and the Texas Advanced Computing Center in Austin. The three-dimensional finite element models of the prostate and time-varying thermal imaging data are used to generate images of the entire process. The computational models are used to simulate the treatment, predict outcomes, and control laser parameters to achieve the desired results.

1.1 Summary of Dissertation Results

The culminating goal of the thesis is to deliver a clinical tool that provides real-time high fidelity predictions and control over the bioheat transfer within the domain of interest. Towards this goal, a cyber-infrastructure has been created with the ability to control a laser treatment using high performance computers that are at a distance of 250 km apart from the laboratory.

A list of results attained while working towards this goal is given as follows.

1. The control system, in its entirety, must orchestrate the simultaneous solution of multiple optimization problems each with a different goal in mind. The different goals are embodied through different objective functions or quantities of interest. A precise discretization scheme has been developed to facilitate the solution of multiple optimization problems under a single mathematical framework.

2. A suite of parallel computing codes has been developed such that a root processor coordinates the simultaneous solution of multiple optimization problems. Each optimization problem is solved using an adjoint method within a parallel computing paradigm. The various optimization problems coded include calibration, temperature based optimal control, an Arrhenius damage model based optimal control, and a two-state damage model based optimal control. An adjoint method is also used to compute goal oriented error estimates.

3. During the solution process, the groups of multiple processors work together to solve the optimization problems of the control system. The groups have the ability to communicate solution information amongst each other as well as have the capability to update their computational model with newly acquired imaging data.

4. The treatment process heavily depends on the timing of data transfer of the thermal images as well as the timing of the data transfer of the laser controls. The timing algorithms and code has been verified on the computational grid consisting of the computers in the operating room at M.D. Anderson and TACC, the Texas Advanced Computing Center.

5. Raw thermal images from the MRI scanner are inherently noisy. A filtering pipeline consisting of a median and deriche filter has been implemented to remove the noise and smooth the data.

6. The final visualization of the control system consists of images of the FEM solution, the MRTI imaging, the optimal control parameters, damage, HSP expression, and cutlines to verify the FEM/MRTI temperature correlation. Portraying this multitude of information simultaneously requires significant computational power capable of rendering the data in real-time. For this purpose, a remote visualization scheme has been developed using the high performance visualization computers at TACC. Remote visualization removes the requirement of performance visualization hardware on the local graphics card. All rendering is done at TACC and remote visualization allows the transfer of merely the pixel information to the local computer within the operating room. Furthermore, inherent to the dynamic data driven scheme is uncertainty as to when the data will be available for visualization. Low level routines are written to check not only if the data is available but also if the complete data set is available to avoid reading in incomplete data in mid-transfer. The final visualization scheme remotely renders each individual data set when it is available.

7. Misalignment of the biological domain with the computational domain is unavoidable. A semi-automatic registration procedure has been developed to align the FEM mesh with intra-operative anatomical MRI data.

8. The ability for robust, efficient, real-time model calibration is demon-

strated. Results show that the accuracy of the calibration depends greatly on modeling the tissue heterogeneity within the patient specific biological domain and inversion for the constitutive nonlinearities. The tissue heterogeneity may be represented as a variation in the vasculature or the material thermal properties. Results also reinforce the experimentally observed phenomena of decreased perfusion in the damage region and hyper-perfusion surrounding the damage region.

9. Optimal laser control involves modulating the laser power as a function of time to maximize damage to a cancerous region while simultaneously minimizing damage to the surrounding healthy region. Time varying power functions have been computed that optimize the treatment delivery to impose a specified temperature or damage field.

This dissertation addresses all areas essential to modern work in Computational and Applied Mathematics. Area A, Applicable Mathematics; detailed mathematical analysis of the underlying models is presented, including existence of solutions of the nonlinear parabolic boundary-initial-value problem of bioheat transfer, optimal control algorithms, inverse analysis, proofs of convergence of discrete approximations and related issues. Area B, Numerical Analysis and Scientific Computing; an elaborate suite of parallel computing codes have been developed to implement nonlinear solvers of the governing partial differential equations, inverse analysis for the real-time calibration, use of imaging data for mesh generation, code verification and validation, and optimization algorithms for cell damage, HSP expression, and mesh adaptivity. Area C, Mathematical Modeling and Applications; extensive applications to modeling of bioheat transfer and laser therapies in various domains, including mice and canine specimens.

1.2 Outline

The governing equations used throughout the remainder of the thesis are discuss and developed in Chapter 2. A high level abstraction of the architecture and data flow of the control system is given in Chapter 3. The mathematical framework under which all optimization problems are solved is established in Chapter 4. Chapter 5 provides the major application results of the dissertation. Concluding remarks and future work are discussed Chapter 6.

Chapter 2

Bioheat Transfer

The equations of bioheat transfer are the governing equations used through out this dissertation. The field of bioheat transfer brings together elements of continuum mechanics, thermodynamics, anatomy, and physiology. Biological heat transfer includes conduction, convection, radiation, metabolism, evaporation, and phase change. However, the heat transfer between blood and tissue is the defining characteristic of biological heat transfer; as blood flows through the complex vasculature networks embedded in tissue, it may act as a significant heat source or heat sink.

The initial development of the equations of bioheat transfer accepted by the bioheat transfer community may be attributed to the work of Pennes [32] in 1948. The Pennes model attempts to describe bioheat transfer as the conservation of energy applied to a motionless non-deforming homogeneous mass of human tissue. The model does not allow mass flux across the boundary and assumes a uniform heat source based on the heat generated from the metabolic processes within the tissue and the perfusion of blood throughout the tissue. The Pennes model has been the subject of debate since its conception. It is a relatively simple model, easy to implement, and takes into account that the blood flow through tissue has a significant effect on the heat transfer. However, some argue that the blood perfusion term in Pennes equation is an adjustable parameter frequently chosen so that the predictions of the bioheat equation provide reasonable agreement with experimental measurement [44], thus allowing the flexibility of a curve-fit of the data without ever really testing fundamental hypotheses upon which the blood perfusion term rests. Moreover, the work of Chen and Holmes [13] shows that the fundamental assumptions of Pennes to be fundamentally flawed. Models [44, 22, 9] put forth after Pennes attempt to extend Pennes work by taking into account details of the vascular structure at the expense of substantially increasing the complexity of the

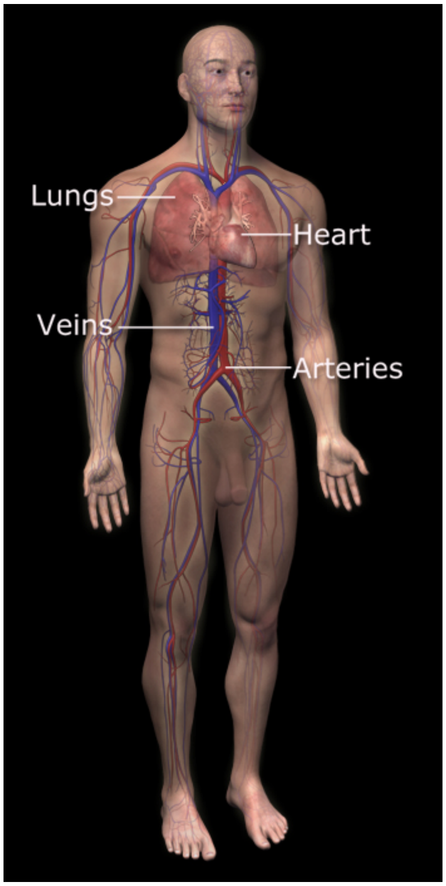

Figure 2.1: Schematic of cardiovascular system, www.3dscience.com. Reproduced under the Creative Commons Attribution 2.5 License.

model. Nevertheless, more recent work by Wissler [46] shows that much of the criticism directed to Pennes' model is not justified and after reworking Pennes' work demonstrates that "those who base their theoretical calculations on Pennes' model can be somewhat more confident that their starting equations are valid". Looking at the complex and irregular cellular structure of tissue one may wonder why the Pennes model produces such good results at the continuum level. The cellular structure of the tissue acts to create significant gradients in mass concentration, but not temperature gradients. One must recognize that, while cellular membranes act as barriers between certain molecules, they do not act as heat barriers. From the point of view of heat transfer, a specific tissue is a relatively homogeneous mixture composed mainly of proteins and water molecules in which the random motion of the molecules transfers heat. Before developing the Pennes model in detail, a brief review of the cardiovascular architecture is necessary to understand the modeling assumptions.

2.1 Background Physiology

A diagram of the cardiovascular system is shown in Figure 2.1. The cardiovascular system facilitates mass transport and heat transport within mammals. Mass transfer of O_2 and nutrients from the blood to surrounding tissue occurs only at the capillaries. However, heat transfer between the cardiovascular system and the tissue is not restricted and may occur anywhere. Figure 2.2 shows a schematic of the blood temperature distribution throughout the cardiovascular system as it enters tissue with either a lower or higher temperature. The cardiovascular system may be described as a plexus of branching countercurrent artery-vein pairs connected at the capillaries. Major arteries

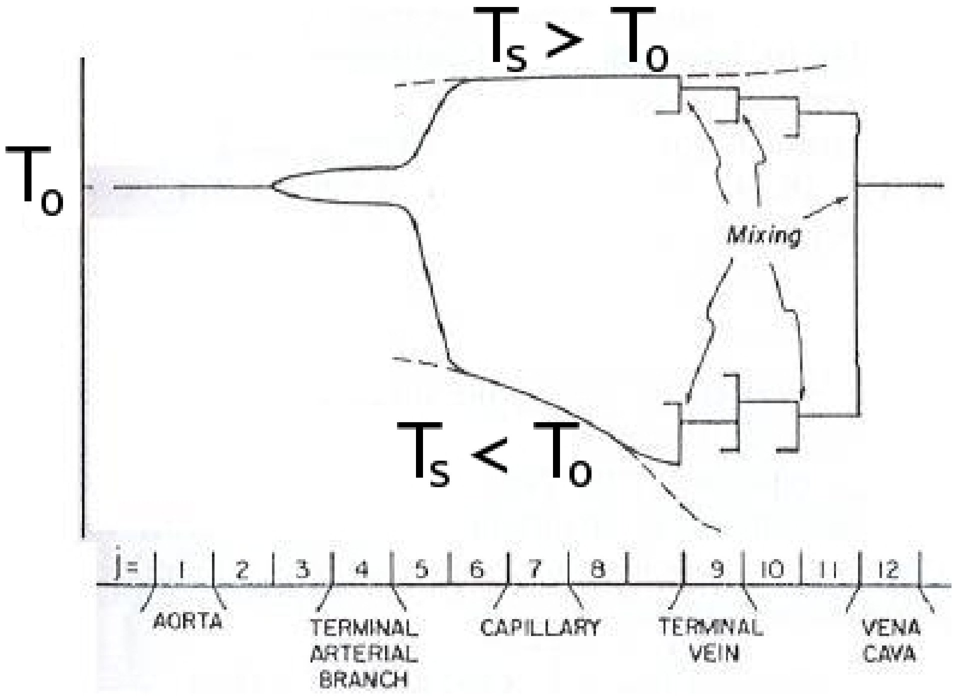

Figure 2.2: Schematic of blood temperature distribution within the circulatory system [11]. Reprinted, with permission, from Advances in Heat Transfer, www.elsevier.com Blood entering the aorta at the core body temperature T_o equilibriates with the tissue temperature at distant extremities, T_s, as shown.

and veins exist as countercurrent pairs. The countercurrent structure assists in the thermal regulation of the body by returning the heat to the inner core. The pairs branch 6-7 times before terminating at the equally spaced array of vessels that supply the capillary beds. Only in the last stages of branching does the countercurrent structure begin to disappear. As shown in Figure 2.2, for the situation such as tissue on the extremities, as the blood flows into the arterioles, the amount of smaller vessels and surface area of the vessels increases simultaneously as blood flow decreases setting in place ideal conditions for heat transfer between the blood and tissue. Numbers quantifying

Table 2.1: Anatomical dimensions of vessels in cardiovascular system [40]

	total cross-sectional area (cm^2)	velocity of blood flow (cm/s)	mean diameter	mean wall thickness
aorta	100	24	-	-
arteries	100 - 300	24 - 5	4.0 mm	1.0 mm
arterioles	300 - 4000	5 - 4	30.0 μm	6.0 μm
capillaries	4000 - 5000	4	8.0 μm	0.5 μm
venules	4500 - 2000	4	20.0 μm	1.0 μm
veins	2000 - 100	4 - 7	5.0 mm	0.5 mm
venae cavae	100	7 - 20	-	-

the extent of surface exchange area, blood flow velocity, and vessel diameter are given in Table 2.1. As an order of magnitude, the total capillary surface exchange area in normal adults is approximately 6300 m^2, roughly the surface area of two football fields. The length of capillaries is approximately 40,000 km or 25,000 miles, approximately the length of the earth's equator. Blood is known to be thermally equilibriated with surrounding tissue by the time it reaches the arterioles with a diameter of 60 μm.

2.2 An Overview of Models in Bioheat transfer

An ideal all-encompassing bioheat transfer model does not exist. Although bioheat transfer is generally understood as continuum mechanics applied to biological tissue, it is infinitely more than that.

The complexity of the microvascular architecture prevents an exact geometrical modeling of the biological domain. A true representation of the biological domain needs to begin at the cellular level. Figure 2.3 presents a various assemblies of specialized cells forming a different tissue types. Cells bind to other cells and the extracellular matrix through what are collectively known as cell junctions. Tissues are composed of billions of individual cells within the environment provided by the interstitial fluid and extracellular matrix. Different tissues are formed, Figure 2.3, through variations in the types of cells and extracellular matrix. Tissue regions are not solid. The human body is about 60% water by weight. Intracellular compartments contains 67% of the body's water and the remaining 33% of the water is divided between interstitial fluid approximately 3/4 of the extracellular water and plasma approximately one-fourth of the extracellular water. Interlaced throughout the tissue cells, interstitial fluid, and extracellular matrix are vessels of both the cardiovascular system and the lymphatic system, Figure 2.3. The average capillary density is $600/\text{mm}^3$, so it is not surprising that almost every cell in every tissue is located within 50-100 μm of the nearest capillary. Mass transfer across the boundary of the vessels is constantly occurring. Any attempt at exact geometrical modeling of this environment with current technology is futile.

Furthermore, the physiological control system that has evolved and is responsible for regulating the temperature of the human body though conduction, convection, radiation, metabolism, evaporation, and phase change is far more complex than the prediction capabilities of a thermo-mechanical continuum mechanics model. For example, skin receptors and receptors elsewhere in the body detect the body temperature. The temperature information is passed to the hypothalamus in the brain, which is responsible for maintaining the core body temperature.

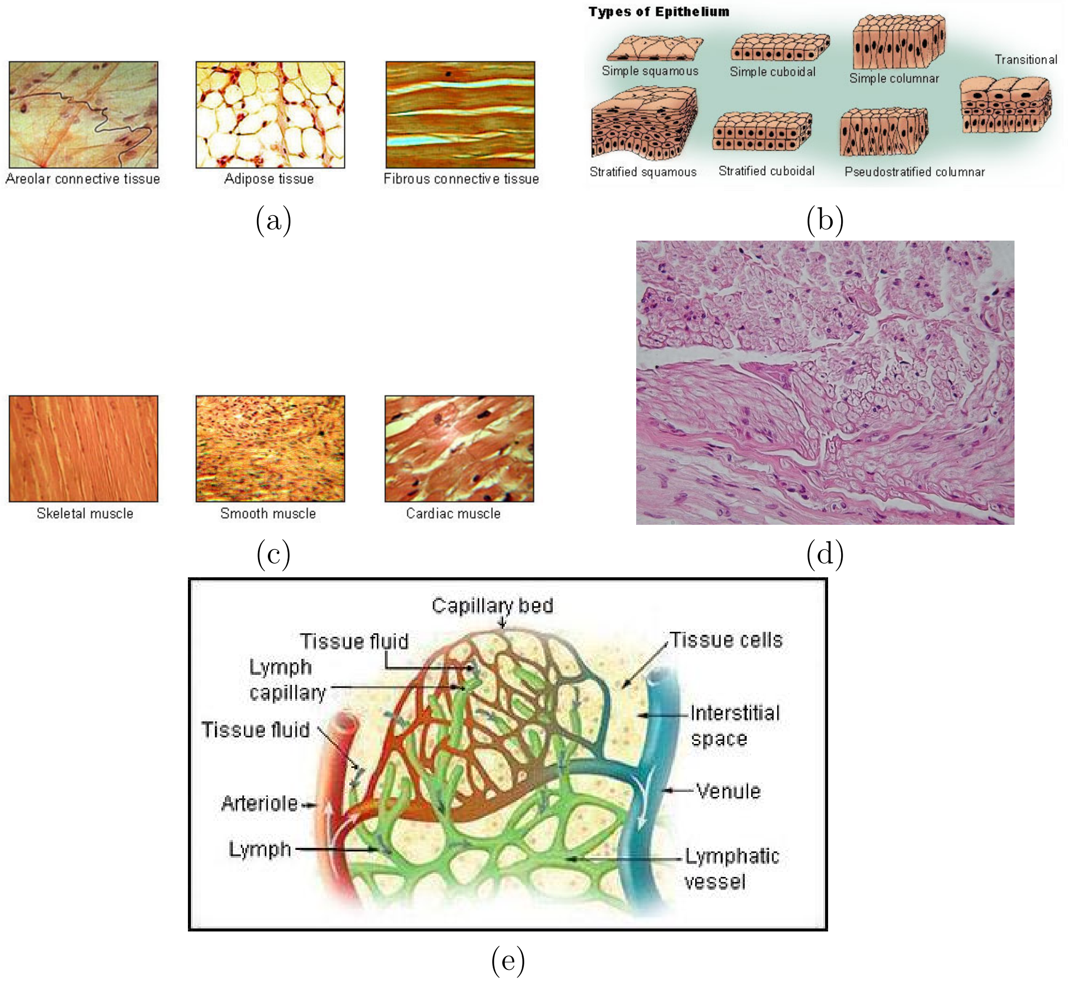

Figure 2.3: Specialized cells assemble through what are collectively known as cell junctions to form various tissue types. The four main tissue types are shown: (a) connective (b) epithelial (c) muscle (d) nervous. Vessels of the cardiovascular and lymphatic systems are interlaced throughout the tissue cells, interstitial fluid, and extracellular matrix, (e). (a), (b), and (c) are reproduced from Wikimedia Commons, a freely licensed media file repository. (d) is courtesy of the Department of Histology, Jagiellonian University Medical College and is reproduced under the GNU Free Documentation License. (e) is reproduced, with permission, from www.lymphnotes.com

If the hypothalamus determines that the temperature is too low, then messages are sent to contract the smooth muscles in the blood vessels near the skin (reducing blood flow and thus heat loss through the skin) and to skeletal muscles to start contracting rapidly to produce heat through shivering. On the other hand, if the temperature is too high, messages are sent to relax the smooth muscles in the blood vessels (allowing more blood flow and thus increase heat loss) and to sweat glands to release moisture to induce heat loss through evaporative cooling.

Thus, even if the precise vascular and microvascular architecture were known, and properly frame invariant, physically consistent constitutive equations, boundary conditions, and initial conditions are given; the conservation laws of continuum mechanics in their entirety (mass, momentum, energy, entropy) would still lack the ability to predict the action of electrical pulses sent from the brain to the tissue and the biochemical chain of reactions that they create. Nonetheless, there have been many proposed simplifications of the biological physiology including the models by Pennes [32], Klinger [24], Wulff [47], Chen-Holmes [13], Chato [12], Weinbaum-Jiji [44, 22]. A major flaw in quite a few bioheat transfer models [47, 24, 34] is that a prohibitively large amount of physiological detail, such as detailed accounts of the vasculature or unattainable amounts of material coefficients, needs to be known in order to computationally implement and attempt to validate these models. For completeness, an overview of computationally feasible bioheat transfer models is presented in Table 2.2. The models are divided into three classes: homogenized, porous media, and vasculature based. Remarkably, Pennes model is shown (Chapter 5) to be capable of producing very accurate predictions of the bioheat transfer. Only the Pennes model is studied in detail in this research.

Table 2.2: Overview of bioheat transfer models.

model type, assumptions, criticism, and applicability	
Homogenized (Pennes [32])	
Assumptions	*Criticism*
-single homogenized material -no rigid body motion -no deformation -no mass flux across boundary -blood perfusion acts as volumetric heating	-known that blood in thermal equilibrium in arterioles $\approx 60\ \mu$m -neglects convection effects -ignores countercurrent architecture -does not account for vascular geometry
Applicability: Porcine kidney cortex[48], rat liver[42], capillary bleed off[10]	
Porous Media Approach (Chen-Holmes [13])	
Assumptions	*Criticism*
-Partition Domains into two distinct sets, solid and fluid and assumes no mass transfer between the two -Develop conservation of energy for each domain based upon a defined average temperature	-known that blood in thermal equilibrium -averaging Process ignores vessels with diameter $\geq$ 1mm -ignores countercurrent architecture -convective terms present -increasing complexity to implement over Pennes model
Applicability: Essentially same as Pennes	
Vasculature Based Models (Weinbaum-Jiji[44, 22])	
Assumptions	*Criticism*
-three regions: major arteries, major veins, tissue -conservation of energy applied to each $\Rightarrow$ coupled system of equations	-accounts for countercurrent heat transfer -requires knowledge of vascular geometry to implement
Applicability: Peripheral muscle tissue of a limb [44]	

2.3 The Pennes Model

This section focuses on the complete derivation of the Pennes bioheat transfer equation modified to include a laser source term and heterogeneous nonlinear tissue properties. Consider a material body $\Omega \subset \mathbb{R}^3$. The time span of interested is denoted $(0,T]$ and the space-time domain is denoted $\Omega_T \equiv \Omega \times (0,T]$. The biological domain Ω is assumed to be a Lipschitz domain to provide meaning to the trace of the functions defined in the variational problem. The integral equations for conservation of energy are now invoked under the following assumptions:

- no mass flux across boundary, $\partial\Omega$
- no motion, deformation, or applied forces
- muscle, fat blood, etc. is represented as a single homogenized tissue that may have spatially varying properties.
- the presence of the blood within the homogenized tissue acts as a volumetric heating term at every point within the body Ω
- laser heating acts as a spatially and time varying heat source term

Note that the conservation of mass and momentum are identically satisfied under the first two assumptions. In words, the conservation of energy states that the change of energy within an arbitrary subvolume of the body, $\hat{\omega} \subset \Omega$, is equal to the energy lost across the boundary, $\partial\hat{\omega}$, plus energy generated within the body, Figure 2.4.

$$\frac{d}{dt}\int_{\hat{\omega}} \rho e \, dx = -\int_{\partial\hat{\omega}} \mathbf{q}\cdot\mathbf{n} \, dA + \int_{\hat{\omega}} Q_{blood} + Q_{laser} \, dx \tag{2.1}$$

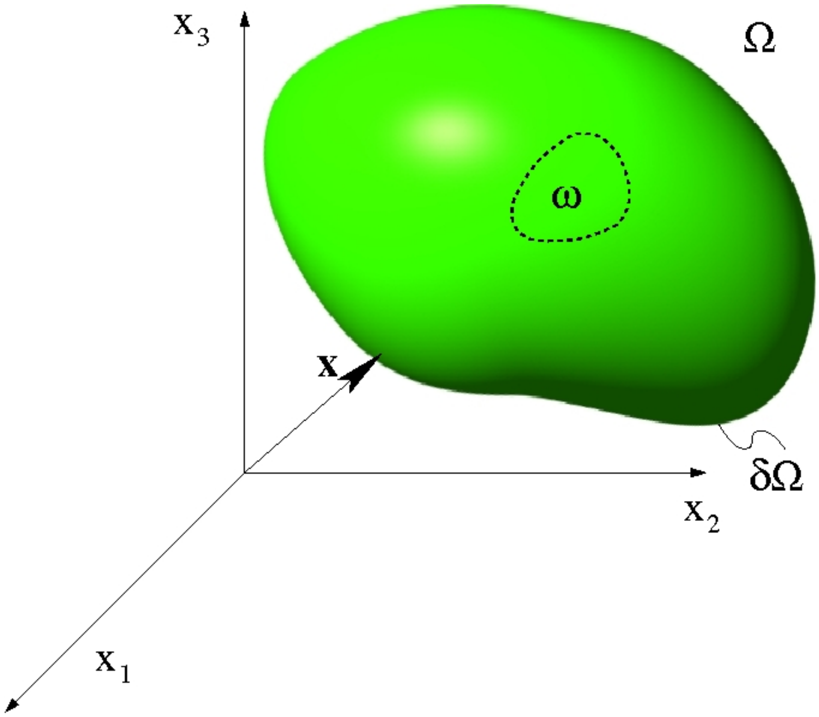

Figure 2.4: The equations of bioheat transfer are derived from the conservation of energy applied to an arbitrary subvolume

where Q_{blood} is the volumetric heating due to blood perfusion in the tissue and Q_{laser} is the volumetric heating of the laser source term. The density is denoted ρ, e is the internal energy, and $\mathbf{q}$ is the heat flux.

Integrals in (2.1) may be simplified as follows.

$$\Omega \text{ fixed}, \qquad \rho = \rho(\mathbf{x}) \qquad \Rightarrow \frac{d}{dt}\int_{\hat{\omega}} \rho e \, dx = \int_{\hat{\omega}} \rho \frac{\partial e}{\partial t} \, dx$$

$$\text{Divergence theorem} \qquad \Rightarrow \int_{\partial\hat{\omega}} \mathbf{q} \cdot \mathbf{n} \, dA = \int_{\hat{\omega}} \nabla \cdot \mathbf{q} \, dx$$

Since $\hat{\omega}$ is arbitrary, this implies that the local form of the principle of conservation of energy is

$$\rho \frac{\partial e}{\partial t} = -\nabla \cdot \mathbf{q} + Q_{blood} + Q_{laser} \qquad \text{a.e. in } \Omega$$

For the constitutive equations take

- $e = c_p\, u(\mathbf{x},t)$, where c is the specific heat $\left[\frac{J}{kg\,K}\right]$ and $u(\mathbf{x},t)$ denotes the temperature of the homogenized tissue at point $\mathbf{x} \in \bar{\Omega}$ at time t. Since there is no deformation the material may be considered incompressible and the specific heat at constant pressure is the same as the specific heat at constant volume. The constitutive equation follows from the definition of the specific heat $c_p = \frac{\partial e}{\partial u}\big|_p$
- $q = -k(u,\mathbf{x})\nabla u$, where $k(u,\mathbf{x})$ is the scalar coefficient of thermal conductivity. Assume a non-linear form for, $k\left[\frac{J}{s\cdot m\cdot K}\right]$, as shown in Figure 2.5.

  $$k(u,\mathbf{x}) = k_0(\mathbf{x}) + k_1\ \text{atan}(\tilde{k}_2(u - \hat{k}_3))$$

  where $k_0(\mathbf{x})\left[\frac{J}{s\cdot m\cdot K}\right]$, $k_1\left[\frac{J}{s\cdot m\cdot K}\right]$, $\tilde{k}_2\left[\frac{1}{K}\right]$, $\hat{k}_3\,[K] \in \mathbb{R}$. $k_0(\mathbf{x})$ is allowed to vary over the spatial dimension to capture the biological tissue heterogeneity. The media is thus assumed to be thermally isotropic (referring to heat flux) but spatially heterogeneous.

For the volumetric heating terms:

- The scattering and absorption of photons is the fundamental mechanism of heat transfer for the laser source term. The following form of the laser source term may be derived from transport theory using the diffusion approximation [45].

  $$Q_{laser}(\mathbf{x},t) = 3P(t)\mu_a\mu_{tr}\frac{\exp(-\mu_{eff}\|\mathbf{x}-\mathbf{x}_0\|)}{4\pi\|\mathbf{x}-\mathbf{x}_0\|}$$

  $$\mu_{tr} = \mu_a + \mu_s(1-g) \qquad \mu_{eff} = \sqrt{3\mu_a\mu_{tr}}$$

$P(t)$ is the laser power as a function of time, μ_a and μ_s are laser coefficients related to laser wavelength and give probability of absorption and scattering of photons, respectively. The anisotropic factor is denoted g and $\mathbf{x}_0$ denotes the position of laser photon source.

- Assume, as Pennes did in his original work in 1948, that arterial blood acts as a heat source and blood is isothermal until it reaches the capillaries with a diameter of $\approx 8\ \mu$m. Figure 2.2 shows a schematic of the blood temperature distribution in the circulatory system. As shown, blood is equilibriated with surrounding tissue by the time it reaches arterioles with diameters $\approx 60\ \mu$m, but we will use the assumption of Pennes irregardless.

  The volumetric heating of the tissue by perfused blood is driven by mass flow of blood to tissue and the temperature difference between arterial temperature, $u_a\,[K]$, and local homogenized tissue temperature, $u\,[K]$.

$$Q_{blood} = -\omega c_{blood}(u - u_a)$$

  where $\omega\left[\frac{kg}{s\ m^3}\right]$ is the perfusion coefficient. Perfusion has units of mass flow (of blood to tissue) per unit volume of tissue. Empirical evidence suggests that $\omega\left[\frac{kg}{s\ m^3}\right]$, is a smooth, monotone increasing bounded function of temperature, Figure 2.5.

$$\omega(u, \mathbf{x}) = \omega_0(\mathbf{x}) + \omega_1 \ \mathrm{atan}(\tilde{\omega}_2(u - \hat{\omega}_3))$$

  where $\omega_0\left[\frac{kg}{s\ m^3}\right]$, $\omega_1\left[\frac{kg}{s\ m^3}\right]$, $\tilde{\omega}_2\left[\frac{1}{K}\right]$, $\hat{\omega}_3\,[K] \in \mathbb{R}$. Note that $\omega_0(\mathbf{x})$ is allowed to vary over the spatial dimension as the blood perfusion within the necrotic core of a cancerous tumor or the blood perfusion within a damaged tissue is expected to be significantly lower than the surrounding healthy tissue. The specific heat of blood is denoted $c_{blood}\left[\frac{J}{kg\cdot K}\right]$

Let β denote an array of all the bioheat transfer model parameters,

$$\boxed{\beta \equiv (k_0(\mathbf{x}), k_1, \tilde{k}_3, \hat{k}_3, \omega_0(\mathbf{x}), \omega_1, \tilde{\omega}_3, \hat{\omega}_3, P(t), \mu_a, \mu_s, \mathbf{x}_0)}$$

Combining all terms, the problem statement is as follows:

Given a set of bioheat transfer model parameters, β,

$$\boxed{\beta \equiv (k_0(\mathbf{x}), k_1, \tilde{k}_3, \hat{k}_3, \omega_0(\mathbf{x}), \omega_1, \tilde{\omega}_3, \hat{\omega}_3, P(t), \mu_a, \mu_s, \mathbf{x}_0)}$$

find the spatially and temporally varying temperature field $u(\beta, \mathbf{x}, t)$ such that

$$\begin{aligned} &\rho c_p \frac{\partial u}{\partial t} - \nabla \cdot (k(u, \mathbf{x}, \beta) \nabla u) \\ &+ \omega(u, \mathbf{x}, \beta) c_{blood}(u - u_a) = Q_{laser}(\beta, \mathbf{x}, t) \quad \text{in } \Omega \end{aligned} \tag{2.2}$$

given the Cauchy and Neumann boundary conditions

$$-k(u, \mathbf{x}, \beta) \nabla u \cdot \mathbf{n} = h(u - u_\infty) \qquad \text{on } \partial\Omega_C$$

$$-k(u, \mathbf{x}, \beta) \nabla u \cdot \mathbf{n} = \mathcal{G} \qquad \text{on } \partial\Omega_N$$

and the initial condition

$$u(\mathbf{x}, 0) = u^0 \qquad \text{in } \Omega$$

The domains of the Cauchy and Neumann boundary conditions satisfy

$$\partial\Omega = \partial\Omega_C \,\bar{\cup}\, \partial\Omega_N \qquad\qquad \partial\Omega_C \cap \partial\Omega_N = \emptyset$$

On the Cauchy boundary, h is the coefficient of cooling and u_∞ is the ambient temperature. The prescribed heat flux on the Neumann boundary is denoted $\mathcal{G}$. Notice the explicit dependence of thermal conductivity, $k(u, \mathbf{x}, \beta)$, perfusion, $\omega(u, \mathbf{x}, \beta)$, and laser source, $Q_{laser}(\beta, \mathbf{x}, t)$, on β. A summary of the nomenclature used throughout the remainder of this dissertation is given in Table 2.3.

Table 2.3: Nomenclature.

u = temperature	h = coefficient of cooling	c_p = tissue specific heat
ω = blood perfusion	k = thermal conductivity	c_{blood} = blood specific heat
ρ = tissue density	u_∞ = ambient temperature	Q_{laser} = laser source term

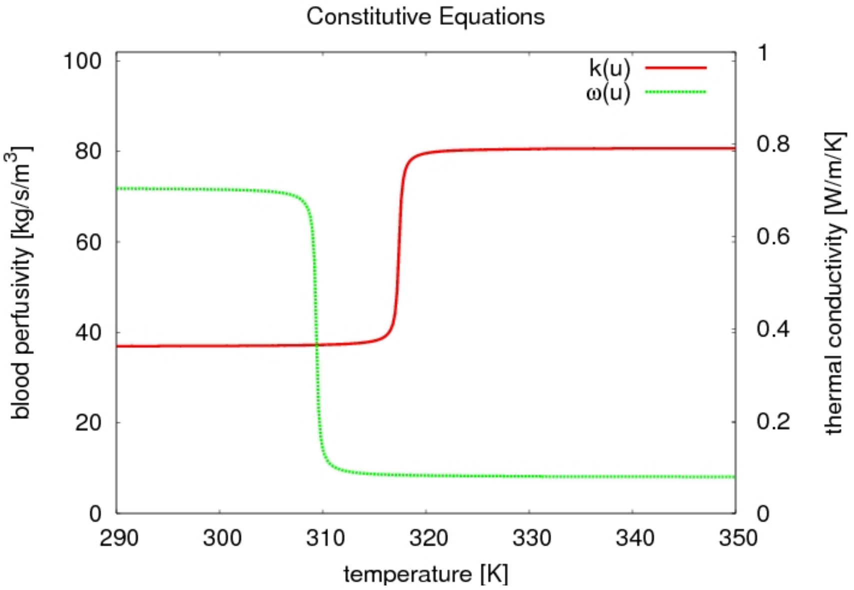

Figure 2.5: Typical temperature dependencies of the blood perfusion and thermal conductivity material data used in the Pennes model are plotted against the left and right axis, respectively.

Typical values of the parameters appearing in the Pennes model obtained by Rylander [36] are given in Tables 2.4 and 2.5. Later, these parameters will be determined from real-time thermal MRTI data using calibration methods based on inverse analysis.

Table 2.4: Model Coefficients (From Rylander [36])

Laser Wavelength	810 nm	ρ_{tissue}	1045 $\frac{kg}{m^3}$
μ_s	14.74cm	ρ_{blood}	1058 $\frac{kg}{m^3}$
μ_a	0.046 cm	c_p^{tissue}	3600 $\frac{J}{kg \cdot K}$
u_a	310 K	c_p^{blood}	3840 $\frac{J}{kg \cdot K}$

2.3.1 Variational Form of the Pennes Model

A variational method is used to weaken the regularity requirements on the solution and search for the solution in a broader space of functions. In order to do this, the sense in which the equality in (2.2) holds must be reinterpreted.

A space-time formulation is developed in anticipation of the dual/adjoint formulation used in the optimization process. As will be seen, the space of test functions will be the same space of the adjoint solution, and a variational formulation is sought in which the space of the trial and test functions are identical. Proceeding formally, one multiplies the Pennes equation by a *smooth space-time* test function, $v(\mathbf{x}, t)$, and integrates over Ω and $(0, T)$. Using the Gauss' theorem,

$$\int_\Omega -\nabla \cdot (k(u, \mathbf{x}, \beta) \nabla u) v \; dx = \int_\Omega k(u, \mathbf{x}, \beta) \nabla u \cdot \nabla v \; dx - \int_{\partial\Omega} k(u, \mathbf{x}, \beta) \nabla u \cdot \mathbf{n} v \; dx$$

and applying the boundary conditions, the structure of the variational problem

Table 2.5: Model Coefficients

$k(u) = k_0 + k_1 \cdot \text{atan}(k_2(u - k_3))$		$\omega(u) = \omega_0 + \omega_1 \cdot \text{atan}(\omega_2(u - \omega_3))$	
k_0	$0.6489 \left[\frac{J}{s \cdot m \cdot K}\right]$	ω_0	$0.6267 \left[\frac{kg}{s\ m^3}\right]$
k_1	$0.0427 \left[\frac{J}{s \cdot m \cdot K}\right]$	ω_1	$-0.137 \left[\frac{kg}{s\ m^3}\right]$
k_2	$0.02529 \left[\frac{1}{K}\right]$	ω_2	$2.35893 \left[\frac{1}{K}\right]$
k_3	$315.314\,[K]$	ω_3	$314.262\,[K]$

is as follows:

$$\begin{aligned}\int_0^T \int_\Omega \rho c_p \frac{\partial u}{\partial t}\ v\ dx &+ \int_0^T \int_\Omega \omega(u, \mathbf{x}, \beta) c_{blood}(u - u_a)\ v\ dx \\ &+ \int_0^T \int_\Omega k(u, \mathbf{x}, \beta) \nabla u \cdot \nabla v\ dx + \int_0^T \int_{\partial\Omega_C} h(u - u_\infty)\ v\ dx \\ &= \int_0^T \int_\Omega Q_{laser}(\beta, \mathbf{x}, t) v\ dx - \int_0^T \int_{\partial\Omega_N} \mathcal{G}\ v\ dA\end{aligned} \tag{2.3}$$

Sufficient regularity has been tacitly assumed to justify the above computations. To provide a precise mathematical meaning to the variational problem, the proper setting in which each of the integrals in (2.3) holds must be determined.

Given the assumptions on the thermal conductivity $k(u, \mathbf{x}, \beta)$ and the perfusion $\omega(u, \mathbf{x}, \beta)$, the corresponding integrals involving these terms are well defined provided that $u, v \in H^1(\Omega)$ for a.e. $t \in (0, T]$. Here, $H^1(\Omega)$ is the classical Sobolev space of the equivalence class of $L_2(\Omega)$ functions whose distributional derivatives also belong to the equivalence class of $L_2(\Omega)$ functions.

$$H^1(\Omega) \equiv \left\{ f \in L_2(\Omega) : \frac{\partial f}{\partial x_i} \in L_2(\Omega) \text{ for } i = 1,2,3 \right\}$$

More precisely, interpreting u, v as mappings from the time domain to the appropriate function space

$$u(\mathbf{x},t) \equiv (u(t))(\mathbf{x}) : (0,T) \to H^1(\Omega) \qquad\qquad v(\mathbf{x},t) \equiv (v(t))(\mathbf{x}) : (0,T) \to H^1(\Omega)$$

the integrals involving the thermal conductivity and perfusion in (2.3) are well defined. The appropriate space containing such mappings is defined below.

Definition 2.3.1.

$$\boxed{\mathcal{V} \equiv L_2\left(0,T; H^1(\Omega)\right)}$$

where $u \in L_2\left(0,T; H^1(\Omega)\right) \Rightarrow$

- u is a mapping from the time domain to the spatial domain,

$$u : (0,T) \to H^1(\Omega)$$

- the H^1 norm of u is L_2 integrable in time,

$$\int_0^T \|u(\cdot,t)\|_{H^1}^2 dt < \infty$$

A precise form of (2.3) also requires that the laser source term, Q_{laser}, and the time derivative of the solution, $\frac{\partial u}{\partial t}$, exist in the dual space of the test functions.

$$Q_{laser}, \frac{\partial u}{\partial t} \in \mathcal{V}' = \left(L_2(0,T; H^1(\Omega))\right)' = L_2\left(0,T; (H^1(\Omega))'\right)$$

To be precise,

$$h \in \left(L_2(0,T;H^1(\Omega))\right)' \Rightarrow \exists g \in L_2(0,T;(H^1(\Omega))') :$$

$$, \qquad < h, y >= \int_0^T < g(t), y(t) >_{(H^1(\Omega))' \times H^1(\Omega)} \; dt \qquad y \in L_2(0,T;H^1(\Omega)) \tag{2.4}$$

and the derivative $\frac{\partial u}{\partial t}$ is understood in the sense of distributions. Finally, the boundary terms in (2.3) are well defined provided $\mathcal{G} \in (H^{\frac{1}{2}}(\partial\Omega))'$ and the values of the solution and test function are interpreted in the trace sense.

$$\begin{aligned}\left|\int_{\partial\Omega} \gamma u \; \gamma v \; dx\right| \leq \|\gamma u\|_{L_2(\partial\Omega)} \|\gamma v\|_{L_2(\partial\Omega)} &\leq \|\gamma u\|_{H^{\frac{1}{2}}(\partial\Omega)} \|\gamma v\|_{H^{\frac{1}{2}}(\partial\Omega)} \\ &\leq C\|u\|_{H^1(\Omega)} \|v\|_{H^1(\Omega)}\end{aligned}$$

where $\gamma : H^1(\Omega) \rightarrow H^{\frac{1}{2}}(\partial\Omega)$ is the trace operator.

The variational problem may now be stated.

$$\boxed{\begin{aligned}&\text{Given a set of model parameters, } \beta \text{, find} \\ &\quad u(\mathbf{x},t) \in \mathcal{V} \text{ with } \frac{\partial u}{\partial t} \in \mathcal{V}' : \\ &\qquad \rho c_p \frac{\partial u}{\partial t}(\mathbf{x},t) + \mathcal{A}(\beta) u(\mathbf{x},t) = \mathcal{F}(\beta) \in \mathcal{V}' \\ &\qquad\quad u(\mathbf{x},0) = u^0\end{aligned}} \tag{2.5}$$

where $\mathcal{A} : \mathcal{V} \rightarrow \mathcal{V}'$ and denoting the duality pairing by $< \cdot, \cdot >_{\mathcal{V}' \times \mathcal{V}}$,

$$\begin{aligned}\langle \mathcal{A}(\beta) u(\mathbf{x},t), v \rangle_{\mathcal{V}' \times \mathcal{V}} = &\int_0^T \int_\Omega \left[k(u,\mathbf{x},\beta) \nabla u \cdot \nabla v + \omega(u,\mathbf{x},\beta) c_{blood} u \; v \; \right] dx dt \\ &+ \int_0^T \int_{\partial\Omega_C} h u \; v \; dA dt\end{aligned} \tag{2.6}$$

and

$$\begin{aligned}\langle \mathcal{F}(\beta), v \rangle_{V' \times V} = &\int_0^T \int_\Omega Q_{laser}(\beta, \mathbf{x}, t) v \; dx dt + \int_0^T \int_{\partial\Omega_C} h u_\infty \; v \; dA dt \\ &+ \int_0^T \int_\Omega \omega(u,\mathbf{x},\beta) c_{blood} u_a \; v \; dx dt - \int_0^T \int_{\partial\Omega_N} \mathcal{G} \; v \; dA\end{aligned} \tag{2.7}$$

As is typical for a function defined in $L_2(0,T)$, we have the right to speak of a function $L_2\left(0,T;H^1(\Omega)\right)$ only for a.e. $t \in (0,T]$. However, important calculus results [39] on the space $L_2\left(0,T;H^1(\Omega)\right)$, with time derivatives in $L_2\left(0,T;(H^1(\Omega))'\right)$ justify the right to speak of the solution point-wise in time so that the initial condition $u(x,0)=u^0$ is well-defined.

The theory on parabolic equations as found in Showalter [39] provides conditions under which (2.5) may be shown to have a solution. In particular, if the operator $\mathcal{A}:\mathcal{V}\rightarrow\mathcal{V}'$ is

- bounded, i.e. $\exists\ C$ s.t.

$$\|\mathcal{A}u\|_{\mathcal{V}'} \leq C\ \|u\|_{\mathcal{V}} \qquad \forall u\in\mathcal{V}$$

- coercive: $\exists\ \alpha>0$ s.t.

$$\langle\mathcal{A}v,v\rangle_{\mathcal{V}'\times\mathcal{V}} \geq \alpha\ \|u\|_{\mathcal{V}}^2 \qquad \forall v\in\mathcal{V}$$

- type $\mathcal{M}$:

$$u_n \rightharpoonup u, Au_n \rightharpoonup f,\ \lim\sup A(u_n)u_n \leq f(u) \qquad \Rightarrow \qquad Au=f$$

then (2.5) has a solution [39]. Coercivity may be shown from the realistic assumptions that thermal conductivity, perfusion, and coefficient of cooling are bounded away from zero.

$$\begin{aligned}\langle\mathcal{A}(v),v\rangle_{\mathcal{V}'\times\mathcal{V}} = \int_0^T\int_\Omega & [k(v,\mathbf{x},\beta)\nabla v\cdot\nabla v+\omega(v,\mathbf{x},\beta)c_{blood}v\ v\ ]\,dxdt \\ & \qquad\qquad + \int_0^T\int_{\partial\Omega_C} hv\ v\ dAdt \\ \geq & \int_0^T k_*\|\nabla v\|_{L_2(\Omega)}^2\ dt + \int_0^T \omega_* c_{blood}\|v\|_{L_2(\Omega)}^2\ dt \\ \geq & \min(k_*,\omega_*)\|v\|_{\mathcal{V}}^2\end{aligned}$$

where positivity of the boundary integral was used and k_* and ω_* denote bounds on the thermal conductivity and perfusion.

$$0 < k_* < k(u, \mathbf{x}, \beta) \qquad 0 < \omega_* < \omega(u, \mathbf{x}, \beta)$$

Upper bounds on the thermal conductivity and perfusion

$$k(u, \mathbf{x}, \beta) < k^* < \infty \qquad \omega(u, \mathbf{x}, \beta) < \omega^* < \infty$$

may be used to show boundedness. Using Hölder's inequality and rearranging

$$\forall u, v \qquad \frac{\left|\langle \mathcal{A}(u), v \rangle_{\mathcal{V}' \times \mathcal{V}}\right|}{\|v\|_{\mathcal{V}}} \leq \max(k^*, \omega^*) \|u\|_{\mathcal{V}}$$

Thus, $\max(k^*, \omega^*)\|u\|_{\mathcal{V}}$ is an upper bound of $\frac{\left|\langle \mathcal{A}(u), v \rangle_{\mathcal{V}' \times \mathcal{V}}\right|}{\|v\|_{\mathcal{V}}}$ for all v. The supremum is the least upper bound which implies that

$$\sup_{v \in \mathcal{V}, v \neq 0} \frac{\left|\langle \mathcal{A}(u), v \rangle_{\mathcal{V}' \times \mathcal{V}}\right|}{\|v\|_{\mathcal{V}}} = \|\mathcal{A}u\|_{\mathcal{V}'} \leq \max(k^*, \omega^*) \|u\|_{\mathcal{V}} \qquad \forall u$$

The Lipschitz continuity of the constitutive equations and a generalization of the Rellich-Kondrachov theorem to the space $\mathcal{V}$

$$u_n \overset{L_2\left(0,T;H^1(\Omega)\right)}{\rightharpoonup} u \qquad \Rightarrow \qquad u_n \overset{L_2(0,T;L_2(\Omega))}{\rightarrow} u \tag{2.8}$$

may be used to show that the operator $\mathcal{A} : \mathcal{V} \rightarrow \mathcal{V}'$ is weakly closed

$$u_n \rightharpoonup u, \mathcal{A}u_n \rightharpoonup f \qquad \Rightarrow \qquad \mathcal{A}u = f$$

and, hence, is of type $\mathcal{M}$. Weak convergence of space-time functions in $\mathcal{V}$ is a straight forward generalization of the classical theory on the domain Ω.

$$u_n \overset{\mathcal{V}}{\rightharpoonup} u \Longleftrightarrow \left| \int_0^T \int_\Omega \left((u - u_n) \, v \; + \nabla(u - u_n) \cdot \nabla v \right) dx dt \right| \rightarrow 0 \qquad \forall v \in \mathcal{V}$$

From the definition of weak convergence and using the characterization of $\mathcal{V}'$ (2.4), $\mathcal{A}u_n \rightharpoonup f$ is understood as

$$\left| \begin{array}{l} \displaystyle\int_0^T \int_\Omega \begin{bmatrix} k(u_n, \mathbf{x}, \beta)\nabla u_n \cdot \nabla v \\ + \,\omega(u_n, \mathbf{x}, \beta) c_{blood} u_n \; v \end{bmatrix} dxdt \\ \displaystyle + \int_0^T \int_{\partial\Omega_C} h u_n \; v \; dAdt - \int_0^T \int_\Omega (f \; v \; + \nabla f \cdot \nabla v)\, dxdt \end{array} \right| \to 0 \qquad \forall v \tag{2.9}$$

An element of the weakly converging sequence, u_n, may be chosen such that $\mathcal{A}u - f$ is as small as desired.

$$\begin{aligned} &\left| \begin{array}{c} \displaystyle\int_0^T \int_\Omega \begin{bmatrix} k(u, \mathbf{x}, \beta)\nabla u \cdot \nabla v \\ + \,\omega(u, \mathbf{x}, \beta) c_{blood} u \; v \end{bmatrix} dxdt \\ \displaystyle + \int_0^T \int_{\partial\Omega_C} h u \; v \; dAdt \end{array} - \int_0^T \int_\Omega (f \; v \; + \nabla f \cdot \nabla v)\, dxdt \right| \\ &= \left| \begin{array}{c} \displaystyle\int_0^T \int_\Omega \begin{bmatrix} (k(u, \mathbf{x}, \beta)\nabla u \pm k(u_n, \mathbf{x}, \beta)\nabla u_n) \cdot \nabla v \\ + \, c_{blood}(\omega(u, \mathbf{x}, \beta) u \pm \omega(u_n, \mathbf{x}, \beta) u_n) \; v \end{bmatrix} dxdt \\ \displaystyle + \int_0^T \int_{\partial\Omega_C} h(u \pm u_n) \; v \; dAdt \\ \displaystyle - \int_0^T \int_\Omega (f \; v \; + \nabla f \cdot \nabla v)\, dxdt \end{array} \right| \end{aligned} \tag{2.10}$$

Using the definition of the weak convergence of the operator (2.9) and a trace theorem and Rellich-Kondrachov (2.8) for the boundary term, (2.10) reduces to

$$\leq \epsilon + \left| \int_0^T \int_\Omega \begin{bmatrix} (k(u, \mathbf{x}, \beta)\nabla u - k(u, \mathbf{x}, \beta)\nabla u_n) \cdot \nabla v \\ + \, (k(u, \mathbf{x}, \beta)\nabla u_n - k(u_n, \mathbf{x}, \beta)\nabla u_n) \cdot \nabla v \\ + \, c_{blood}(\omega(u, \mathbf{x}, \beta) u - \omega(u, \mathbf{x}, \beta) u_n) \; v \\ + \, c_{blood}(\omega(u, \mathbf{x}, \beta) u_n - \omega(u_n, \mathbf{x}, \beta) u_n) \; v \end{bmatrix} dxdt \right|$$

and finally using that the constitutive equations are Lipschitz and that a weakly convergent sequence is bounded

$$
\begin{aligned}
&\leq \tilde{\epsilon} + \left| \int_0^T \int_\Omega \begin{bmatrix} (k(u,\mathbf{x},\beta) - k(u_n,\mathbf{x},\beta))\nabla u_n \cdot \nabla v \\ + c_{blood}(\omega(u,\mathbf{x},\beta) - \omega(u_n,\mathbf{x},\beta))u_n \; v \end{bmatrix} dxdt \right| \\
&\leq \tilde{\epsilon} + C \begin{pmatrix} \|k(u,\mathbf{x},\beta) - k(u_n,\mathbf{x},\beta)\|_{L_2(0,T;L_2(\Omega))} \\ + \|\omega(u,\mathbf{x},\beta) - \omega(u_n,\mathbf{x},\beta)\|_{L_2(0,T;L_2(\Omega))} \end{pmatrix} \\
&\leq \tilde{\epsilon} + \tilde{C}\|u - u_n\|_{L_2(0,T;L_2(\Omega))}
\end{aligned}
$$

the strong convergence in $L_2\left(0,T;L_2(\Omega)\right)$ implies the result. Additional assumptions on the constitutive equations may be required to prove monotinicity of the operator $\mathcal{A} : \mathcal{V} \rightarrow \mathcal{V}'$ and hence uniqueness.

From the above conditions, we may begin to identify a well-defined parameter space over which a solution is expected to exist. The parameter space used in the remainder of this dissertation is defined below.

$$
\mathbb{P} = \left\{ \begin{array}{c} \beta \in L_\infty(\Omega) \times \mathbb{R}^3 \times L_\infty(\Omega) \times \mathbb{R}^3 \times L_\infty([0,T]) \times \mathbb{R}^5 : \\ 0 < k_* < k_0(\mathbf{x}) + k_1 \text{atan}(k_2(u - k_3)) < k^* < \infty \\ 0 < \omega_* < \omega_0(\mathbf{x}) + \omega_1 \text{atan}(\omega_2(u - \omega_3)) < \omega^* < \infty \end{array} \right\} \qquad (2.11)
$$

The sense in which a solution satisfies (2.5) is not strictly equivalent to the solution of the original PDE (2.2). For a solution to the variational problem (2.5), classical arguments using the Lebesgue or Fourier Lemma may be used to recover the PDE in the sense of distributions, i.e.

$$
\langle \text{ Pennes PDE }, v \rangle_{\mathcal{D}' \times \mathcal{D}} = 0 \qquad \forall v \in \mathcal{D}
$$

however the remaining boundary terms

$$
\int_0^T \int_{\partial\Omega} k(u,\mathbf{x},\beta)\nabla u \cdot \mathbf{n} \; v \; dAdt = \int_0^T \int_{\partial\Omega_N} \mathcal{G} \; v \; dAdt + \int_0^T \int_{\partial\Omega_C} h(u - u_\infty) \; v \; dxdt
$$

may not be used to recover the original boundary conditions of the PDE because the trace of the normal derivative of an $H^1(\Omega)$ function may not be well-defined. Additional regularity on the solution is required to recover the boundary conditions of the PDE (2.2).

Chapter 3

The Control System

A new paradigm in computational modeling has emerged in recent years where the fidelity and predictability of computer models can be, in principle, greatly enhanced by developing feedback control systems which interface the computational model with real-time field measurements. Such systems are referred to generally as Dynamic Data Driven Application Systems [14]. In this research, a new and challenging DDDAS framework is developed to facilitate accurate real-time simulations of laser treatment of prostate cancer with the Pennes model developed in the previous chapters providing the core simulations tool and with the experimental real-time data provided by MRTI imaging of the actual therapy at a remote site - the imaging laboratory at M.D. Anderson Cancer Center in Houston, Texas. The goal is to develop an optimal control system that operates on a computational grid that connects the computational modeling arena in Austin, Texas (within TACC) with the MRTI-Laser therapy arena in Houston (M.D.A.C.C.). With accurate computer prediction, the location and power of the laser can be modulated to maximize damage to cancerous cells while minimizing damage to healthy tissue. This provides a canonical example of DDDAS and the use of so-called cyber-infrastructure. It also represents a significant extension of modern simulation methods as a means for real-time calibration and validation of models are made possible in this system.

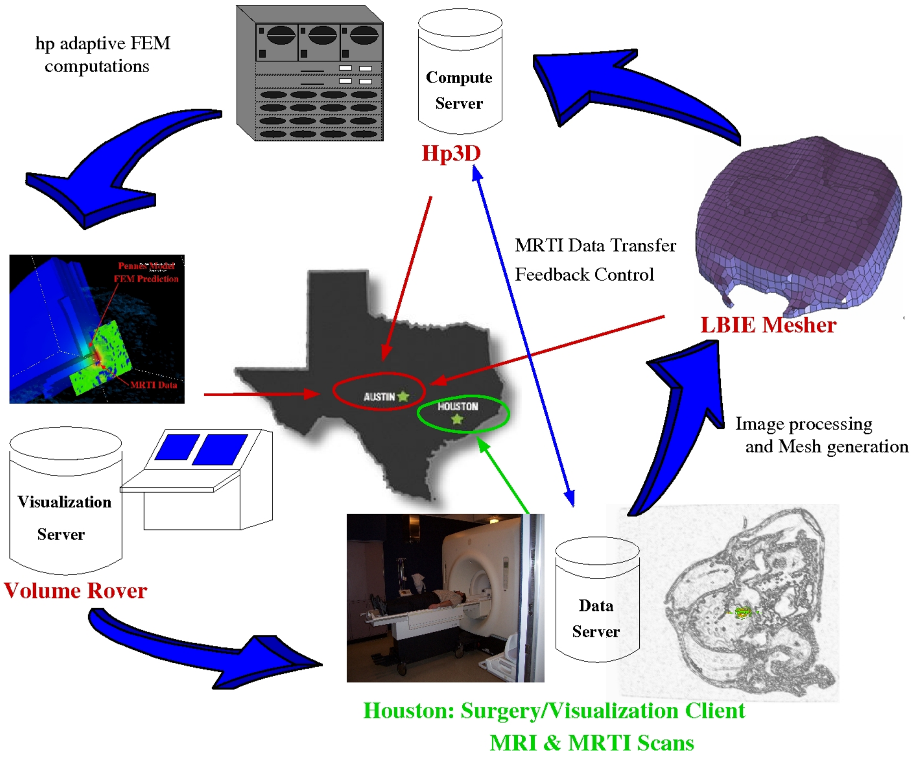

Figure 3.1: Schematic of the peer to peer communication architecture used to control the laser treatment process. Feedback control is achieved through the continual interaction of the data, compute, and visualization modules.

Figures 3.1 and 3.3 provide an outline of the computational grid and the data flow between the major software modules of the control system. The developmental stages uses canines as the host of prostate tumors as well as *ex vivo* canine prostate embedded within a 1% agar material, Figure 3.2. Communication connecting the software modules at the actual laboratory at M.D. Anderson Cancer Center in Houston, TX to the computing and visualization center in Austin, TX is handled via batch sftp over a commercial GigE Internet connection. Prior to treatment, the LBIE Mesher[1] generates a patient-specific

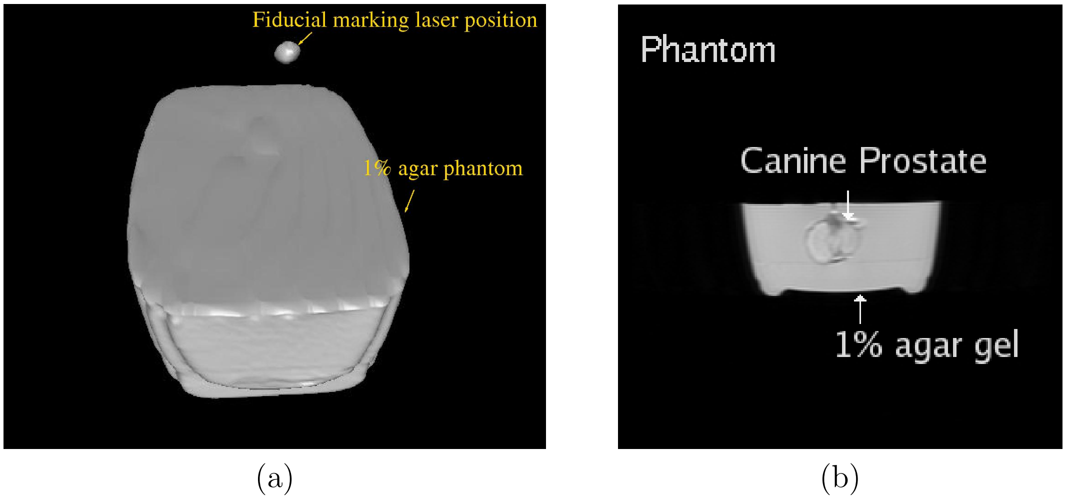

(a) (b)

Figure 3.2: The phantom geometry used in the development of the control system is shown. The phantom consists of a canine prostate embedded within a 1% agar gel.

finite element mesh of the biological domain using pre-operative MRI data. Optimal laser parameters (location of optical fiber, laser power, etc.) are then computed to eliminate/sensitize cancer cells, minimize damage to healthy cells, and control Heat Shock Protein (HSP) expression. Upon initiation of the treatment process, the software employs intra-operative MRI data to register the computational domain and real-time thermal imaging MRTI data drives the calibrations aligning the parameters of the Pennes bioheat transfer model to the patient's biological tissue values. As new thermal imaging data is acquired intermittently, the computational prediction is compared to the measurements of the real-time thermal images and the differences seen are used to update the computations of the optimal laser parameters. For example, if the model was incorrectly calibrated an the thermal images begin to detect unexpected high

---

[1] Software available at: http://cvcweb.ices.utexas.edu/cvc

temperatures the laser power is turned off. The model must be recalibrated before proceeding. The system is built around five main computing modules, as indicated in Figure 3.3.

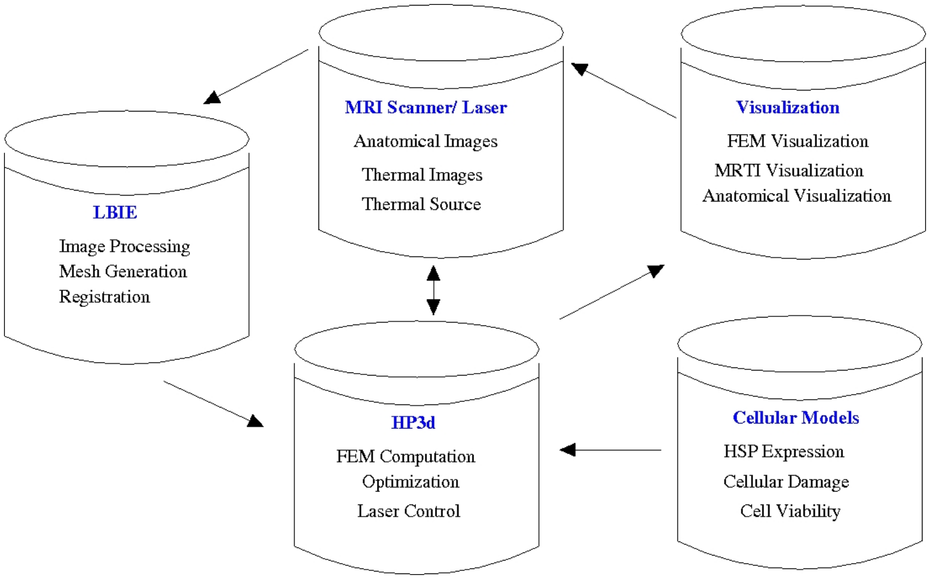

Figure 3.3: The computational infrastructure has five main modules: heating/imaging, finite element mesh generation, finite element computation, cellular damage models, and visualization. The data flow between the control system modules is illustrated.

The four stages of the treatment are illustrated in Figure 3.4. During the first stage, the biological domain is pulse heated and MRTI thermal image data is acquired for the heating as well as the cooling. The second stage of the treatment accounts for the time span of the calculations that use the imaging data for model calibration. The third stage accounts for the time delay to compute the optimal temperature/ damage/ HSP heating protocol. In the fourth and final stage, the optimal laser control parameters are applied to the biological domain. In the event of the detection of an unexpectedly high temperature within the biological domain, a fail-safe shutoffs the laser power.

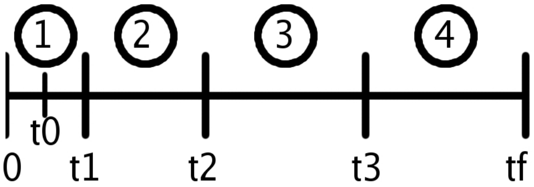

Figure 3.4: The treatment process is divided into four stages. 1. MRTI thermal image data is acquired and used for model calibration; 2. the time span of actual calibration computations; 3. the time span for optimal temperature/ damage/ HSP computations; and 4. the optimal laser control parameters are applied to the biological domain. In the event of the detection of an unexpectedly high temperature within the biological domain, a fail-safe shuts off the laser power.

A high-level abstraction of the HP3d[2] hp-adaptive finite element solver is shown in Figure 3.5. The models are implemented efficiently in parallel to meet the demands of rapid calibration and rapid optimal control calculations. The finite element solver is run at Texas Advanced Computing Center (TACC) located in Austin. The real-time laser treatment consists of four stages. During each stage, the problems of real-time calibration, optimal control, and goal-oriented error estimation are solved in parallel by separate groups of processors working together Figure 3.5.

---

[2] Software available at: http://dddas.ices.utexas.edu

Denoting group 0 as the computational group in charge of temperature/ damage/ HSP optimization and group 1 as the group of processors in charge of calibration, the logic of the computations is given in chronological order as follows:

- Before any thermal image transfer occurs, group 0 makes an initial prediction of the entire time history of temperature/damage/HSP from textbook or pre-calibrated material properties. The time window of the prediction is the entire length of the treatment $[0, t_f]$
- The domain is heated with a pulse during time $[0, t_0]$ and thermal images are generated from time $[0, t_1 > t_0]$ and group 1 will use the images from $[0, t_1]$ to calibrate the model. The image time is greater than the heating time, so that the the images record heating and cooling. Group 1 has the time window $[t_1, t_2]$ to finish the calibration computation; group 1 checkpoints its progress along the way and group 1 finishes by making a prediction over the time window $[0, t_f]$
- At time t_2, group 0 takes the latest parameter update from group 1 and proceeds to optimize the power from $[t_3, t_f](t_3 > t_2)$; group 0 has the time window $[t_2, t_3]$ to finish the optimal control computations. At time t_3, the optimizer is stopped and the final prediction is made over the time window $[t_3, t_f]$.

Periodically during treatment, the group-wise optimization solutions and error estimates are collected on the Control Task. A skeleton of the entire FEM mesh of the biological domain is stored on the Control Task. Using the collective error estimates, a mesh refinement strategy is computed on the

Control Task and both the collective optimization solutions and refinement strategy are broadcast to the individual Computational Groups. The Data Server shown in Figure 3.5 reads in the thermal images from disk, filters the thermal images to remove noise, broadcasts the thermal images to each computational group as needed, and transmits the laser power to Houston. The

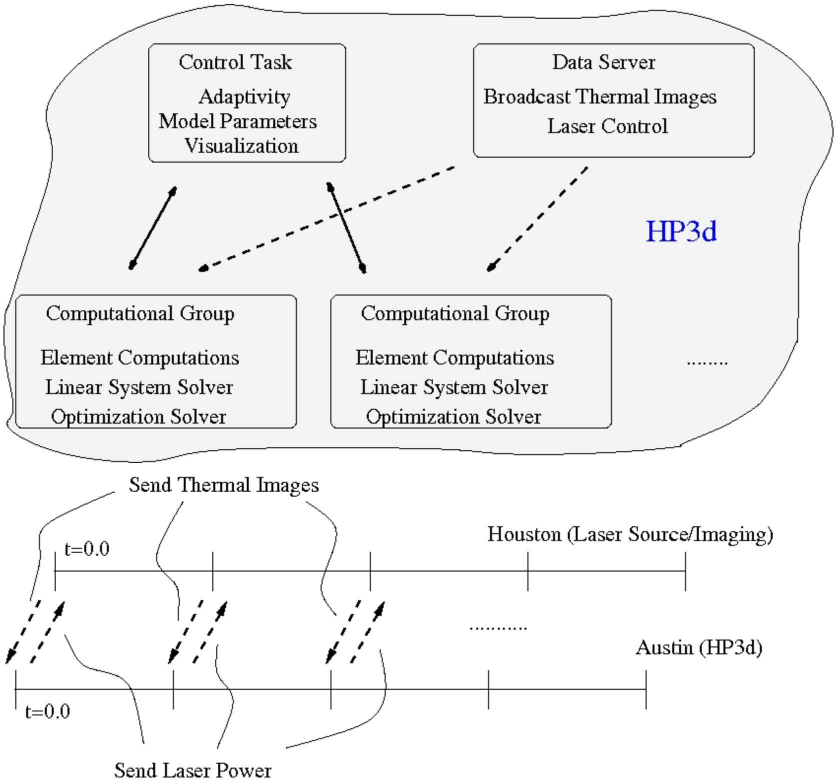

Figure 3.5: The finite element computations are performed on a parallel computing architecture using multiple groups of compute tasks to simultaneously solve disjoint numerical problems of the control system. A control task in used to gather and broadcast the individual solutions of the computational groups. A data server broadcasts filtered thermal images to individual computational groups as requested. The imaging implicitly controls the laser power output. As a new thermal image is acquired by HP3d in Austin, the power wattage for the next time interval is transmitted to the laser.

timing of the laser power control is implicit through the image acquisition by the HP3d Data Server in Austin. As new thermal images are written to disk physically in Houston, they are transferred to disk at TACC. When the Data Server detects that the full set of thermal images for a time instance is available, the power to be used for the next time interval is sent to Houston.

The software infrastructure is built from the Petsc [3] parallel computing paradigm and the TAO [6] parallel optimization library. AVS [21] is used in conjunction with a VNC server for remote visualization. AVS coroutines are used to manage and coordinate the simultaneous visualization of the MRI anatomical image, MRTI thermal image, and finite element data sets. From a computational point of view, the orchestration of a successful laser treatment is to solve the problems of registration, calibration, and optimal control invisibly to the surgeon, and provide the surgeon with an a priori visualization of the outcome of the treatment for use as guidance for the actual treatment.

3.1 Model Optimization

There are three fundamental problems of the control system: calibration, optimal control, and mesh refinement. These problems will now be formally defined. Consider the biological domain Ω shown in Figure 3.6. The biological domain Ω is composed of a of region of healthy tissue Ω_H and a region of cancerous tissue Ω_C. $\Omega = \Omega_H \cup \Omega_C$. The domain, Ω, is heated by a laser heat source within the time in-

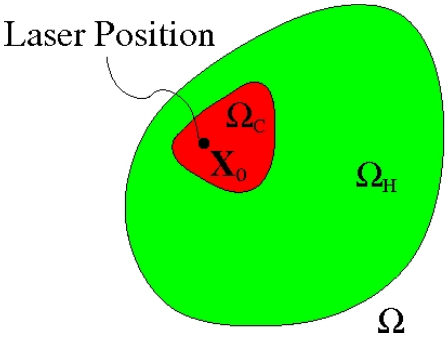

Figure 3.6: A biological domain composed of a cancerous region (red) and a region of healthy tissue.

terval $[0, \tau]$. The model parameters available for control of the laser heat source are the position of the laser tip, $\mathbf{x}_0 = (x_0, y_0, z_0)$, the power as a piecewise constant function of time, $P(t)$. The material properties available for model calibration are the thermal conductivity $k_0(\mathbf{x}), k_1, \tilde{k}_3, \hat{k}_3$ the perfusion $\omega_0(\mathbf{x}), \omega_1, \tilde{\omega}_3, \hat{\omega}_3$ and the coefficients of scattering and absorption, μ_s and μ_a. The entire time span of the laser treatment occurs within the interval $[0, T]$, $[0, \tau] \subset [0, T]$. As before, β will denote all model parameters.

$$\boxed{\beta \equiv (k_0(\mathbf{x}), k_1, \tilde{k}_3, \hat{k}_3, \omega_0(\mathbf{x}), \omega_1, \tilde{\omega}_3, \hat{\omega}_3, P(t), \mu_a, \mu_s, \mathbf{x}_0)}$$

The temperature field resulting from the application of the heat source is an implicit function of the model parameters.

$$u(\beta, \mathbf{x}, t) \qquad t \in [0, T] \qquad \mathbf{x} \in \Omega \qquad \beta \in \mathbb{P}$$

where $\mathbb{P}$ is defined in (2.11). For the remainder of this chapter, it is assumed that the appropriate initial conditions and boundary conditions are given and that the temperature field, $u(\beta, \mathbf{x}, t)$, is computed from Pennes model and is known.

3.1.1 Calibration of Pennes Model

The problem of model calibration is to find the set thermal conductivity parameters $k_0(\mathbf{x}), k_1, \tilde{k}_3, \hat{k}_3$, and blood perfusion parameters $\omega_0(\mathbf{x}), \omega_1, \tilde{\omega}_3, \hat{\omega}_3$ that minimize the $L_2(0, T; L_2(\Omega))$ norm of the difference between the predicted temperature field and an ideal field, $u^{ideal}(\mathbf{x}, t) \quad \mathbf{x} \subset \Omega \quad t \subset [0, T]$.

$$Q(u(\beta, \mathbf{x}, t)) = \frac{1}{2} \|\chi(\mathbf{x})(u(\beta, \mathbf{x}, t) - u_{ideal}(\mathbf{x}, t))\|^2_{L_2(0,T;L_2(\Omega))} \tag{3.1}$$

The ideal field for the calibration problem is the experimentally determined temperature field $u^{exp}(\mathbf{x}, t) \quad \mathbf{x} \subset \Omega \quad t \subset [0, T]$ in this case, those values obtained from MRTI data. The set of laser parameters, $P(t), \mu_a, \mu_s, \mathbf{x}$, are fixed.

3.1.2 Temperature Based Control

The optimal treatment of a cancer-infected tissue is defined by the following criteria:

- Maintain the functionality of the healthy region of the tissue.
- Maximize damage to the cancerous region.

Various metrics based on temperature, damage, or HSP expression are used to evaluate the degree to which the criteria is satisfied. The discussion of the temperature based metric is followed by the damage and HSP metric.

Similar to the calibration problem, the goal of the temperature-based optimal control is to find the set of model parameters that minimize the space-time norm of the difference between the computed temperature field $u(\beta, \mathbf{x}, t)$ and an ideal field $u^{ideal}(\mathbf{x}, t)$. The mathematical structure is the same as in (3.1). However, the ideal field for temperature-based optimal control maximizes damage to cancerous tissue while minimizing damage to healthy tissue,

$$u^{ideal} = \begin{cases} 37.0^o C & \mathbf{x} \in \Omega_H \\ 50.0^o C & \mathbf{x} \in \Omega_C \end{cases}$$

The domains of the healthy and cancerous tissue are denoted Ω_H and Ω_C, respectively. Moreover, for temperature based optimal control, the laser control parameters, $\mathbf{x}_0$ and $P(t)$ are varied to minimize (3.1) and the material parameters, $k(u, \mathbf{x}, \beta)$, $\omega(u, \mathbf{x}, \beta)$, μ_s, and μ_a are fixed.

3.1.3 Damage Based Control

The thermal injury resulting from the application of the heat source is reflected in the damage field, $D(\mathbf{x})$. Let φ denote the functional that acts on the temperature field and returns the corresponding damage field.

$$\varphi : L_2(0, T, H^1(\Omega)) \rightarrow L_2(\Omega)$$

$$\varphi(u(\beta, \mathbf{x}, t)) = D(\mathbf{x}) \qquad \forall \mathbf{x} \in \Omega$$

Assume there exists an ideal damage field, $D^{ideal}(\mathbf{x})$, that maximizes damage to the cancerous region while maintaining functionality of the healthy region. As a concrete example, consider the ideal damage field to be a *discontinuous* function of $\mathbf{x} \in \Omega$. Within the cancerous region there is a threshold damage value, denoted D_C^{ideal}, *above* which all cancerous cells will die. Similarly, within the healthy region there is a threshold damage value, denoted D_H^{ideal}, *below* which the functionality is maintained for all healthy cells.

$$D^{ideal}(\mathbf{x}) \equiv \begin{cases} D_C^{ideal} & \mathbf{x} \in \Omega_C \\ D_H^{ideal} & \mathbf{x} \in \Omega_H \end{cases}$$

The measure of success of the cancer treatment process is determined by the degree that the damage field resulting from the application of a laser heat source $\varphi(u(\beta, \mathbf{x}, t)) = D(\mathbf{x})$ satisfies the ideal conditions:

$$Y_C \equiv \left\{ \mathbf{x} \in \Omega_C : D(\mathbf{x}) \geq D_C^{ideal} \right\}$$

$$Y_H \equiv \left\{ \mathbf{x} \in \Omega_H : D(\mathbf{x}) \leq D_H^{ideal} \right\}$$

The goal of the treatment is to maximize the volume of cancerous cells that have reached a damage threshold to eradicate the cells and minimize the volume of healthy cells that reach a threshold beyond which the healthy tissue begins to lose functionality, ie.

$$|Y_C| = |\Omega_C| \qquad \text{and} \qquad |Y_H| = |\Omega_H| \tag{3.2}$$

Here $|\cdot|$ denotes the Lebesgue measure of the set. Since the temperature field is a continuous function, the resulting damage field is expected to be a continuous function. Therefore, (3.2) is *unattainable*. There will always exist a region where the damage field does not satisfy the ideal criteria. In this region, healthy cells will lose functionality and/or cancerous cells will not be destroyed. A one dimensional illustration is shown in Figure 3.7. With this in mind, the best that can be achieved is to minimize the region in which the ideal criteria is not achieved. A mathematical formulation with this problem in mind is to minimize the L_2-norm of the difference between the ideal damage field and the computed damage field,

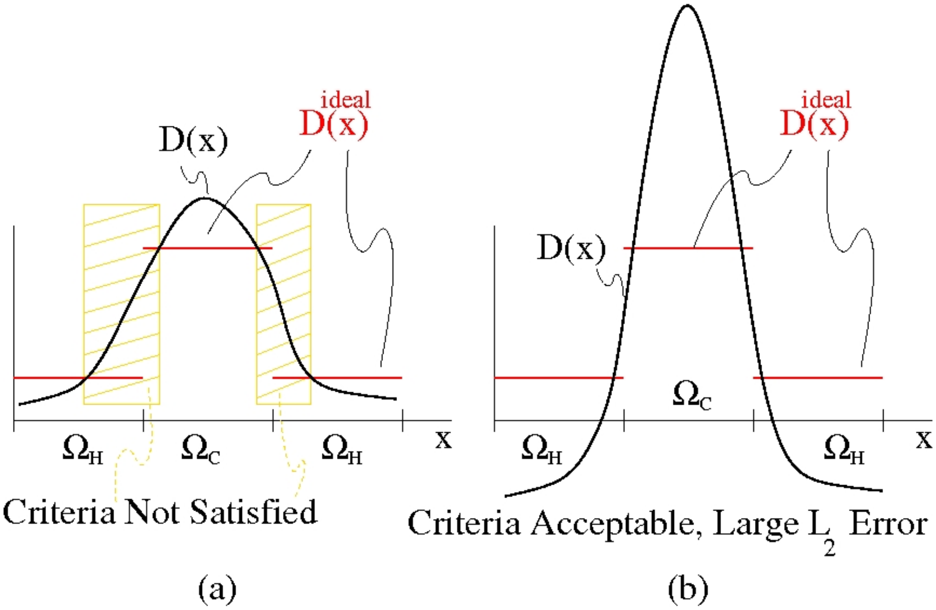

Figure 3.7: (a) The damage field will never satisfy the ideal criteria. There will always be a region where healthy cells will lose functionality and/or cancerous cells will not be destroyed. (b) a solution that is acceptable to the damage criteria may have a large L_2 error.

$$Q(u(\beta,\mathbf{x},t)) = \frac{1}{2}\|\varphi(u(\beta,\mathbf{x},t)) - D^{ideal}(\mathbf{x})\|^2_{L_2(\Omega)} = \frac{1}{2}\|D(\mathbf{x}) - D^{ideal}(\mathbf{x})\|^2_{L_2(\Omega)}$$

The optimization problem minimizes the cost function over the parameter space $\mathbb{P}$.

$$\min_{\beta\in\mathbb{P}} Q(u(\beta,\mathbf{x},t)) \tag{3.3}$$

However, notice the possibility that a completely acceptable solution to (3.2) may have a large L_2 error see Figure 3.7. Therefore, during the solution process of (3.3), the ratio of the volume of the domain that satisfies the ideal criteria to the total volume of the domain should be used as a measure of the degree to which (3.3) satisfies (3.2),

$$\frac{|Y_C|}{|\Omega_C|} \qquad \text{and} \qquad \frac{|Y_H|}{|\Omega_H|} \tag{3.4}$$

In the event that the ratios (3.4) resulting from the solution to (3.3) are unsatisfactory, the criteria may be weakened by allowing a percentage of the healthy cells to be destroyed along with the cancerous cells. i.e.

$$D^{ideal}(\mathbf{x}) \equiv \begin{cases} D_C^{ideal} & \mathbf{x}\in\Omega_C+\epsilon \\ D_H^{ideal} & \mathbf{x}\in\Omega_H-\epsilon \end{cases}$$

where ϵ is a small region of around the boundary of Ω_C and $\epsilon\subset\Omega_H$.

3.1.3.1 Damage Models

An Arrhenius model and a the Two-State model are used to quantify the damage from the thermal assault on the biological domain, Ω. The Arrhenius model is a classical empirical law used in early models of thermal effects and properties of molecular averages. For the Arrhenius model, φ represents the *damage index*, and for the Two-State model, φ represents the *cell viability.*

$$\varphi(u(\beta,\mathbf{x},t)) = D(\mathbf{x}) = \begin{cases} \displaystyle\int_0^T A\, e^{\frac{-E_a}{R\,u}}\, dt & \text{Arrhenius} \\ \displaystyle\int_0^T \frac{e^{-\left(\frac{h}{u}+\alpha\, t+\beta\right)}}{1+e^{-\left(\frac{h}{u}+\alpha\, t+\beta\right)}}\, dt & \text{Two-State} \end{cases}$$

The constants E_a, A, and R are *known* constants of the Arrhenius model and h, α, and β are *known* constants of the Two-State model determined from *in-vitro* experiments on cell samples [20]. Note that the numerical values of D_C^{ideal} and D_H^{ideal} for the Arrhenius model will be different from D_C^{ideal} and D_H^{ideal} for the Two-State model.

3.1.4 HSP Based Control

Heat Shock Protein (HSP) expression based control is similar to damage control. It is assumed that the function mapping the temperature field to the corresponding HSP expression field is known.

$$H : L_2(0, T, H^1(\Omega)) \to L_2(\Omega) \qquad H(u(\beta, \mathbf{x}, t))(\mathbf{x}) \in L_2(\Omega)$$

The constitutive data mapping the temperature field to the HSP expression field is obtained from *in vitro* cellular data [36].

3.1.5 Summary of Optimization Problems

A summary of the objective functions is provided below.

$$Q(u(\beta, \mathbf{x}, t)) = \begin{cases} \frac{1}{2}\int_\Omega \int_0^T \left(u(\mathbf{x}, t) - u^{ideal}(\mathbf{x})\right)^2 \, dtdx & \text{calibration/temp. based} \\ \frac{1}{2}\int_\Omega \left(\int_0^\tau A\, e^{\frac{-E_a}{R\, u}} \, dt - D^{ideal}(\mathbf{x})\right)^2 dx & \text{Arrhenius} \\ \frac{1}{2}\int_\Omega \left(\int_0^T \frac{e^{-\left(\frac{h}{u} + \alpha\, t + \beta\right)}}{1 + e^{-\left(\frac{h}{u} + \alpha\, t + \beta\right)}} \, dt - D^{ideal}(\mathbf{x})\right)^2 dx & \text{Two-State} \\ \frac{1}{2}\int_\Omega \left(H(\mathbf{x}) - H^{ideal}(\mathbf{x})\right)^2 dx & \text{HSP} \end{cases}$$

3.2 Mesh Refinement

Procedures for computing goal-oriented error estimates have been presented in Oden and Prudhomme [29, 28] and Becker and Rannacher [5] and used as a basis for adaptive meshing algorithms to produce near optimal meshes. These estimates and adaptive procedures focus on optimizing the accuracy in computed values of specified quantities of interest, such as average temperature over Ω_C. Goal oriented error estimates are calculated under the following framework:

- For a fixed set of model parameters β_0,

$$C(u, \beta_0; v) = B(u, \beta_0; v) - F(\beta_0; v)$$

- Let $\mathcal{V}^h$ and $\mathcal{V}^{hp}$ represent two finite dimensional spaces such that $\mathcal{V}^h \subset \mathcal{V}^{hp}$.
- Assume that $\|u^{hp} - u\|_{\mathcal{V}} \leq \|u^h - u\|_{\mathcal{V}}$ where u, u^h, u^{hp} satisfy the Pennes model constraints

$$\begin{aligned} C(u, \beta_0; v) &= 0 \qquad \forall v \in \mathcal{V} \\ C(u^{hp}, \beta_0; v^{hp}) &= 0 \qquad \forall v^{hp} \in \mathcal{V}^{hp} \\ C(u^h, \beta_0; v^h) &= 0 \qquad \forall v^h \in \mathcal{V}^h \end{aligned}$$

The solution $u^{hp} \in \mathcal{V}^{hp}$ of the discrete approximation of the Pennes model is assumed to be a more accurate representation of the exact solution $u \in \mathcal{V}$ than $u^h \in \mathcal{V}^h \subset \mathcal{V}^{hp}$. Further, we assume that an arbitrary quantity of interest, Q, approximated as $Q(u^{hp})$ is a more accurate representation of $Q(u)$ than the quantity of interest $Q(u^h)$.

The following Taylor series approximations is invoked

$$Q(u^{hp}) \approx Q(u^h) + \delta Q(u^h; u^{hp} - u^h)$$

$$C(u^{hp}, \beta_0; v^{hp}) \approx C(u^h, \beta_0; v^{hp}) + \delta C(u^h, \beta_0; u^{hp} - u^h, v^{hp})$$

with

$$\begin{aligned}\delta Q(u;\hat{u}) &\equiv \lim_{\theta\to 0}\frac{1}{\theta}\left[Q(u+\hat{u})-Q(u)\right]\\ \delta C(u,\beta_0;\hat{u},v) &\equiv \lim_{\theta\to 0}\left[C(u+\hat{u},\beta_0;v)-C(u,\beta_0;v)\right]\end{aligned}$$

The adjoint variable $p^{hp}\in\mathcal{V}^{hp}$ is defined as the solution of the linear problem, such that

$$\delta Q(u^h;\hat{u}) = \delta C(u^h,\beta_0;\hat{u},p^{hp}) \qquad \forall \hat{u}\in\mathcal{V}^{hp}$$

With this function in hand, we calculate the relative error in the quantity of interest:

$$\begin{aligned}Q(u^{hp})-Q(u^h) &= -\,C(u^h,\beta_0;p^{hp}) = F(\beta_0,p^{hp})-B(u^h,\beta_0;p^{hp})\\ &= -\int_0^T\int_\Omega\left[\begin{aligned}&\rho c_p\frac{\partial u^h}{\partial t}p^{hp}+k(u^h,\beta_0)\nabla u^h\cdot\nabla p^{hp}\\ &\qquad\qquad +\omega(u^h,\beta_0)c_{blood}(u^h-u_a)\,p^{hp}\end{aligned}\right]dxdt\\ &\quad -\int_0^T\int_{\partial\Omega_C}h(u^h-u_\infty)\,p^{hp}\,dAdt-\int_0^T\int_{\partial\Omega_N}\mathcal{G}\,p^{hp}\,dAdt\\ &\quad +\int_0^T\int_\Omega Q_{laser}(\mathbf{x},\beta_0)p^{hp}\,dxdt\\ &=\int_0^T\mathcal{Z}(t)dt=\int_\Omega\mathcal{X}(\mathbf{x})\,dx+\int_{\partial\Omega_C}\mathcal{R}(\mathbf{x})\,dA+\int_{\partial\Omega_N}\mathcal{N}(\mathbf{x})\,dA\end{aligned} \tag{3.5}$$

The error estimate (3.5) is written as a function of time or space using $\mathcal{Z}(t)$ or $\mathcal{X}(\mathbf{x})$, $\mathcal{R}(\mathbf{x})$, and $\mathcal{N}(\mathbf{x})$; respectively. The temporal form is used to determine when greater time stepping accuracy is needed, likewise the spatial form is used to determine when spatial mesh refinement is needed. $\mathcal{Z}(t)$, $\mathcal{X}(\mathbf{x})$, $\mathcal{R}(\mathbf{x})$, and $\mathcal{N}(\mathbf{x})$ are defined as

$$\begin{aligned}\mathcal{Z}(t) = &-\int_\Omega\left[\rho c_p\frac{\partial u^h}{\partial t}p^{hp}+k(u^h,\beta_0)\nabla u^h\cdot\nabla p^{hp}+\omega(u^h,\beta_0)c_{blood}(u^h-u_a)p^{hp}\right]dx\\ &-\int_{\partial\Omega_C}h(u^h-u_\infty)\,p^{hp}\,dA-\int_{\partial\Omega_N}\mathcal{G}\,p^{hp}\,dA+\int_\Omega Q_{laser}(\mathbf{x},\beta_0)p^{hp}\,dx\end{aligned}$$

$$
\begin{aligned}
\mathcal{X}(\mathbf{x}) = & \int_0^T Q_{laser}(\mathbf{x},\beta_0) p^{hp} - \rho c_p \frac{\partial u^h}{\partial t} p^{hp} \\
& - \int_0^T k(u^h,\beta_0) \nabla u^h \cdot \nabla p^{hp} - \omega(u^h,\beta_0) c_{blood} (u^h - u_a)\, p^{hp}\, dt \\
& \mathcal{R}(\mathbf{x}) = - \int_0^T h(u^h - u_\infty)\, p^{hp}\, dt \qquad \qquad \mathcal{N}(\mathbf{x}) = - \int_0^T \mathcal{G}\, p^{hp}\, dt
\end{aligned}
$$

3.3 Computing Requirements

A rough estimate of the computational requirements are given in this section to demonstrate the feasibility of the real-time computations. Each problem of optimal control, error estimation, and calibration of a bioheat transfer model involves the solution of a time dependent nonlinear parabolic PDE and a corresponding linear adjoint problem stepping backwards in time. Using a Newton method to solve the nonlinear forward problem with roughly 3 Newton iterations per time step, there are four total linear system solves per time step, including the adjoint solve. The optimization process requires approximately ten gradient computations, each requiring one forward stepping and one backward stepping. As a concrete example, consider a 30 second simulation with a time step of one second. The total number of linear solves is thus

$$
\begin{aligned}
& \approx 10 \text{ gradient computations} \\
& \quad * \, 4 \text{ linear system solves per gradient } * \, 30 \text{ time steps} \\
& \approx 1200 \text{ linear system solves}
\end{aligned}
$$

For illustration purposes, assume that a reasonable finite element mesh contains roughly 30000 degrees of freedom. The iterative solver requires roughly 30 sparse-matrix vector multiplies to converge. For linear elements, 27 is an upper bound on the number of matrix entries per row. Thus, the cost per linear system solve is $\approx 30 \cdot 27 \cdot N_{dof}$. As a rough approximation, assume that the cost of the assembly and building a preconditioner are both equal to the cost of the solve. Under these assumptions, the real time computation requires $\approx$ 90e+9 floating point operations. This computational requirement is attainable with 32 2.66Ghz Intel Xeon processors (10.6 GFLOPS peak) operating at a conservative 5% the theoretical maximum flop rate for 6 secs.

3.3.1 Communications

Communications requirements for the DDDAS system will consist of sending five DICOM image files from Houston to Austin as it is generated every five seconds. The size of the 256x256 pixel DICOM file is $\approx$ 140 kB. With a GigE Internet connection of approximately 300 kB/s and, assuming a reasonable latency, the files can be delivered from Houston to Austin in roughly two seconds. The data sent from Austin to Houston is negligible as current and projected control of the laser will consist of sending an small array of time and laser power data for each laser. Post-processing data of comparable size to the DICOM file will be sent to Houston. Thus the GigE connection used to send data from Houston to Austin will suffice to also send data from Austin to Houston.

3.3.2 Memory

Inherent to the forward and backward time stepping of the optimization problems is a significant amount of re-computation. Extensive use of every bit of RAM available will significantly increase performance of the parallel code; i.e. instead of recomputing, save the data. The entire time history of the temperature field is stored in memory so that no re-computation is required on the adjoint solve.

3.3.3 I/O and Disk Storage

A single 10 min treatment requires 84.0 MB (700 * 120) of storage space for the raw DICOM DATA. The initial mesh file generated from the data is around 3.0 MB in size for a 30000 dof mesh. Each time step for the optimal control and calibration will write out a visualization file to disk again a size 3.0 MB. Thus, for a single run the data output to make movies is $\approx$(2 problems) *(10*60 time steps) * 3.0MB which is roughly 3.6 GB per treatment. Current I/O systems capable of sustaining bandwidths of about 100 MB/s. can write out a visualization file for a single time step in under 0.3 seconds.

Chapter 4

Optimization Framework

An adjoint method solution of the optimization problems of the control loop is studied from several layers of abstraction within this section. A high level abstraction of the solution to the optimization problem is presented. The solution is presented under the framework of differential calculus in Banach spaces and clearly demonstrates how the use of an adjoint variable eliminates the need to solve for sensitivities of the solution. The strong form of the adjoint problem is provided along with an outline of the steps involved with the gradient computation. Finally, the PDE based optimization process is applied to the Pennes equation and the fully discretized equations are given.

The variational framework developed in Section 2.3.1 must be rewritten within a framework suitable for optimization. Using the notation of (2.6) and (2.7),

$$C(u,\beta;v) : \mathcal{V} \times \mathbb{P} \times \mathcal{V} \to \mathbb{R}$$

denotes the governing PDE and is nonlinear with respect to the first two arguments, u, β, but linear with respect to the test function, v.

$$\begin{aligned} \forall v \qquad C(u,\beta;v) &= 0 \\ &= \left\langle \rho c_p \frac{\partial u}{\partial t}(\mathbf{x},t) + \mathcal{A}(\beta)u(\mathbf{x},t) - \mathcal{F}(\beta), v \right\rangle_{\mathcal{V}'\times\mathcal{V}} \end{aligned}$$

$$
\begin{aligned}
= & \int_0^T \int_\Omega \rho c_p \frac{\partial u}{\partial t}\, v \; dxdt + \int_0^T \int_\Omega k(u, \mathbf{x}, \beta) \nabla u \cdot \nabla v \; dxdt \\
& + \int_0^T \int_\Omega \omega(u, \mathbf{x}, \beta) c_{blood} (u - u_a)\; v \; dxdt + \int_0^T \int_{\partial\Omega_N} \mathcal{G} \; v \; dAdt \\
& - \int_0^T \int_\Omega Q_{laser}(\beta, \mathbf{x}, t) v \; dxdt + \int_0^T \int_{\partial\Omega_C} h(u - u_\infty)\; v \; dxdt
\end{aligned}
\tag{4.1}
$$

where $u, v \in \mathcal{V} \equiv L_2\left([0,T], H^1(\Omega)\right)$ and the control variable, β, belongs to the relevant parameter space, $\beta \in \mathbb{P}$, see (2.11).

4.1 Mathematical Formulation of the Optimization Problem

The adjoint method considered is based on the chain rule in Banach spaces. The chain rule is known to hold for compositions of Fréchet-differentiable functions. All functions are assumed Fréchet-differentiable, defined below.

Definition 4.1.1. Let $f : U \to Y$ where $U \subset X$ is open and X, Y are normed linear spaces. For $x \in U$, f is Fréchet-differentiable if $\exists\; Df(x) \in B(X, Y)$ such that

$$
\frac{\|f(x+h) - f(x) - Df(x)h\|_Y}{\|h\|_X} \to 0 \qquad \text{as } \|h\|_X \to 0
$$

Here $B(X, Y)$ is the space of bounded linear operators from X into Y. For functions defined on the Cartesian products of spaces the notion of partial Fréchet differentiability is also of importance.

Definition 4.1.2. Let X denote the direct sum of the space of trial functions and parameter space, $X = \mathcal{V} \oplus \mathbb{P}$. For U open, $U \subset X$, and $F : U \to Y$

consider the point $x = (u, \beta) \in X$. Define

$$f_u(z) : \mathcal{V} \to \mathbb{R} \qquad f_u(z) = F(z, \beta)$$

$$f_\beta(s) : \mathbb{P} \to \mathbb{R} \qquad f_\beta(s) = F(u, s)$$

The Fréchet derivative of $f_u(z)$ at $z = u$ and $f_\beta(s)$ at $s = \beta$ are the partial derivatives F in the direction of u and β; respectively.

$$D_u F(x) : \mathcal{V} \to \mathbb{R} \qquad D_u F(x) = Df_u(u)$$

$$D_\beta F(x) : \mathbb{P} \to \mathbb{R} \qquad D_\beta F(x) = Df_\beta(\beta)$$

The Fréchet derivative of F at (u, β) is the sum of its partial derivatives [2].

The optimizations problems in the control loop is to minimize a given objective function, Q, over parameter space, $\mathbb{P}$.

$$\boxed{\begin{array}{l}\text{Find } \beta^* \in \mathbb{P} \text{ s.t.} \\ \qquad Q(u(\beta^*), \beta^*) = \inf_{\beta \in \mathbb{P}} Q(u(\beta), \beta)\end{array}}$$

where $u \in \mathcal{V}$ is the state variable determined by a variational PDE of the form

$$C(u, \beta; v) = 0 \qquad \forall v \in \mathcal{V}$$

The gradient of the objective function with respect to the control variables is the work horse of the optimization schemes in this dissertation. The objective function is guaranteed to decrease in the direction of the gradient and is also used to approximate the Hessian in a quasi-Newton scheme. A Newton scheme for optimization is not considered in this work. The real-time nature of the control system does not permit the computation of the Hessian of the objective function.

It is necessary to determine the gradient of the objective function with respect to the control variables. The Pennes model solution, u, is considered to be a function of the the control parameters, β, and the objective function, Q, is considered to be a function of the Pennes model solution, u, and the control parameters, β. Consequently, the composition of the objective function with the Pennes model solution, denoted as $Q \diamond u$, is considered as solely a mapping from parameters space to the real numbers.

$$\begin{aligned} &u(\beta) : \mathbb{P} \rightarrow \mathcal{V} \\ &Q(u, \beta) : \mathcal{V} \times \mathbb{P} \rightarrow \mathbb{R} \\ &Q \diamond u \equiv Q(u(\beta), \beta) : \mathbb{P} \rightarrow \mathbb{R} \end{aligned}$$

The derivative of the composition, $Q \diamond u$, is of interest and is computed under the following first order approximations of the solution and objective function.

$$\begin{aligned} u(\beta + \hat{\beta}) &= u(\beta) + u'(\beta)\hat{\beta} \\ Q(u + \hat{u}, \beta + \hat{\beta}) &= Q(u, \beta) + D_u Q(u, \beta)\hat{u} + D_\beta Q(u, \beta)\hat{\beta} \end{aligned}$$

Here $u' : \mathbb{P} \rightarrow \mathcal{V}$ denotes the Fréchet derivative of the solution with respect to the control variables, $D_u Q : \mathcal{V} \rightarrow \mathbb{R}$ is the partial Fréchet derivative with respect to the solution, and $D_\beta Q : \mathbb{P} \rightarrow \mathbb{R}$ is the partial Fréchet derivative with respect to the control variables. Using the chain rule,

$$D(Q \diamond u) : \mathbb{P} \rightarrow \mathbb{R} \qquad D(Q \diamond u) = D_u Q(u, \beta)u'(\beta) + D_\beta Q(u, \beta) \tag{4.2}$$

Notice that to compute the gradient of the objective function, Q, the sensitivities, u', must be computed. The variation of the PDE constraints with respect to the model parameters may be used to compute the sensitivities. Only model parameters for which a solution to the governing PDE exists are of interest, i.e. $\beta : C(u(\beta), \beta; v) = 0 \ \forall v$, within this hyper-space the variation is identically zero.

$$\boxed{(D_u C u' + D_\beta C) : \mathbb{P} \rightarrow \mathbb{R} \qquad D_u C(u, \beta; v)u'(\beta) + D_\beta C(u, \beta; v) = 0 \ \ \forall v \in \mathcal{V}} \tag{4.3}$$

where $D_uC : \mathcal{V} \to \mathbb{R}$ is the partial Fréchet derivative of the PDE with respect to the solution and $D_\beta C : \mathbb{P} \to \mathbb{R}$ is the partial Fréchet derivative of the PDE with respect to the model parameters. The adjoint method of computing the gradient of the objective function may now be formulated.

Theorem. Given $\beta \in \mathbb{P}$, the derivative of the objective function is

$$\boxed{D(Q \diamond u) = D_\beta Q(u(\beta), \beta) - D_\beta C(u(\beta), \beta; p)} \tag{4.4}$$

where $u \in \mathcal{V}$ is the solution of the Pennes model and $p \in \mathcal{V}$ is the solution to the adjoint problem.

$$\boxed{\begin{array}{l} \text{Find } p \in \mathcal{V} : \\ \qquad \langle D_uC(u(\beta), \beta; p), \hat{u} \rangle_{\mathcal{V}' \times \mathcal{V}} = \langle D_uQ(u(\beta), \beta), \hat{u} \rangle_{\mathcal{V}' \times \mathcal{V}} \qquad \forall \hat{u} \in \mathcal{V} \end{array}}$$

Proof. For a fixed β, the solution to the adjoint problem, p, implies that

$$\langle D_uC(u(\beta), \beta; p), u' \rangle_{\mathcal{V}' \times \mathcal{V}} = \langle D_uQ(u(\beta), \beta), u' \rangle_{\mathcal{V}' \times \mathcal{V}}$$

From the first variation of the PDE constraints (4.3), we have that

$$D_uC(u(\beta), \beta; p) u'(\beta) = -D_\beta C(u(\beta), \beta; p)$$

The gradient follows from a direct substitution in (4.2) to eliminate the sensitivities

$$\begin{aligned} D(Q \diamond u) &= D_uQ(u, \beta) u'(\beta) + D_\beta Q(u, \beta) \\ &= D_\beta Q(u, \beta) - D_\beta C(u(\beta), \beta; p) \end{aligned}$$

□

Recall that $D(Q \diamond u)$ is an operator on the parameter space, $\mathbb{P}$, and the desired solution, β, is such that

$$D(Q \diamond u)(\beta) = 0 \iff \left\langle D(Q \diamond u)(\beta), \hat{\beta} \right\rangle = 0 \qquad \forall \hat{\beta} \in \mathbb{P}$$

4.1.1 The Continuous Adjoint Problem

As a concrete example, the strong form of the adjoint problem is derived from the Fréchet derivatives used to develop (4.4). The following Taylor series expansion will be used in computing the Gateaux derivatives of the variational form of Pennes model.

$$k(u+\hat{u},\beta+\hat{\beta}) = k(u,\beta) + \hat{u}\frac{\partial k}{\partial u} + \hat{k_0}\frac{\partial k}{\partial k_0} + \hat{k_1}\frac{\partial k}{\partial k_1} + \hat{k_2}\frac{\partial k}{\partial k_2} + \hat{k_3}\frac{\partial k}{\partial k_3} + \text{h.o.t.}$$

$$\omega(u+\hat{u},\beta+\hat{\beta}) = \omega(u,\beta) + \hat{u}\frac{\partial \omega}{\partial u} + \hat{\omega_0}\frac{\partial \omega}{\partial \omega_0} + \hat{\omega_1}\frac{\partial \omega}{\partial \omega_1} + \hat{\omega_2}\frac{\partial \omega}{\partial \omega_2} + \hat{\omega_3}\frac{\partial \omega}{\partial \omega_3} + \text{h.o.t.}$$

An alternative formulation of (4.1) must be used to account for the initial condition. The initial condition is accounted for in the variational form by integrating by parts on the time derivative.

$$\int_\Omega \rho c_p \left[u(\mathbf{x},0)p(\mathbf{x},0) - u(\mathbf{x},T)p(\mathbf{x},T)\right]\, dx = \int_0^T \int_\Omega \rho c_p \left(\frac{\partial u}{\partial t}p + \frac{\partial p}{\partial t}u\right)\, dxdt$$

Recognizing that $u^0(\mathbf{x}) = u(\mathbf{x},0)$ and *not testing* the equation at the final time, $p(\mathbf{x},T) = 0$, leads to the following

$$C(u,\beta;p) = \begin{aligned} & -\int_0^T \int_\Omega \rho c_p \frac{\partial p}{\partial t} u dxdt + \int_0^T \int_\Omega k(u,\beta)\nabla u \cdot \nabla p \, dxdt \\ & + \int_0^T \int_\Omega c_{blood}\omega(u,\beta)(u-u_a)p \, dxdt \\ & + \int_0^T \int_{\partial\Omega} hup \, dAdt + \int_\Omega u^0(\mathbf{x})p(\mathbf{x},0)\, dx \end{aligned}$$

Applying the definition of the partial Fréchet derivative to the variational PDE

$$C(u+\hat{u},\beta;p) = \begin{aligned} & -\int_0^T \int_\Omega \rho c_p \frac{\partial p}{\partial t}(u+\hat{u}) dxdt + k(u+\hat{u},\beta)\nabla(u+\hat{u}) \cdot \nabla p \, dxdt \\ & + \int_0^T \int_\Omega c_{blood}\omega(u+\hat{u},\beta)((u+\hat{u})-u_a)p \, dxdt \\ & + \int_0^T \int_{\partial\Omega} h(u+\hat{u})p \, dAdt + \int_\Omega u^0(\mathbf{x})p(\mathbf{x},0)\, dx \end{aligned}$$

Substituting the Taylor series expansion for k and ω, multiplying terms out, and rearranging terms gives

$$\begin{array}{c} C(u+\hat{u},\beta;p) \\ \quad - C(u,\beta;p) \end{array} = \left[\begin{array}{l} -\int_0^T \int_\Omega \rho c_p \frac{\partial p}{\partial t} \hat{u} \; dxdt + \int_0^T \int_{\partial\Omega} h\hat{u}p \; dAdt \\ \quad + \int_0^T \int_\Omega \left(k(u,\beta) \nabla \hat{u} \cdot \nabla p + \hat{u} \frac{\partial k}{\partial u} \nabla u \cdot \nabla p \right) \; dxdt \\ \quad + \int_0^T \int_\Omega \left(\omega(u,\beta) \hat{u} p + \hat{u} \frac{\partial \omega}{\partial u} (u - u_a) p \right) \; dxdt \\ \quad + \int_0^T \int_\Omega \left(\hat{u} k(u,\beta) \nabla \hat{u} \cdot \nabla p + \frac{1}{2} \hat{u}^2 \frac{\partial^2 k}{\partial u^2} \nabla u \cdot \nabla p \right) \; dxdt \\ \quad + \ldots \end{array} \right]$$

Notice that the terms involving the initial condition cancel out. Letting

$$D_u C(u,\beta;p)\hat{u} = \begin{array}{l} \int_0^T \int_\Omega \rho c_p \frac{\partial \hat{u}}{\partial t} p \; dxdt + \int_0^T \int_{\partial\Omega} h\hat{u}p \; dAdt \\ \quad + \int_0^T \int_\Omega k(u,\beta) \nabla \hat{u} \cdot \nabla p + \hat{u} \frac{\partial k}{\partial u} \nabla u \cdot \nabla p \; dxdt \\ \quad + \int_0^T \int_\Omega \omega(u,\beta) \hat{u} p + \hat{u} \frac{\partial \omega}{\partial u} (u - u_a) p \; dxdt \end{array}$$

implies that

$$|C(u+\hat{u},\beta;p) - C(u,\beta;p) - D_u C(u,\beta;p)\hat{u}| \leq \tilde{C} \|\hat{u}\|^2 \tag{4.5}$$

where the higher order terms of the thermal conductivity, $\frac{\partial^2 k}{\partial u^2}$, and perfusion, $\frac{\partial^2 \omega}{\partial u^2}$, are assumed bounded and hidden in the constant, $\tilde{C}$. For a particular test/adjoint function, p, the constant, $\tilde{C}$, also depends on the norm of the test/adjoint function, $\|p\|$, however, because $p \in \mathcal{V}$, the norm is always bounded and (4.5) holds. It follows from the definition that $D_u C(u,\beta;p)$ is the Fréchet derivative of C.

As a concrete example, consider objective function for the calibration problem,

$$\begin{aligned}
Q(u+\hat{u},\beta) - Q(u,\beta) &= \begin{bmatrix} \frac{1}{2}\int_0^T \int_\Omega (u+\hat{u}-u_{ideal})^2 \; dxdt \\ \qquad\qquad - \frac{1}{2}\int_0^T \int_\Omega (u-u_{ideal})^2 \; dxdt \end{bmatrix} \\
&= \left[\int_0^T \int_\Omega (u(\mathbf{x},t)-u_{ideal}(\mathbf{x},t))\hat{u}(\mathbf{x},t) + \hat{u}^2(\mathbf{x},t) \; dxdt \right]
\end{aligned}$$

Again, from recognizing the first order approximation of the objective function

$$|Q(u+\hat{u},\beta) - Q(u,\beta) - D_u Q(u,\beta)\hat{u}| \le C \; \|\hat{u}\|^2$$

the derivative of the objective function is

$$D_u Q(u,\beta)\hat{u} = \int_0^T \int_\Omega (u(\mathbf{x},t)-u_{ideal}(\mathbf{x},t))\hat{u}(\mathbf{x},t) \; dxdt$$

Notice that the variational form of the adjoint problem for the calibration, optimal control, and goal oriented error estimates are all essentially the same, the only difference being the source term $D_u Q(u(\beta),\beta)\hat{u}$ which depends on the quantity of interest. The strong form of the adjoint formulation is as follows

Given the spatially and temporally varying temperature field $u(\mathbf{x},t)$ find the Lagrange multiplier $p(\mathbf{x},t)$ such that

$$-\rho c_p \frac{\partial p}{\partial t} - \nabla \cdot (k(u)\nabla p) + \frac{\partial k}{\partial u}(u,\beta)\nabla u \cdot \nabla p + \omega(u,\beta)\, p \\ + \frac{\partial \omega}{\partial u}(u,\beta)\, p\, (u-u_a) = \begin{cases} u - u_{exp}(\mathbf{x},t) \text{ (calibration)} \\ u - \phi(\mathbf{x}) \text{ (optimal control)} \\ \chi(\mathbf{x})u \text{ (error estimate)} \end{cases} \text{ in } \Omega \tag{4.6}$$

given the Cauchy boundary condition

$$-k(u)\nabla p \cdot \mathbf{n} = h\, p \qquad \text{on } \partial\Omega$$

and the terminal condition

$$p(\mathbf{x},T) = 0 \qquad \text{in } \Omega$$

4.2 Finite Element Discretization

The gradient (4.4) that drives the optimization of Pennes model is computed using a Galerkin finite element method. The discretization framework follows the work of Demkowicz [16]. The computational domain is formed by a partition of the space-time domain $\Omega_T = \Omega \times (0,T]$. The spatial domain is a union of a $N_{el} < \infty$ compact, connected, Lipschitz sets K_m with non-empty interiors such that

$$\bar{\Omega} = \bigcup_{m=1}^{N_{el}} K_m \qquad \text{int}(K_m) \bigcap \text{int}(K_n) = \emptyset \ , \ m \neq n$$

The time span of interest, $(0,T]$, is partitioned into equally spaced intervals

$$t_0 = 0 < t_1 < t_2 < ... < t_{N_{step}} = T$$

Each element of the computational domain, K_m, is the image of the master element, $\hat{K} = (0,1)^3$, under a bijective mapping,

$$\mathbf{x}_{K_m} : \hat{K} \rightarrow K_m$$

The space of functions considered on the master element is the tensor product of polynomial spaces with polynomial order p_i in the i^{th} direction.

$$X(\hat{K}) = \mathcal{P}^{p_1} \otimes \mathcal{P}^{p_2} \otimes \mathcal{P}^{p_3}$$

Let $S_h \subset H^1(\Omega)$ denote a conforming finite element space such that the restriction of a continuous function to an element K_m is a composition of a master element shape function with the inverse of the geometrical mapping, $\mathbf{x}_{K_m}^{-1}$

$$S_h = \{u : u \text{ is continuous and } u|_{K_m} \in X(K_m) \ \ \forall K_m \subset \Omega\} \tag{4.7}$$

where

$$X(K_m) = \left\{ u = \hat{u} \circ \mathbf{x}_{K_m}^{-1} : \hat{u} \in X(\hat{K}) \right\}$$

The subscript h denotes the maximum diameter over the finite elements that partition the domain.

$$h = \max_{K_m \in \Omega} \text{ diam } (K_m) \qquad \text{diam } (K_m) = max_{x_1, x_2 \in K_m} \|x_1 - x_2\|$$

The following interpolation estimate of $H^1(\Omega)$ by the so-called Projection Based Interpolation [15] operator is used in deriving *a priori* estimates.

Theorem 4.2.1. *For every $\epsilon > 0$, there exist a constant $C = O(\epsilon^{-1})$ such that*

$$||u - \Pi^{hp} u||_{H^1(K_m)} \leq C h_{K_m}^{min\{p-1,r\}} p^{-(r-\epsilon)} ||u||_{H^{1+r}(K_m)}$$

for every $u \in H^r(K_m), r > \frac{1}{2}$

Where h_{K_m} denotes the diameter of the element K_m. Notice that extra regularity of the solution is needed. For the estimates, the result will be used in a global form with $r = 1$.

$$\begin{aligned} ||u - \Pi^{hp} u||_{H^1(\Omega)} &\leq C \sum_{K_m} h_{K_m}^{min\{p-1,1\}} p_{K_m}^{-(1-\epsilon)} ||u||_{H^2(K_m)} \\ &\leq C \frac{h}{p} ||u||_{H^2(\Omega)} \end{aligned} \tag{4.8}$$

The following Galerkin representation of the temperature field and adjoint variable is assumed.

$$u(\mathbf{x}, t) = \sum_{k=1}^{N_{step}} \sum_{j=1}^{N_{dof}} \alpha_j^k(t) \phi_j(\mathbf{x}) \qquad p(\mathbf{x}, t) = \sum_{k=1}^{N_{step}} \sum_{i=1}^{N_{dof}} \lambda_i^k(t) \phi_i(\mathbf{x})$$

where N_{step} is the number of time steps, N_{dof} is the number of Galerkin coefficients, and ϕ_i's are the finite element shape functions of polynomial order p=1,2,3...

$$\alpha_j^k(t) = \begin{cases} \dfrac{t_k - t}{t_k - t_{k-1}} \alpha_j^{k-1} + \dfrac{t - t_{k-1}}{t_k - t_{k-1}} \alpha_j^k, \ t \in (t_{k-1}, t_k] \\ \qquad\qquad 0 \qquad\qquad\qquad , \ \text{otherwise} \end{cases}$$

$$\lambda_i^k(t) = \begin{cases} \lambda_i^k, \ t \in (t_{k-1}, t_k] \\ 0, \ \text{otherwise} \end{cases}$$

Although not explicitly indicated, the Galerkin coefficients of the solution are assumed to be function of the model parameters, i.e.

$$\alpha_j^k = \alpha_j^k(\beta_1^1, \beta_2^1, ..., \beta_L^M)$$

The time discretization of the power is assumed piece-wise constant in time, Figure 4.1.

$$P(t) = \begin{cases} P_k, & t \in [t_{k-1}, t_k) \\ 0, & \text{otherwise} \end{cases}$$

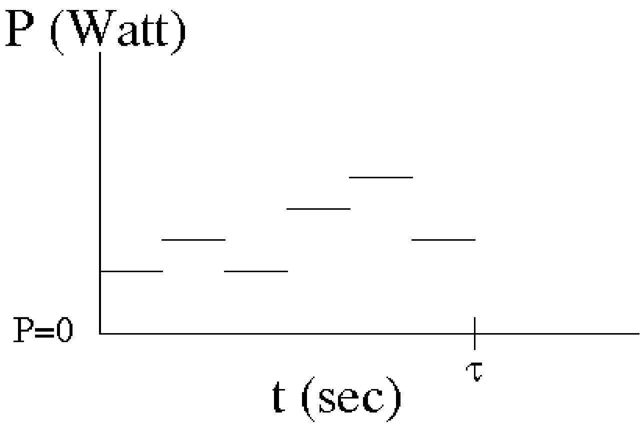

Figure 4.1: Piecewise constant power.

The spatial variation of the parameters fields is assumed to have the following Galerkin representation

$$
\begin{aligned}
k_0(\mathbf{x}) &= \sum_j k_0^j \psi^j(\mathbf{x}) \\
\omega_0(\mathbf{x}) &= \sum_j \omega_0^j \psi^j(\mathbf{x})
\end{aligned}
$$

where $\psi(\mathbf{x})$ are piece-wise constant across elements, K_m.

4.2.1 Outline of Gradient Computation

Before the involved details of the fully discretized gradient computation are given, a brief digression outlining the steps is provided. The order of the discretization and differentiation leads to two possibly non-commutative routes to computing the gradient.

$$\begin{tikzcd}
Q(u,\beta) \arrow[r] \arrow[d] & D(Q \circ u) = D_u Q(u,\beta) u'(\beta) + D_\beta Q(u,\beta) \arrow[d] \\
Q(u^h,\beta^h) \arrow[r] & \frac{\partial}{\partial \beta_i} Q(u^h,\beta^h) \overset{?}{=} D_u Q(u^h,\beta^h) u'(\beta^h) + D_\beta Q(u^h,\beta^h)
\end{tikzcd}$$

Here the objective function and Pennes solution is first discretized and then the derivatives are taken with respect to the Galerkin coefficients. The general form of the objective function is the space-time integral of a possibly nonlinear kernel that is function of the Pennes solution and the model parameters.

$$Q(u,\beta) = \int_0^T \int_\Omega f(u,\beta)\ dxdt$$

The variational form of the Pennes equation is similar, except the kernel is multiplied by a test function.

$$C(u,\beta,v) = \int_0^T \int_\Omega g(u,\beta) v\ dxdt$$

For computational purposes, we are interested in the derivative of the discretized objective function with respect to the model parameters.

$$\frac{\partial Q(u^h,\beta^h)}{\partial \beta_i} = \int_0^T \int_\Omega \left[\frac{\partial f}{\partial u}(u^h,\beta^h) \frac{\partial u^h}{\partial \beta_i} + \frac{\partial f}{\partial \beta}(u^h,\beta^h)\psi_i \right]\ dxdt$$

Similarly, the derivative of the discretized variational PDE is of interest.

$$\frac{\partial C(u^h,\beta^h;v^h)}{\partial \beta_i} = \int_0^T \int_\Omega \left[\frac{\partial g}{\partial u}(u^h,\beta^h) \frac{\partial u^h}{\partial \beta_i} + \frac{\partial g}{\partial \beta}(u^h,\beta^h)\psi_i \right]\ v^h\ dxdt$$

The discretized sensitivities, $\frac{\partial u^h}{\partial \beta_i}$, are interpreted as follows

$$\frac{\partial u^h}{\partial \beta_i} = \sum_{k=1}^{N_{step}} \sum_{j=1}^{N_{dof}} \frac{\partial \alpha_j^k(t)}{\partial \beta_i} \phi_j(\mathbf{x})$$

The gradient is computed in three steps.

1. For a given set of model parameters, β^h, find the solution to the Pennes equation, u^h, such that:

$$C(u^h,\beta^h;v^h) = 0 \qquad \forall v^h \in \mathcal{V}^h$$

2. Find the adjoint solution, p^h such that:

$$\int_0^T \int_\Omega \frac{\partial g}{\partial u}(u^h, \beta^h)\hat{u}^h \; p^h \; dxdt = \int_0^T \int_\Omega \frac{\partial f}{\partial u}(u^h, \beta^h)\hat{u}^h \; dxdt \qquad \forall \hat{u}^h \in \mathcal{V}^h$$

3. Using the Pennes solution, u^h, and the adjoint solution, p^h, compute the gradient.

$$\frac{\partial Q(u^h, \beta^h)}{\partial \beta^i} = \int_0^T \int_\Omega \frac{\partial f}{\partial \beta}(u^h, \beta^h)\psi_i \; dxdt - \int_0^T \int_\Omega \frac{\partial g}{\partial \beta}(u^h, \beta^h)\psi_i \; p^h \; dxdt$$

4.2.2 Time stepping

Assuming that the test function is piece-wise constant in time

$$v(\mathbf{x}, t) = \sum_{k=1}^{N_{step}} \sum_{i=1}^{N_{dof}} v_i^k(t)\phi_i(\mathbf{x}) \qquad\qquad v_i^k(t) = \begin{cases} v_i^k, & t \in (t_{k-1}, t_k] \\ 0, & \text{otherwise} \end{cases}$$

The governing equations (4.1) are solved with the following Crank-Nicolson time stepping scheme.

$$\begin{aligned} \Delta t_k \; & \int_\Omega \rho c_p \frac{u_k - u_{k-1}}{\Delta t_k} v_k + k(u_{k-\frac{1}{2}}, \mathbf{x}, \beta)\nabla u_{k-\frac{1}{2}} \cdot \nabla v_k \; dx \\ & + \Delta t_k \; \int_\Omega \omega(u_{k-\frac{1}{2}}, \mathbf{x}, \beta) c_{blood}(u_{k-\frac{1}{2}} - u_a) \; v_k \; dx \\ & + \Delta t_k \int_{\partial\Omega_C} h(u_{k-\frac{1}{2}} - u_\infty) \; v_k \; dA = \Delta t_k \; \int_\Omega Q_{laser}(\beta, \mathbf{x}, t_{k-\frac{1}{2}}) v_k \; dx \\ & \qquad - \int_{t_{k-1}}^{t_k} \int_{\partial\Omega_N} g \; v_k \; dA \qquad \forall v_k \qquad k = 1, 2, ..., N_{step} \end{aligned} \tag{4.9}$$

where (using Einstein summation notation)

$$u_k = \alpha_j^k \phi_j(\mathbf{x}) \qquad u_{k-\frac{1}{2}} = \frac{\alpha_j^{k-1} + \alpha_j^k}{2}\phi_j(\mathbf{x}) \qquad v_k = v_i^k \phi_i(\mathbf{x})$$

The discretization (4.9) is of the form

$$\boxed{\begin{array}{l} \text{find } \vec{\alpha}^k = (\alpha_1^k, \alpha_2^k, ...) \text{ s.t.} \\ \qquad \vec{f}(\vec{\alpha}^k) = \vec{0} \end{array}}$$

The Jacobian of this system of equations is

$$\begin{aligned} \frac{\partial f_i}{\partial \alpha_j^k} =& \Delta t_k \int_\Omega \frac{\rho c_p}{\Delta t_k} \phi_j \phi_i \; dx + \Delta t_k \frac{1}{2} \int_{\partial \Omega_C} h \phi_j \; \phi_i \; dA \\ & + \Delta t_k \frac{1}{2} \int_\Omega \left(\frac{\partial k}{\partial u}(u_{k-\frac{1}{2}}, \mathbf{x}, \beta) \nabla u_{k-\frac{1}{2}} \phi_j + k(u_{k-\frac{1}{2}}, \mathbf{x}, \beta) \nabla \phi_j \right) \cdot \nabla \phi_i \; dx \\ & + \Delta t_k \frac{1}{2} \int_\Omega c_{blood} \left(\frac{\partial \omega}{\partial u}(u_{k-\frac{1}{2}}, \mathbf{x}, \beta) \left[u_{k-\frac{1}{2}} - u_a \right] + \omega(u_{k-\frac{1}{2}}, \mathbf{x}, \beta) \right) \phi_j \phi_i dx \end{aligned}$$

4.2.3 The Adjoint Gradient

The Adjoint Gradient of the quantity of interest is constructed from the derivative of the discretized equations with respect to a single model variable. The chain rule is used to compute the gradient of the quantity of interest for the optimization. The initial condition does not depend on the model parameters, $\frac{\partial u_0}{\partial \beta_i} = 0$.

$$\frac{\partial}{\partial \beta_i} Q(u(\beta, \mathbf{x}, t), \beta) = \sum_{k=1}^{N_{step}} \frac{\partial Q}{\partial u_k} \frac{\partial u_k}{\partial \beta_i}$$

The derivative of the discretized state equations (4.9) with respect to a single model variable yields the following.

$$\begin{aligned} \frac{\partial C(u, \beta, v)}{\partial \beta_i} =& \Delta t_k \int_\Omega \frac{\rho c_p}{\Delta t_k} \left(\frac{\partial u_k}{\partial \beta} - \frac{\partial u_{k-1}}{\partial \beta} \right) v_k \; dx \\ & + \Delta t_k \int_\Omega \frac{\partial k}{\partial u}(u_{k-\frac{1}{2}}, \mathbf{x}, \beta) \frac{1}{2} \left[\frac{\partial u_{k-1}}{\partial \beta} + \frac{\partial u_k}{\partial \beta} \right] \nabla u_{k-\frac{1}{2}} \cdot \nabla v_k \; dx \\ & + \Delta t_k \int_\Omega k(u_{k-\frac{1}{2}}, \mathbf{x}, \beta) \frac{1}{2} \left[\nabla \frac{\partial u_{k-1}}{\partial \beta} + \nabla \frac{\partial u_k}{\partial \beta} \right] \cdot \nabla v_k \; dx \end{aligned}$$

$$
\begin{aligned}
&+ \Delta t_k \int_\Omega c_{blood} \frac{\partial \omega}{\partial u}(u_{k-\frac{1}{2}}, \mathbf{x}, \beta) \frac{1}{2} \left[\frac{\partial u_{k-1}}{\partial \beta} + \frac{\partial u_k}{\partial \beta} \right] \left(u_{k-\frac{1}{2}} - u_a \right) v_k dx \\
&+ \Delta t_k \int_\Omega c_{blood} \omega(u_{k-\frac{1}{2}}, \mathbf{x}, \beta) \frac{1}{2} \left[\frac{\partial u_{k-1}}{\partial \beta} + \frac{\partial u_k}{\partial \beta} \right] v_k \; dx \\
&+ \Delta t_k \int_{\partial \Omega_C} \frac{h}{2} \left[\frac{\partial u_{k-1}}{\partial \beta} + \frac{\partial u_k}{\partial \beta} \right] \; v_k \; dA \\
&+ \Delta t_k \int_\Omega \frac{\partial k}{\partial \beta}(u_{k-\frac{1}{2}}, \mathbf{x}, \beta) \nabla u_{k-\frac{1}{2}} \cdot \nabla v_k \; dx \\
&+ \Delta t_k \int_\Omega c_{blood} \frac{\partial \omega}{\partial \beta}(u_{k-\frac{1}{2}}, \mathbf{x}, \beta) \left(u_{k-\frac{1}{2}} - u_a \right) v_k \; dx \\
&- \Delta t_k \; \int_\Omega \frac{\partial Q_{laser}}{\partial \beta}(\beta, \mathbf{x}, t_k) v_k \; dx = 0 \qquad k = 1, 2, ..., N_{step}
\end{aligned}
$$

Solving for the adjoint variable, p_k, such that

$$
\begin{aligned}
\Delta t_k \; & \int_\Omega \frac{\rho c_p}{\Delta t_k} \hat{u} p_k + \frac{1}{2} \frac{\partial k}{\partial u}(u_{k-\frac{1}{2}}, \mathbf{x}, \beta) \hat{u} \nabla u_{k-\frac{1}{2}} \cdot \nabla p_k \; dx \\
& +\Delta t_k \; \int_\Omega \frac{1}{2} \frac{\partial \omega}{\partial u}(u_{k-\frac{1}{2}}, \mathbf{x}, \beta) \hat{u} \left(u_{k-\frac{1}{2}} - u_a \right) p_k \; dx \\
& + \Delta t_k \int_\Omega \frac{1}{2} k(u_{k-\frac{1}{2}}, \mathbf{x}, \beta) \nabla \hat{u} \cdot \nabla p_k \; dx + \frac{1}{2} \omega(u_{k-\frac{1}{2}}, \mathbf{x}, \beta) \hat{u} p_k \; dx \\
& + \Delta t_k \int_{\partial \Omega_C} \frac{h}{2} \hat{u} p_k \; dA = \int_\Omega \delta Q_k \hat{u} \; dx \qquad \forall \hat{u}, \qquad k = N_{step}
\end{aligned}
$$

and

$$
\begin{aligned}
\Delta t_k \; & \int_\Omega \frac{\rho c_p}{\Delta t_k} \hat{u} p_k + \frac{1}{2} \frac{\partial k}{\partial u}(u_{k-\frac{1}{2}}, \mathbf{x}, \beta) \hat{u} \nabla u_{k-\frac{1}{2}} \cdot \nabla p_k \\
& + \Delta t_k \; \int_\Omega \frac{1}{2} \frac{\partial \omega}{\partial u}(u_{k-\frac{1}{2}}, \mathbf{x}, \beta) \hat{u} \left(u_{k-\frac{1}{2}} - u_a \right) p_k \; dx \\
& + \Delta t_k \int_\Omega \frac{1}{2} k(u_{k-\frac{1}{2}}, \mathbf{x}, \beta) \nabla \hat{u} \cdot \nabla p_k \; dx + \frac{1}{2} \omega(u_{k-\frac{1}{2}}, \mathbf{x}, \beta) \hat{u} p_k \; dx \\
& + \Delta t_k \int_{\partial \Omega_C} \frac{h}{2} \hat{u} p_k \; dA = \int_\Omega \delta Q_k \hat{u} \; dx
\end{aligned}
$$

$$
- \left(\begin{array}{l}
-\Delta t_{k+1} \int_\Omega \frac{\rho c_p}{\Delta t_{k+1}} \hat{u} p_{k+1} + \frac{1}{2} \frac{\partial k}{\partial u}(u_{k+\frac{1}{2}}, \beta) \hat{u} \nabla u_{k+\frac{1}{2}} \cdot \nabla p_{k+1} \\
\qquad + \Delta t_{k+1} \int_\Omega \frac{1}{2} \frac{\partial \omega}{\partial u}(u_{k+\frac{1}{2}}, \beta) \hat{u} \left(u_{k+\frac{1}{2}} - u_a \right) p_{k+1} \, dx \\
\qquad + \Delta t_{k+1} \int_\Omega \frac{1}{2} k(u_{k+\frac{1}{2}}, \beta) \nabla \hat{u} \cdot \nabla p_{k+1} \, dx \\
\qquad + \Delta t_{k+1} \int_\Omega \frac{1}{2} \omega(u_{k+\frac{1}{2}}, \beta) \hat{u} p_{k+1} \, dx \\
\qquad + \Delta t_{k+1} \int_{\partial \Omega_C} \frac{h}{2} \hat{u} p_{k+1} \, dA
\end{array} \right)
$$

$$
\forall \hat{u}, \qquad k = N_{step} - 1, N_{step} - 2, ..., 1
$$

implies that the numerical gradient of the quantity of interest may be computed as follows.

$$
\frac{\partial Q(u,\beta)}{\partial \beta} = \sum_{k=1}^{N_{step}} \left(\begin{array}{l}
-\Delta t_k \int_\Omega \frac{\partial k}{\partial \beta}(u_{k-\frac{1}{2}}, \mathbf{x}, \beta) \nabla u_{k-\frac{1}{2}} \cdot \nabla p_k \, dx \\
-\Delta t_k \int_\Omega c_{blood} \frac{\partial \omega}{\partial \beta}(u_{k-\frac{1}{2}}, \mathbf{x}, \beta) \left(u_{k-\frac{1}{2}} - u_a \right) p_k \, dx \\
+\Delta t_k \int_\Omega \frac{\partial Q_{laser}}{\partial \beta}(\beta, \mathbf{x}, t_k) p_k \, dx
\end{array} \right)
$$

When the temperature field, $u(\mathbf{x}, t)$, and the adjoint variable, $p(\mathbf{x}, t)$, are known, the explicit form of the first variation of any particular quantity of interest is as follows.

$$
\begin{aligned}
\frac{\delta Q}{\delta k_0} &= -\int_0^T \int_\Omega \nabla u \cdot \nabla p \; \hat{k}_0 \; dxdt \\
\frac{\delta Q}{\delta k_1} &= -\int_0^T \int_\Omega atan(k_2 \; (u - k_3)) \nabla u \cdot \nabla p \; \hat{k}_1 \; dxdt \\
\frac{\delta Q}{\delta k_2} &= -\int_0^T \int_\Omega \frac{k_1 \; (u - k_3)}{1 + k_2^2 \; (u - k_3)^2} \nabla u \cdot \nabla p \; \hat{k}_2 \; dxdt \\
\frac{\delta Q}{\delta k_3} &= -\int_0^T \int_\Omega \frac{-k_1 \; k_2}{1 + k_2^2 \; (u - k_3)^2} \nabla u \cdot \nabla p \; \hat{k}_3 \; dxdt
\end{aligned}
$$

$$
\begin{aligned}
\frac{\delta Q}{\delta \omega_0} &= -\int_0^T \int_\Omega (u-u_a)p\ \hat{\omega}_0(\mathbf{x})\ dxdt + \int_\Omega \omega_0(\mathbf{x})\ \hat{\omega}_0(\mathbf{x})\ dx \\
\frac{\delta Q}{\delta \omega_1} &= -\int_0^T \int_\Omega atan(\omega_2(u-\omega_3))(u-u_a)p\ \hat{\omega}_1\ dxdt \\
\frac{\delta Q}{\delta \omega_2} &= -\int_0^T \int_\Omega \frac{\omega_1\ (u-\omega_3)}{1+\omega_2^2(u-\omega_3)^2}(u-u_a)p\ \hat{\omega}_2\ dxdt \\
\frac{\delta Q}{\delta \omega_3} &= -\int_0^T \int_\Omega \frac{-\omega_1\ \omega_2}{1+\omega_2^2(u-\omega_3)^2}(u-u_a)p\ \hat{\omega}_3\ dxdt
\end{aligned}
$$

$$
\begin{aligned}
\frac{\delta Q}{\delta P} &= \int_0^T \int_\Omega \frac{3\ \mu_a\ \mu_{tr} \exp(-\mu_{eff}\|\mathbf{x}-\mathbf{x}_0\|)}{4\ \pi\ \|\mathbf{x}-\mathbf{x}_0\|}\ p\ \hat{P}(t) dxdt \\
\frac{\delta Q}{\delta \mu_a} &= \int_0^T \int_\Omega \left(\begin{array}{l} 3P(t)\ \dfrac{\exp(-\mu_{eff}\|\mathbf{x}-\mathbf{x}_0\|)}{4\pi\|\mathbf{x}-\mathbf{x}_0\|} \cdot \\ \quad \left(\mu_{tr}+\mu_a-\mu_{tr}\ \mu_a\|\mathbf{x}-\mathbf{x}_0\|\dfrac{3(\mu_a+\mu_{tr})}{2\mu_{eff}}\right)\ p\ \hat{\mu}_a \end{array} \right) dxdt \\
\frac{\delta Q}{\delta \mu_s} &= \int_0^T \int_\Omega \left(\begin{array}{l} 3P(t)\ \dfrac{\exp(-\mu_{eff}\|\mathbf{x}-\mathbf{x}_0\|)}{4\ \pi\ \|\mathbf{x}-\mathbf{x}_0\|} \cdot \\ \quad \left(\mu_a-\mu_{tr}\ \mu_a\|\mathbf{x}-\mathbf{x}_0\|\dfrac{3(\mu_a(1-\gamma))}{2\mu_{eff}}\right)\ p\ \hat{\mu}_s \end{array} \right) dxdt \\
\frac{\delta Q}{\delta x_0} &= \int_0^T \int_\Omega 3P(t)\mu_a\mu_{tr}(\mu_{eff}\|\mathbf{x}-\mathbf{x}_0\|+1)\frac{\exp(-\mu_{eff}\|\mathbf{x}-\mathbf{x}_0\|)}{4\ \pi\|\mathbf{x}-\mathbf{x}_0\|^3}(x-x_0)p\hat{x}_0 dxdt \\
\frac{\delta Q}{\delta y_0} &= \int_0^T \int_\Omega 3P(t)\mu_a\mu_{tr}(\mu_{eff}\|\mathbf{x}-\mathbf{x}_0\|+1)\frac{\exp(-\mu_{eff}\|\mathbf{x}-\mathbf{x}_0\|)}{4\ \pi\|\mathbf{x}-\mathbf{x}_0\|^3}(y-y_0)p\hat{y}_0 dxdt \\
\frac{\delta Q}{\delta z_0} &= \int_0^T \int_\Omega 3P(t)\mu_a\mu_{tr}(\mu_{eff}\|\mathbf{x}-\mathbf{x}_0\|+1)\frac{\exp(-\mu_{eff}\|\mathbf{x}-\mathbf{x}_0\|)}{4\ \pi\|\mathbf{x}-\mathbf{x}_0\|^3}(z-z_0)p\hat{z}_0 dxdt
\end{aligned}
$$

4.2.4 Calibration and Temperature Based Optimal Control

The same Galerkin representation is used for u^{ideal} as u.

$$
\begin{aligned}
Q(u(\beta),\beta) &= \frac{1}{2}\int_0^T \int_\Omega \rho c_p \chi(\mathbf{x})(u(\beta,\mathbf{x},t)-u^{ideal}(\mathbf{x},t))^2\ dxdt \\
&= \frac{1}{2}\sum_{k=1}^{N_{step}} \int_{t_{k-1}}^{t_k} \int_\Omega \rho c_p \chi(\mathbf{x})(u(\beta,\mathbf{x},t)-u^{ideal}(\mathbf{x},t))^2\ dxdt
\end{aligned}
$$

$$
= \frac{\Delta t_k}{6} \sum_{k=1}^{N_{step}} \int_{\Omega} \rho c_p \chi(\mathbf{x}) \left(\begin{aligned} & u_{k-1}^2 - 2u_{k-1}u_{k-1}^{ideal} + u_{k-1}u_k \\ & \qquad - u_{k-1}u^{ideal} + (u_{k-1}^{ideal})^2 \\ & \qquad - u_{k-1}^{ideal}u_k + u_{k-1}^{ideal}u_k^{ideal} \\ & \qquad + u_k^2 - 2u_k u_k^{ideal} + (u_k^{ideal})^2 \end{aligned} \right) dx
$$

Derivatives are taken with respect to the numerically computed quantity of interest.

$$
\begin{aligned}
\frac{\partial Q(u,\beta)}{\partial \beta_i} &= \sum_{k=1}^{N_{step}} \int_{t_{k-1}}^{t_k} \int_{\Omega} \rho c_p \chi(\mathbf{x}) (u(\beta,\mathbf{x},t) - u^{ideal}(\mathbf{x},t)) \frac{\partial u}{\partial \beta_i} \; dxdt \\
&= \sum_{k=1}^{N_{step}} \Delta t_k \int_{\Omega} \rho c_p \chi(\mathbf{x}) \left(\begin{aligned} & \left[\begin{aligned} & \frac{1}{3}(u_{k-1} - u_{k-1}^{ideal}) \\ & + \frac{1}{6}(u_k - u_k^{ideal}) \end{aligned} \right] \frac{\partial u_{k-1}}{\partial \beta_i} \\ & + \left[\begin{aligned} & \frac{1}{6}(u_{k-1} - u_{k-1}^{ideal}) \\ & + \frac{1}{3}(u_k - u_k^{ideal}) \end{aligned} \right] \frac{\partial u_k}{\partial \beta_i} \end{aligned} \right) dx
\end{aligned}
$$

which implies that

$$
\delta Q_k = \begin{cases} \rho c_p \chi(\mathbf{x}) \Delta t_k \left[\frac{1}{6}(u_{k-1} - u_{k-1}^{ideal}) + \frac{1}{3}(u_k - u_k^{ideal}) \right] & k = N_{step} \\ \rho c_p \chi(\mathbf{x}) \left(\begin{aligned} & \Delta t_k \left[\begin{aligned} & \frac{1}{6}(u_{k-1} - u_{k-1}^{ideal}) + \\ & \frac{1}{3}(u_k - u_k^{ideal}) \end{aligned} \right] \\ & + \Delta t_{k+1} \left[\begin{aligned} & \frac{1}{3}(u_k - u_k^{ideal}) \\ & + \frac{1}{6}(u_{k+1} - u_{k+1}^{ideal}) \end{aligned} \right] \end{aligned} \right) & k = N_{step} - 1, ..., 1 \end{cases}
$$

4.2.5 Damage Based Optimal Control

$$
\begin{aligned}
Q(u(\beta,\mathbf{x},t),\beta) &= \frac{1}{2}\int_{\Omega}\left(\int_0^T \varphi(u(\beta,\mathbf{x},t),t)\;dt - \varphi_{ideal}(\mathbf{x})\right)^2\;dx \\
&= \frac{1}{2}\int_{\Omega}\left(\sum_{k=1}^{N_{step}} \varphi(u_{k-\frac{1}{2}}(\beta),t_k)\;\Delta t_k - \varphi_{ideal}(\mathbf{x})\right)^2\;dx
\end{aligned}
$$

As before, derivatives are taken with respect to the numerically computed quantity of interest.

$$
\begin{aligned}
\frac{\partial Q(u,\beta)}{\partial \beta_i} &= \frac{1}{2}\int_{\Omega}\chi(\mathbf{x})\frac{\partial}{\partial\beta_i}\left(\sum_{k=1}^{N_{step}} \varphi(u_{k-\frac{1}{2}}(\beta),t_k)\;\Delta t_k - \varphi_{ideal}(\mathbf{x})\right)^2\;dx \\
&= \int_{\Omega}\chi(\mathbf{x})\left[\begin{array}{c}\left(\sum_{k=1}^{N_{step}} \varphi(u_{k-\frac{1}{2}}(\beta),t_k)\;\Delta t_k - \varphi_{ideal}(\mathbf{x})\right) \\ \cdot\left(\sum_{k=1}^{N_{step}} \frac{\partial\varphi}{\partial u}(u_{k-\frac{1}{2}}(\beta),t_k)\;\Delta t_k \frac{\partial u_{k-\frac{1}{2}}}{\partial\beta_i}\right)\end{array}\right]dx
\end{aligned}
$$

which implies that

$$
\delta Q_k = \begin{cases}
\displaystyle\int_{\Omega}\chi(\mathbf{x})\left[\begin{array}{l}\left(\begin{array}{r}\displaystyle\sum_{k=1}^{N_{step}} \varphi(u_{k-\frac{1}{2}}(\beta),t_k)\;\Delta t_k \\ -\;\varphi_{ideal}(\mathbf{x})\end{array}\right) \\ \cdot\,\dfrac{1}{2}\left(\dfrac{\partial\varphi}{\partial u}(u_{k-\frac{1}{2}}(\beta),t_k)\;\Delta t_k\right)\end{array}\right]dx & k = N_{step} \\
\displaystyle\int_{\Omega}\chi(\mathbf{x})\left[\begin{array}{l}\left(\begin{array}{r}\displaystyle\sum_{k=1}^{N_{step}} \varphi(u_{k-\frac{1}{2}}(\beta),t_k)\;\Delta t_k \\ -\;\varphi_{ideal}(\mathbf{x})\end{array}\right) \\ \cdot\,\dfrac{1}{2}\left(\begin{array}{l}\dfrac{\partial\varphi}{\partial u}(u_{k-\frac{1}{2}}(\beta),t_k)\Delta t_k \\ +\;\dfrac{\partial\varphi}{\partial u}(u_{k+\frac{1}{2}}(\beta),t_{k+1})\Delta t_{k+1}\end{array}\right)\end{array}\right]dx & k = N_{step}-1,...
\end{cases}
$$

Chapter 5

Results

Several main results are presented in this chapter. First, the Pennes model, calibrated using experimental MRTI data, is shown to provide accurate computational predictions for the laser heating of canine cerebral tissue, an excised canine prostate, and a tumor grown on a mouse's hind leg. These results serve to validate the model. The constitutive nonlinearites as well as the heterogeneity of the biological domain are shown to be important features of the model, and are characterized using an inverse analysis algorithm. Second,

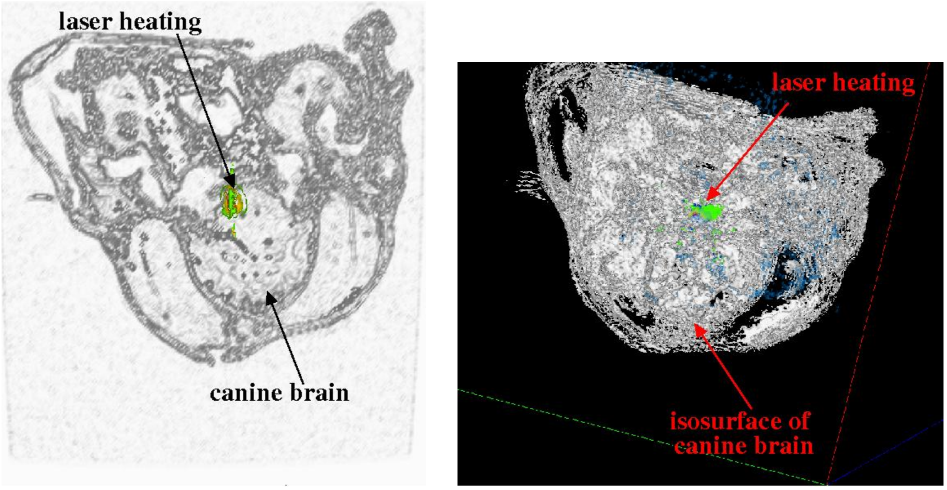

Figure 5.1: The visualization of a MRI brain scan of a canine is shown. A selected slice of the MRI brain data shows the brain and the region of the brain being heated with an interstitial laser fiber. An iso-surface visualization of canine MRI Brain Data is also provided.

results from optimal control computations are presented. Optimal temperature profiles for temperature-based control and the Arrhenius damage-based control are provided. Third, the overall computational feasibility of developing a laser treatment paradigm in which high performance computers control the bioheat data transferred from a remote site is demonstrated and the ability to perform real-time robust calibration and optimal control computation is shown. All computations use the GMRES linear solver and block Jacobi preconditioner available from PETSc [3]. A bound constrained quasi-Newton linesearch method available in TAO [6] is used for the optimization solution.

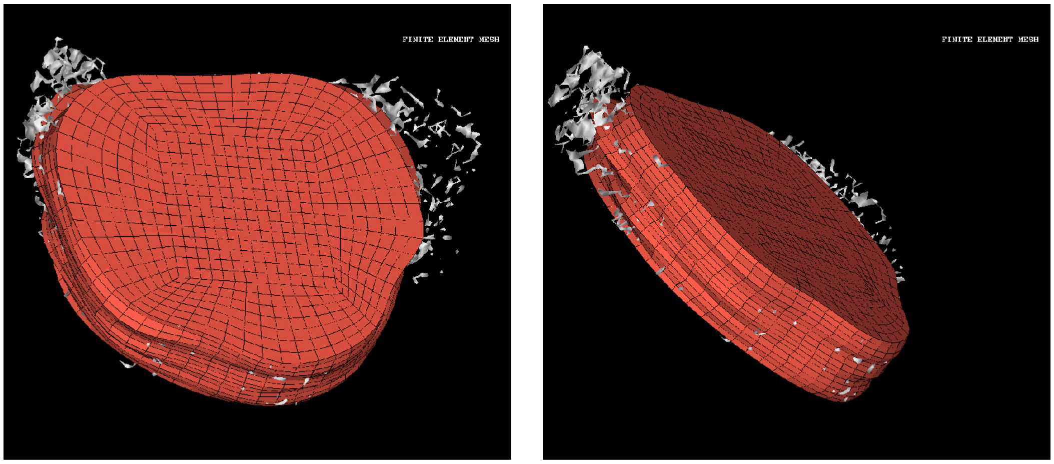

Figure 5.2: Finite Element Mesh of Canine MRI Brain Data

5.1 Model Calibration

Computations comparing the predictions of Pennes model to experimental MRTI taken from a canine brain show very good agreement, Figure 5.4. A manual craniotomy of a canine skull was preformed to allow insertion of an interstitial laser fiber. Thirty-six two dimensional 256×256 pixels MRI images,

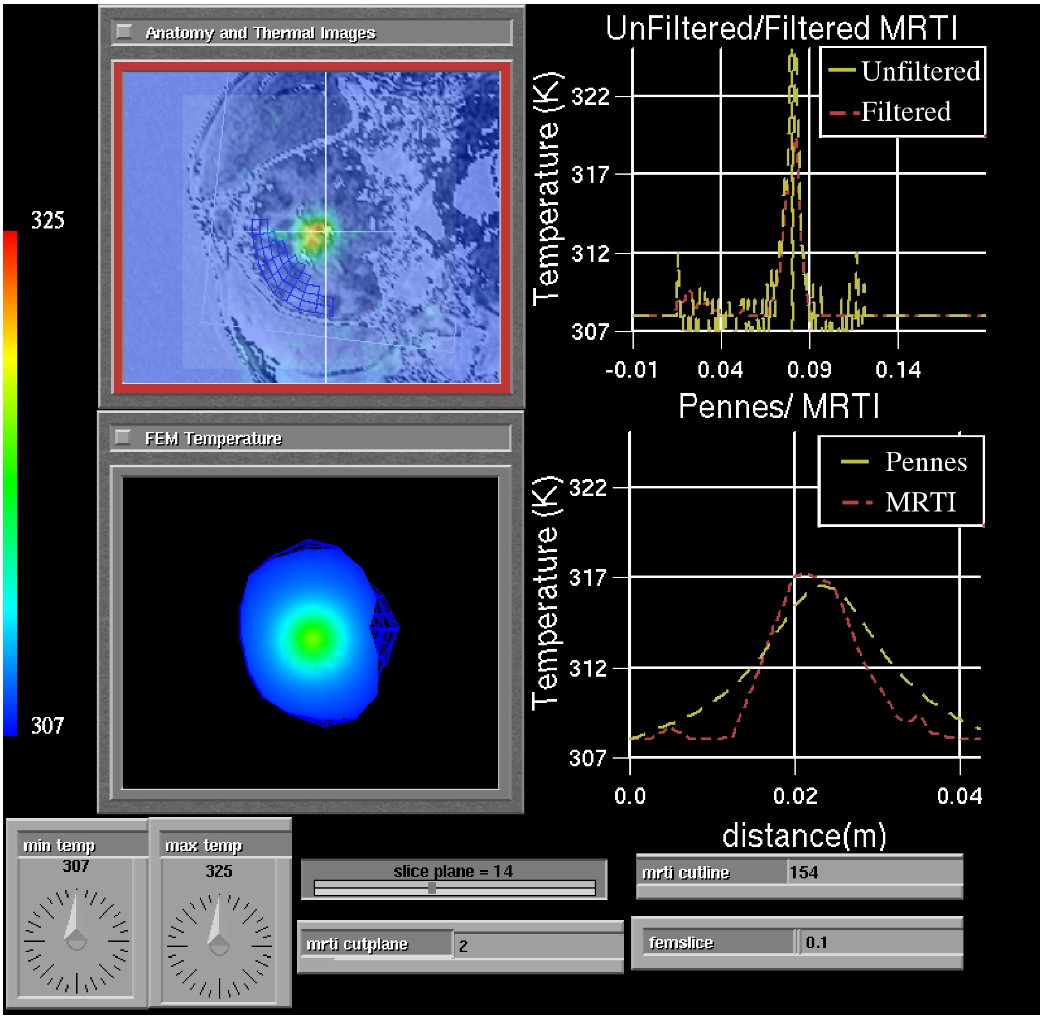

min temp 307

max temp 325

slice plane = 14

mrti cutline 154

mrti cutplane 2

femslice 0.1

Figure 5.3: Thermal images of in-vivo heating of a canine brain were taken every 6 seconds over a period of 12 mins. The top left shows the anatomy with a particular time instance of the thermal images overlaid. The linear Pennes equation was solved using CRC Handbook [18] perfusion and thermal conductivity values for canine brain and the bottom left shows the linear FEM prediction at the same time instance for comparison. The temperature range shown is from 307K-325K. The top right shows a cut-line through the thermal image data. The unfiltered and filtered image data are plotted along the cut-line. The bottom right compares the FEM predicted temperature and filtered thermal image along a cut-line through the FEM mesh.

Figure 5.1, of the canine brain were acquired. The field view was 200 mm×200 mm with each image spaced 1 mm apart. A finite element mesh of the biological domain generated from the MRI data is shown in Figure 5.2. The mesh consists of 8,820 linear elements with a total of 9,872 degrees of freedom. MRTI thermal imaging data was acquired in the form of five two dimensional 256×256 pixel images every six seconds for 120 time steps. The spacing between images was 3.5 mm. The MRTI data was filtered then projected onto the finite element mesh. The effect of calibrating the nonlinear perfusion, $\omega(u, \mathbf{x}, \beta)$, and thermal conductivity, $k(u, \mathbf{x}, \beta)$, parameters in Pennes model was studied. The FEM prediction using CRC Handbook [18] linear material coefficients, $k(u, \mathbf{x}, \beta) = .527[\frac{W}{mK}]$ and $\omega(u, \mathbf{x}, \beta) = 6.0[\frac{kg}{sm^3}]$, is shown in Figure 5.3. Figure 5.4 shows the FEM prediction using calibrated nonlinear coefficients. A plot of the material coefficients obtained is shown in Figure 2.5. The data shown in Figures 5.3 and 5.4 illustrate profiles at a particular time instance. The upper-right windows in Figures 5.3 and 5.4 each show a cut-line comparison of the filtered MRTI data with the unfiltered data. The upper-left windows in Figures 5.3 and 5.4 display an overlay of the MRTI thermal image onto the anatomical MRI image. Figure's 5.3 and 5.4 lower-left window shows a 2D temperature slice through the 3D domain. The lower-right window is a cut-line comparison of the filtered MRTI data to the FEM prediction. The accuracy of the predicted FEM solution shown in Figure 5.4 was obtained by inverting for the constitutive nonlinearities. The damage of the tissue is reflected in the decrease in perfusion for high temperatures within the damaged region and hyper perfusion surrounding the damage region. As shown in [26], the linear case captures the early time heating well, but the cut-lines Figures 5.3 and 5.4 illustrate that the material nonlinearities are necessary model the late time heat dissipation. The results presented in Figure 5.7 indicate that

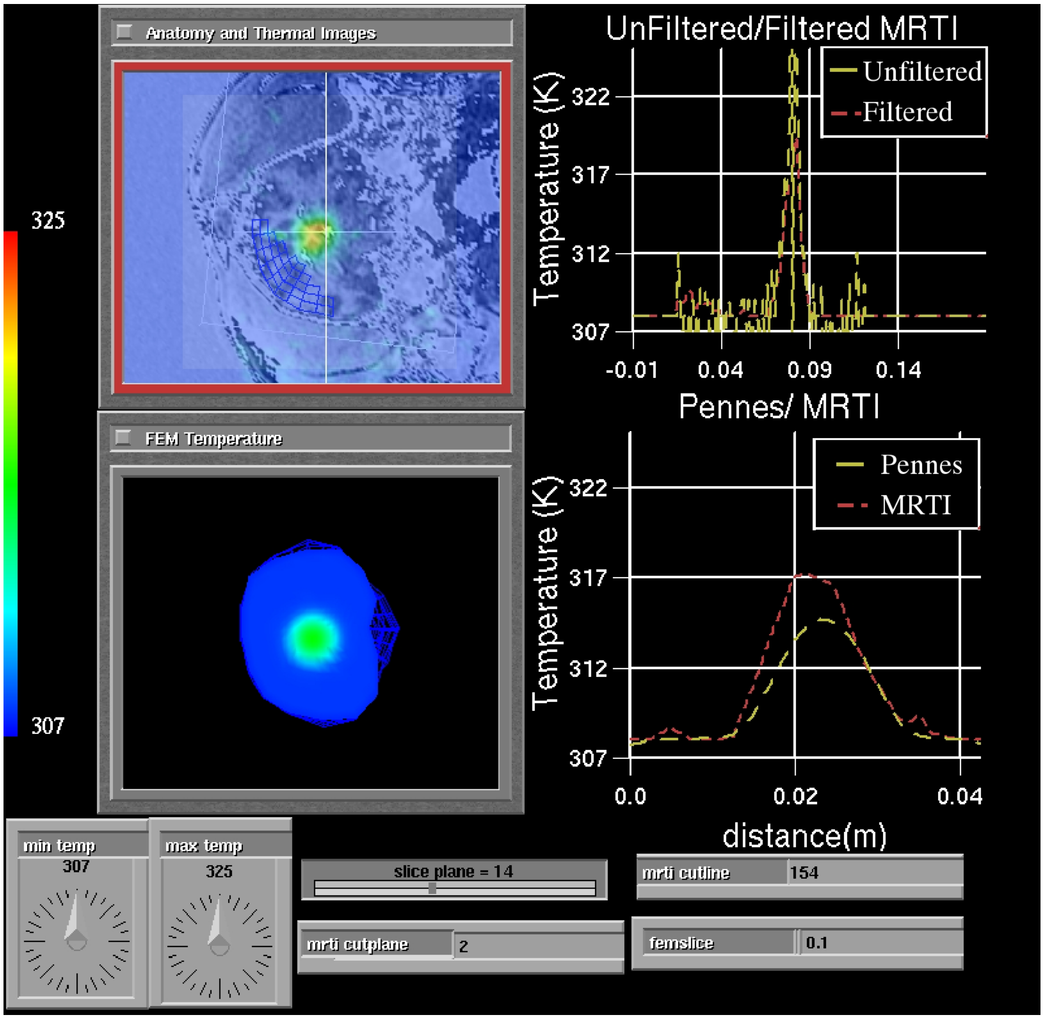

min temp 307

max temp 325

slice plane = 14

mrti cutline 154

mrti cutplane 2

femslice 0.1

Figure 5.4: Thermal images of in-vivo heating of a canine brain were taken every 6 seconds over a period of 12 mins. The top left shows the anatomy with a particular time instance of the thermal images overlaid. Pennes equation was solved with a set of nonlinear perfusion and thermal conductivity material coefficients that were calibrated to the thermal images and the bottom left shows the non-linear FEM prediction at the same time instance for comparison. The temperature range shown is from 307K-325K. The top right shows a cut-line through the thermal image data. The unfiltered and filtered image data are plotted along the cut-line. The bottom right compares the FEM predicted temperature and filtered thermal image along a cut-line through the FEM mesh.

a spatially varying inversion for the perfusion field should provide a means to further increase the accuracy of the FEM temperature prediction of the canine brain data, Figure 5.4.

5.1.1 Heterogeneous Tissue Calibration

Allowing the perfusion and thermal conductivity model parameters to vary as a spatial field is seen to have a significant effect on the model calibrations. Inverting for the spatial variation in the parameters embeds the biological tissue heterogeneity within the Pennes model. Imaging data of an external laser applied to a tumor grown on a mouse's hind leg was used to study the effect of the parameter field inversion, Figure 5.5. Sixty thermal images were acquired over an interval of 5 seconds. A single time instance of the data is shown in Figures 5.6 and 5.7. The field of view is $4{\times}6$ cm^2 and the

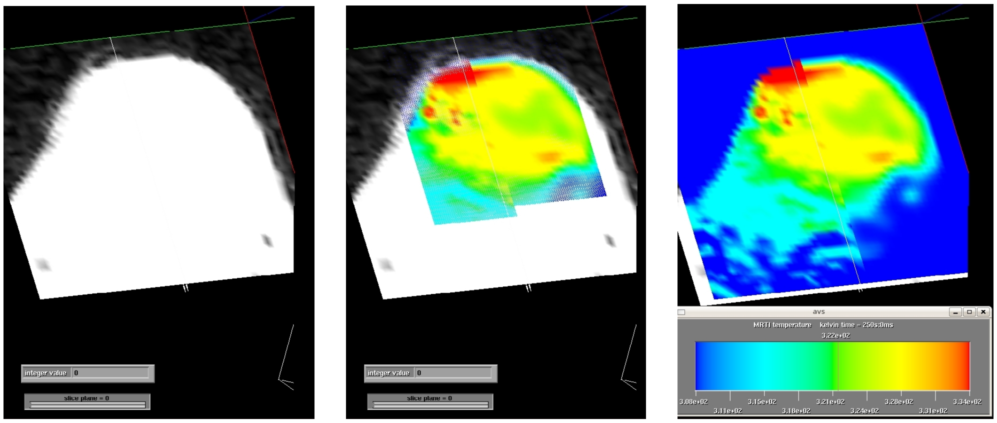

(a) (b) (c)

Figure 5.5: (a) MRI image of a mouse tumor, field of view is 4×6 cm^2 and thickness associated with the image is 3 mm. (b) a thermal image of the heating of the mouse tumor overlaid onto the MRI image. (c) a quantified thermal image of the mouse tumor with color scale from 308 K to 334 K.

thickness associated with the MRI/MRTI images is 3 mm. Figures 5.6 and 5.7 compare the FEM prediction using textbook linear material coefficients to the calibrated heterogeneous material coefficients applied to the in-vivo heating of a tumor grown on a mouse. The upper-right windows in Figures 5.6 and 5.7 each show a cut-line comparison of the filtered MRTI data with the unfiltered data. The upper-left windows in Figures 5.6 and 5.7 display an overlay of the MRTI thermal image onto the anatomical MRI image. The images are 49×56 pixels. Figures 5.6 and 5.7 lower-left windows show a 2D temperature slice through the 3D domain. The lower-right window is a cut-line comparison of the filtered MRTI data to the FEM prediction. The agreement between the predicted FEM solution and the MRTI thermal images shown in Figure 5.7 illustrates the importance of inverting for the field of material heterogeneity. Figure 5.7 represents the results of solving a parameter optimization problem with approximately 4,100 parameters. Figure 5.8 shows the optimizer evolution of the material heterogeneity inversion for the thermal conductivity fields and blood perfusion fields. The initial guess for the material coefficients was assumed homogeneous and the optimized determined a sufficient field variation of the parameters that allows Pennes model to accurately predict the temperature field seen in the thermal images. The values of the thermal conductivity field found by the optimizer are above the physical range seen in the CRC Handbook [18]. Future work includes correlating the computed inverted parameter field with the physical tissue.

5.2 Robust Real Time Computations

Every aspect of the control system is operational and has been tested on a phantom constructed of an excised canine prostate embedded within a

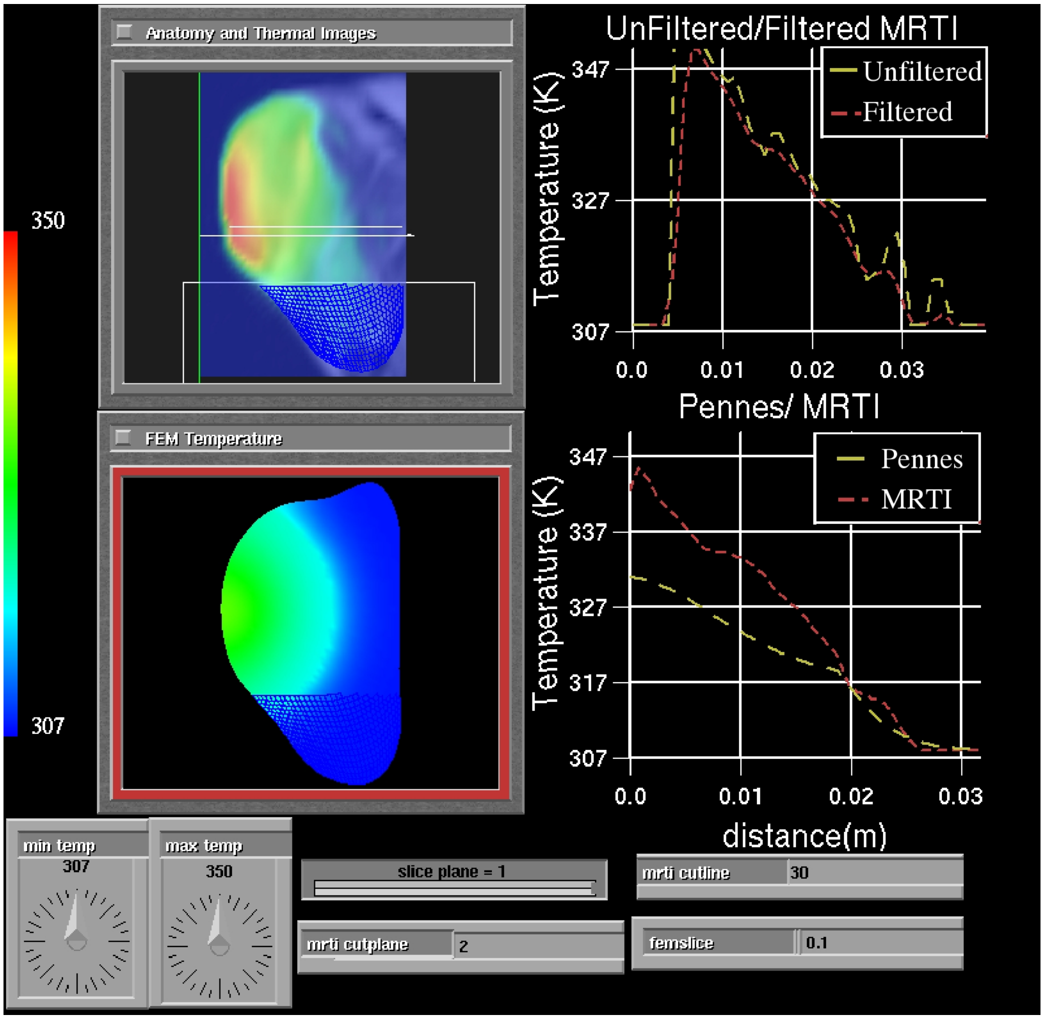

min temp 307

max temp 350

slice plane = 1

mrti cutline 30

mrti cutplane 2

femslice 0.1

Figure 5.6: Thermal images of in-vivo heating of a tumor grown on the hind leg of a mouse were taken every 5 seconds over a period of 5 mins. The top left shows the anatomy with a particular time instance of the thermal images overlaid. The linear Pennes equation was solved using CRC Handbook [18] perfusion and thermal conductivity values for the tissue and the bottom left shows the linear FEM prediction at the same time instance for comparison. The temperature range shown is from 307K-350K. The top right shows a cut-line through the thermal image data. The unfiltered and filtered image data are plotted along the cut-line. The bottom right compares the FEM predicted temperature and filtered thermal image along a cut-line through the FEM mesh.

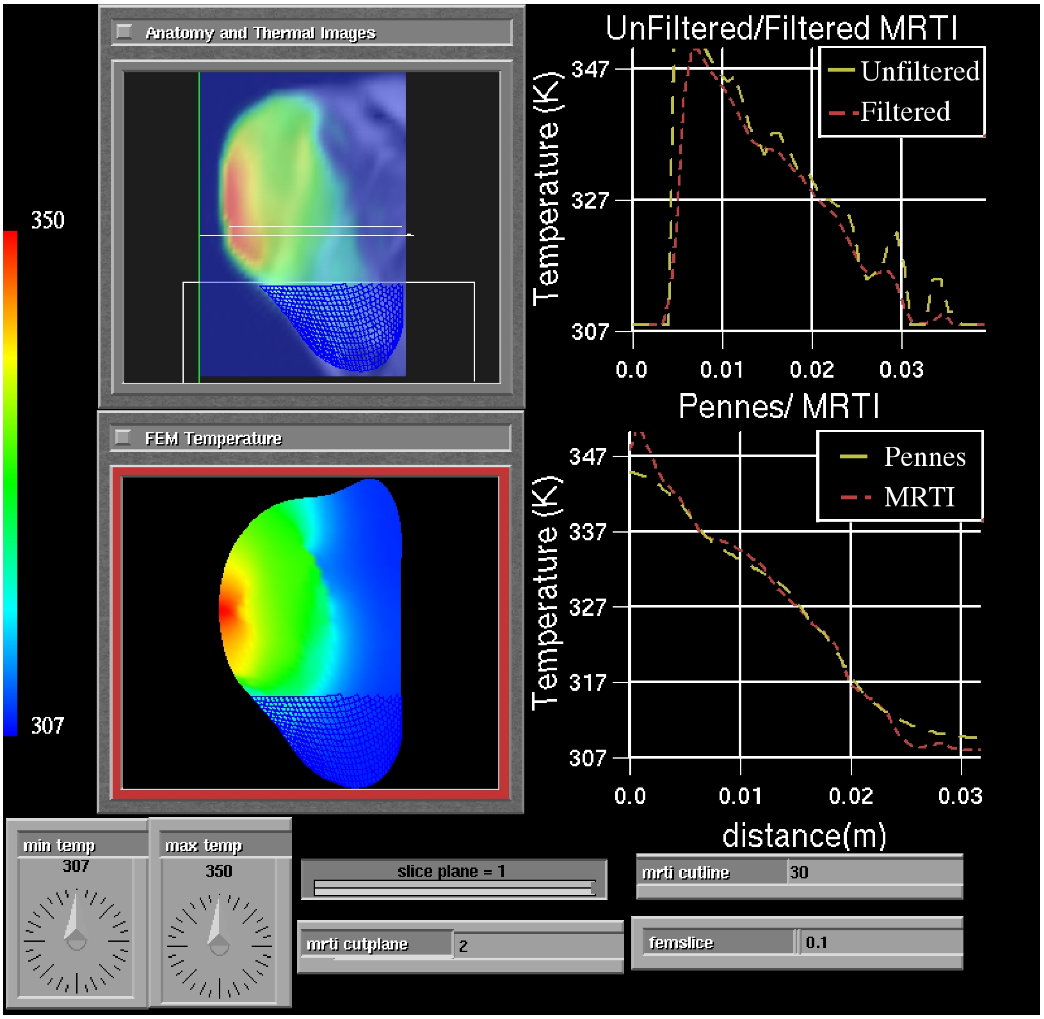

Figure 5.7: Thermal images of in-vivo heating of a tumor grown on a hind leg of a mouse were taken every 5 seconds over a period of 5 mins. The top left shows the anatomy at a particular time instance of the thermal images overlaid. The Pennes equation was solved with a spatially varying field of perfusion and thermal conductivity material that were calibrated to the thermal images. The bottom left image shows the non-linear FEM prediction at the same time instance for comparison. Approximately 4,100 model parameters were optimized to recover the material heterogeneity. The temperature range shown is from 307K-350K. The top right figure shows a cut-line through the thermal image data. The unfiltered and filtered image data are plotted along the cut-line. The bottom right panel compares the FEM predicted temperature and filtered thermal image along a cut-line through the FEM mesh.

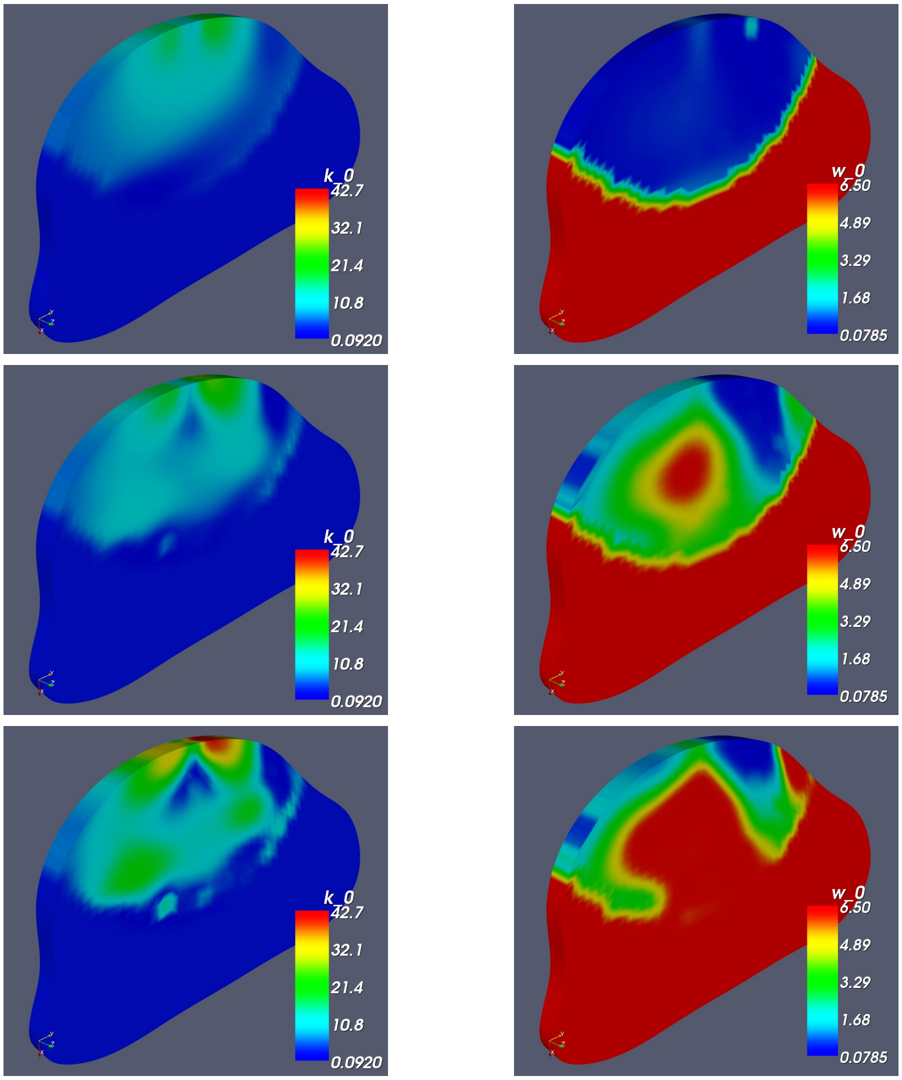

(a) (b)

Figure 5.8: Thermal imaging data was used to drive an inverse problem to recover the biological tissue heterogeneity. Approximately 4,100 model parameters representing the blood perfusion and thermal conductivity fields of the biological domain were optimized to allow the Pennes model to accurately predict the temperature field seen in the thermal images. As shown at the top of the figure, the parameter fields are initially assumed to be homogeneous. The evolution of the optimizer's inversion for the parameter fields is shown. Figures (a) and (b) shows the evolution of the thermal conductivity $[\frac{W}{mK}]$ and blood perfusion $[\frac{kg}{sm^3}]$ fields, respectively.

1% agar gel. This testing represents a project milestone. The phantom has provided an animal-free method of testing and debugging the entire control system. The phantom is meshed, registered, and the computational models in Austin control the heating. Thermal images of the heating are acquired and sent to the HP3d program; HP3d calibrates and optimizes the model parameters, and finally, a visualization of the entire process is provided in Houston. Figure 5.9 shows a particular time instance of the predicted heating of the phantom heated with an interstitial laser fiber during the pre-treatment phase (discussed in Chapter 3). At this point, only thermal images of the baseline temperature field are available and the the power profile shown reflects the initial experimental setup.

A visualization of the anatomy, predicted temperature contours, predicted damage contours, cutlines of the baseline thermal images, and cutlines of the heating predicted by Pennes model are shown. The anatomy images are used to obtain the initial coordinates of the laser tip in the FEM calculations. As illustrated by the initial power profile the phantom is to be pulsed heat with the laser source at 8 Watts for 30 seconds. Imaging of the heating and cooling is used for model calibration. The time period of no heating is the time allotted for the calibration and optimal control computations. The initial parameter for optimal control is 0.2 Watts for the remainder of the treatment. Figure 5.10 shows the same visualization of the experiment post calibration and post optimal control computation. The contour plots of the thermal images and the Pennes model predicted is seen to differ. As expected from modeling the medium as homogeneous with isotropic heating, the Pennes model prediction shows circular contours compared to the more elliptical shape seen in the thermal image contours. However, the particular time instance illustrates very good cutline agreement between the thermal images and the Pennes model prediction. Also shown are cutlines of the filtered and unfiltered thermal images. The initial pulse used for model calibration is seen to mildly damage the prostate before the optimal control portion of the experiment. The optimal power profile shown was computed to simulate the optimal heating of a tumor of radius 1.5cm. The profile shown maximizes damage to the tumor and minimizes damage to the surrounding healthy tissue

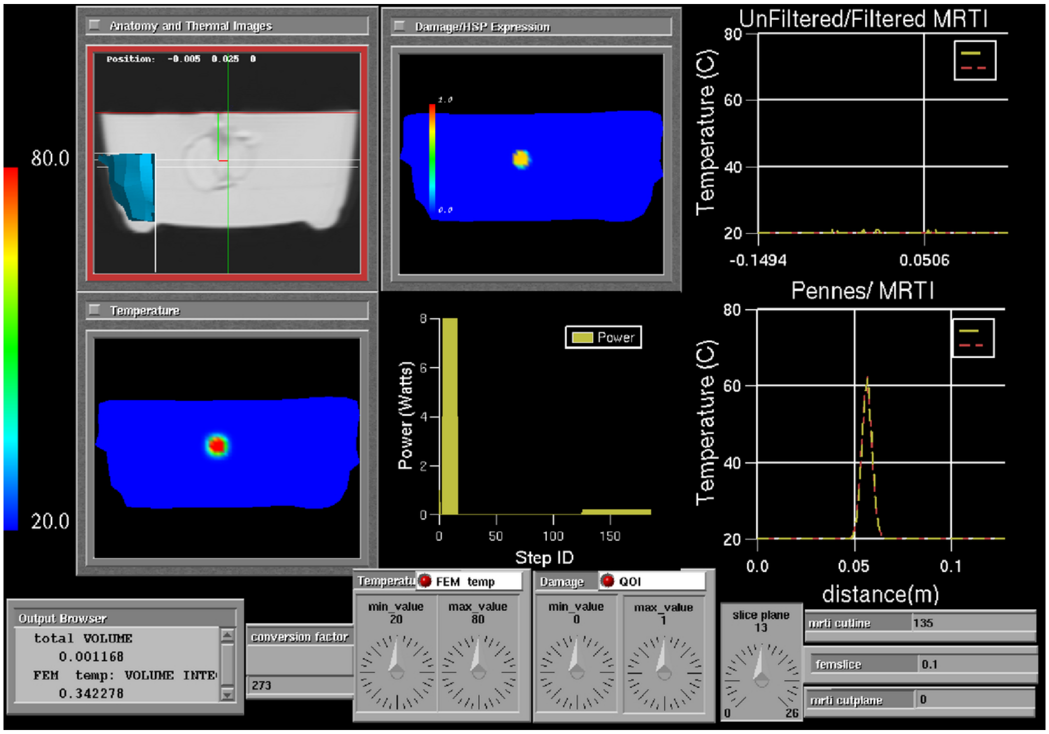

Position: -0.005 0.025 0

```
total VOLUME
   0.001168
FEM  temp: VOLUME INTE
   0.342278
```

conversion factor: 273

min_value 20

max_value 80

min_value 0

max_value 1

slice plane 13

mrti cutline 135

femslice 0.1

mrti cutplane 0

Figure 5.9: Every aspect of the control system has been tested on a phantom constructed of an excised canine prostate embedded within a 1% agar gel. Pre-operative computations illustrating visualizations of the anatomy, predicted temperature contours, predicted damage contours, cutlines of the thermal images, cutlines of the heating predicted by Pennes model, and the planned laser power as a function of time are shown.

by following a pulse heating with a tapering of the laser power. The tapering allows heat to diffuse through the tumor without overheating the healthy tissue.

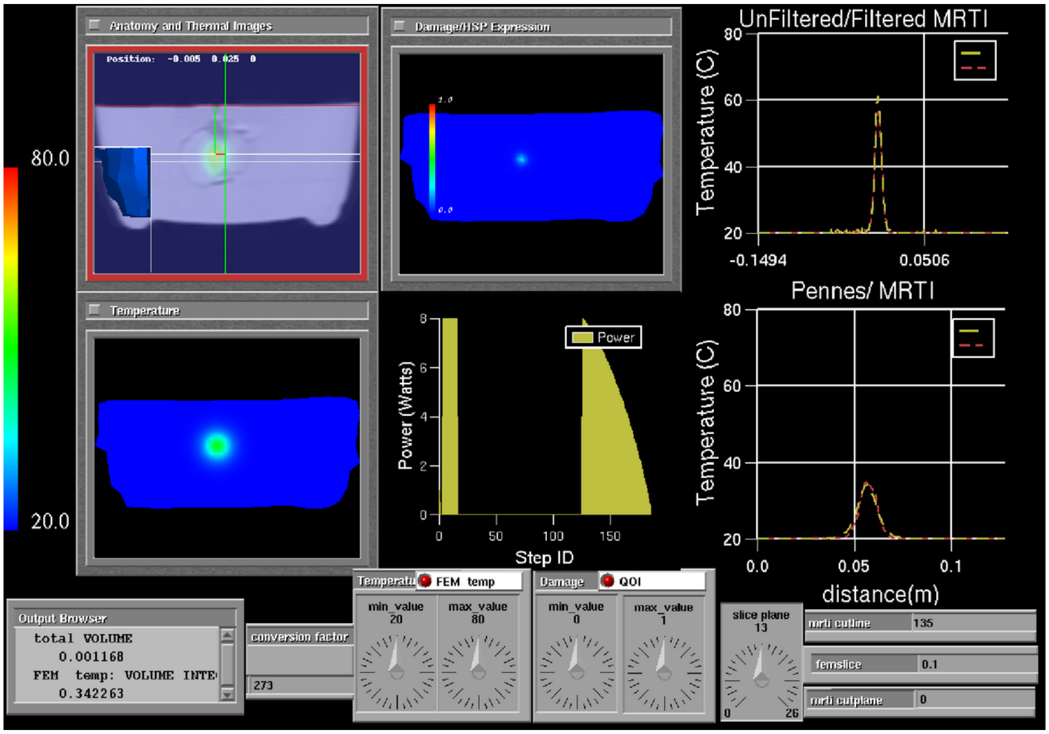

Output Browser

```
total VOLUME
   0.001168
FEM  temp: VOLUME INTE
   0.342263
```

conversion factor 273

mrti cutline 135

femslice 0.1

mrti cutplane 0

Figure 5.10: The control system testing on a phantom constructed of an excised canine prostate embedded within a 1% agar gel is shown. Intra-operative computations illustrating the visualizations of the anatomy, actual temperature contours, actual damage contours, cutlines of the thermal images, cutlines of the heating predicted by Pennes model, and the laser power modulated as a function of time are shown. The cutlines shown are at different spatial positions. Top-right is a thermal imaging cutline comparing the filtered and unfiltered data. Bottom-right is a a cutline through the finite element data comparing the Pennes model prediction to the thermal imaging data projected onto the finite element mesh.

The typical time duration of a laser treatment is about ten minutes.

During a ten minute span, one set of MRTI data is acquired every 5 seconds. The size of each set of MRTI data is around 330 kB (256×256×5 voxels) and the bandwidth of a commercial GigE Internet connection is approximately 300 kB/s. Accounting for connection latency, each set of MRTI data can be transferred between Houston and Austin in roughly one second. A finite element mesh consisting of approximately 10,000 degrees of freedom is sufficient to resolve the geometry of the biological domain. The execution time of a representative 10 second bioheat transfer simulation is presented in Figure 5.11. The execution times represent 10 nonlinear state solves of the Pennes model

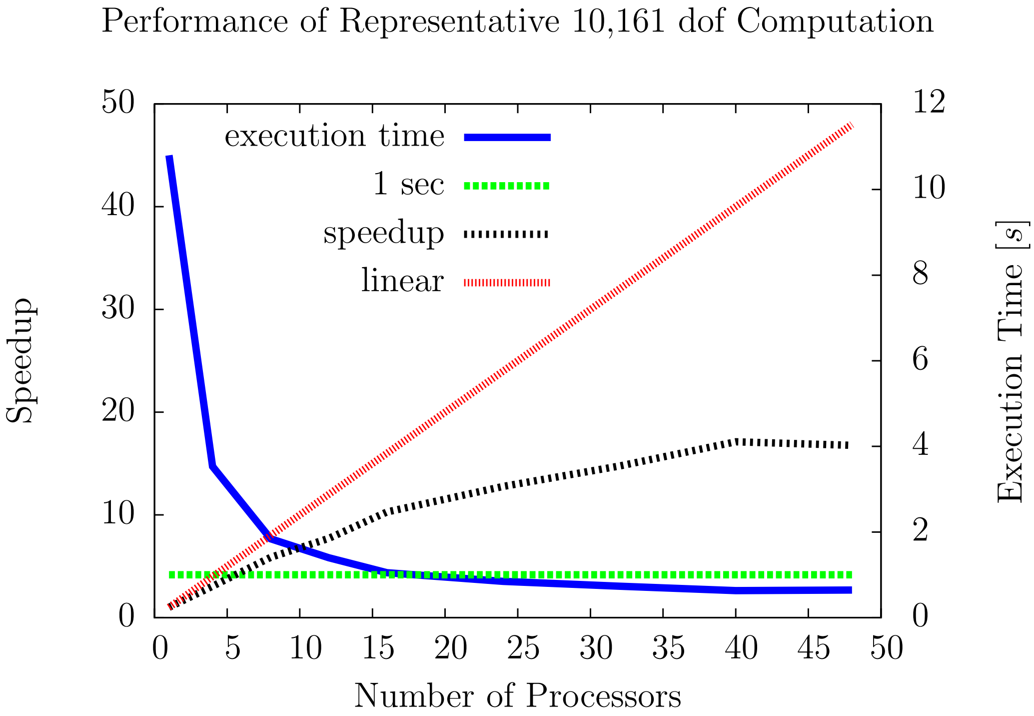

Figure 5.11: Shown is the speedup as a function of processors and execution time for a representative 10 second simulation (10 nonlinear state solve combined with 10 linear adjoint solve on 10000 dof system)

(10 one second time steps) combined with 10 linear adjoint solves to be used for calibration, optimal control, and/or error estimates. Computations were done at TACC, the Texas Advanced Computing Center, on Dual-Core Linux Cluster. Each node of the cluster contains two Xeon Intel Duo-Core 64-bit processors (4 cores in all) on a single board, as an SMP unit. The core frequency is 2.66GHz and supports 4 floating-point operations per clock period. Each node contains 8GB of memory. The fastest time recorded is .67 seconds, meaning that in a real time 10 second span the Pennes model can predict out to more than two minutes. Equivalently, in a 10 second time span roughly 14 corrections can be made to calibrate the model coefficients or optimize the laser parameters.

The results shown in Figure 5.11 indicate that it is feasible to perform roughly ten function/gradient evaluations during a real time computation. An important question that remains is: *Will the the optimizer converge to a solution in the time allowed for a real time computation? Furthermore, is the convergence of the optimizer robust?* "Robust" in this context implies that the optimization process will converge independently of the finite element discretization, independent of the initial guess of the model parameters in physical parameter space, and independent of which model parameters are optimized. With regard to the latter criteria, the calibration is seen to be most sensitive to the absorption coefficient μ_a, the linear term in the thermal conductivity, k_0, and the linear term in the blood perfusion, ω_0. For example, attempting model calibration with only k_0 and ω_0 is found to be insufficient for obtaining an accurate model calibration, i.e., the optimizer is unable

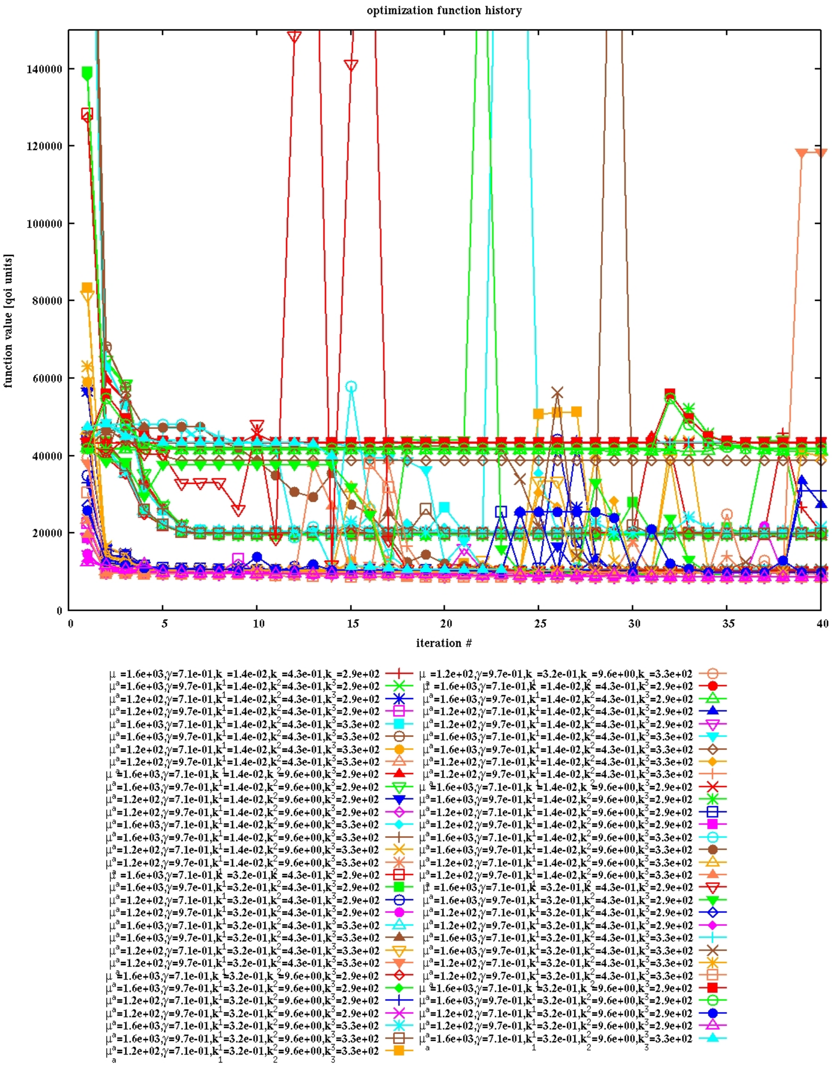

Figure 5.12: Optimization convergence plots for the calibration problem. The number of entries in the legend of this graph illustrates the extent to which parameter space was explored. The legend contains the permutations of the high and low values of physically meaningful model parameters as well as different meshes were used. The graph demonstrates that with reasonable initial guesses for the model coefficients the calibration problem converges in real-time in under ten function evaluations. The space-time norm of the MRTI temperature field is $\|u_{ideal}\| = 5.585e+10$. Normalizing by this value, the error between the computed solution and the thermal images satisfies $\frac{\|u^h - u^h_{ideal}\|}{\|u^h_{ideal}\|} < 1\%$

to decrease the objective function. Properties of the former two requirements of robustness were studied for calibration, temperature based optimal control and damage based optimal control. Shown in Figure 5.12 is the optimizer convergence plots when using permutations over the high and low values of physically meaningful model parameters as the initial guess for calibration performed in Figure 5.9. Meshes of 33,096 degrees of freedom and 87,830 degrees of freedom were used in the study.

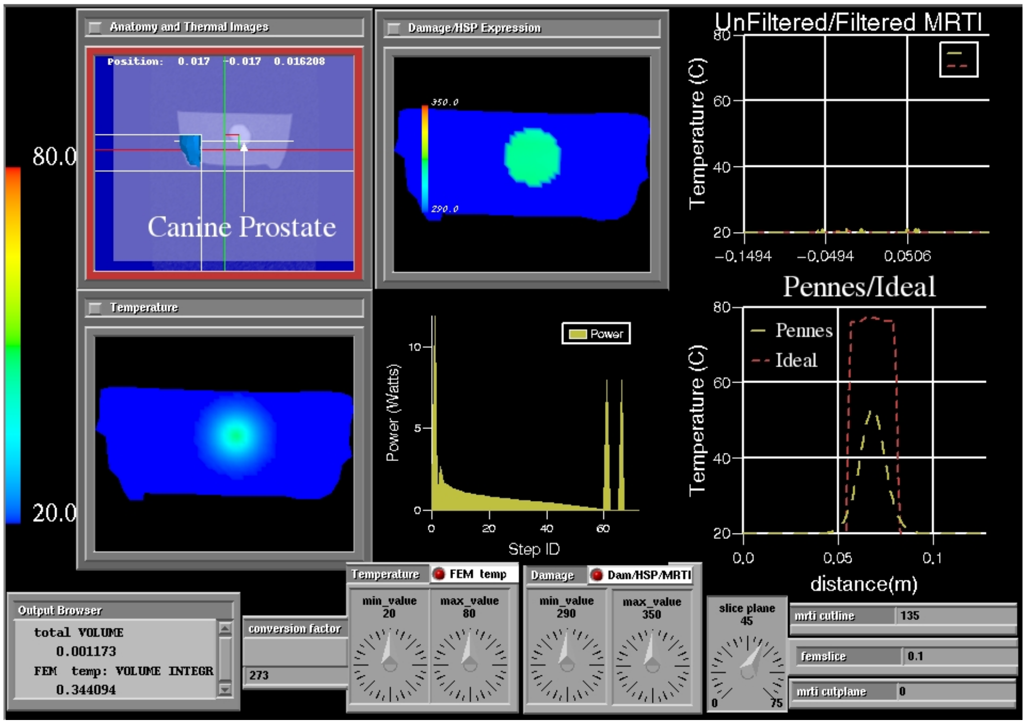

```
total VOLUME
   0.001173
FEM  temp: VOLUME INTEGR
   0.344094
```

conversion factor 273

min_value 20

max_value 80

min_value 290

max_value 350

slice plane 45

mrti cutline 135

femslice 0.1

mrti cutplane 0

Figure 5.13: Temperature based optimal control. The power is modulated to produce a temperature of 350 K within a tumorous region while maintaining room temperature in the surrounding region.

As shown, the optimizer is seen capable of converging to a solution in under 10 function/gradient evaluations for most of the scenarios considered. However, there do exist a few special exceptions that must be avoided. A similar study for temperature based control is shown in Figures 5.13 and 5.14.

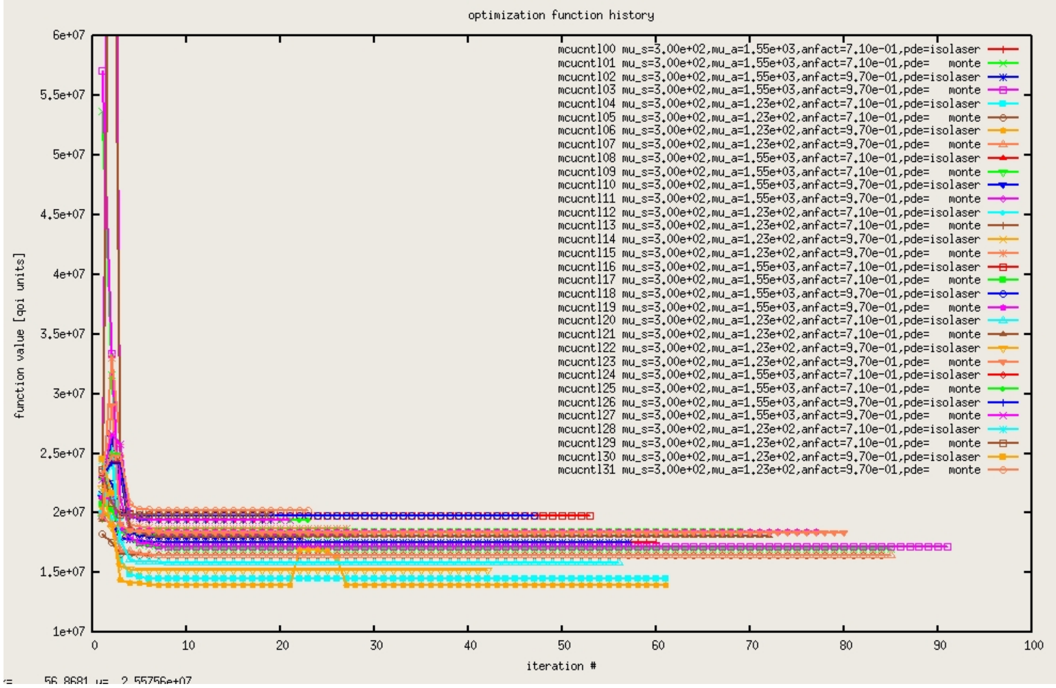

Figure 5.14: Optimization convergence plots for the temperature based optimal control problem. The number of entries in the legend of this graph illustrates the extent to which parameter space was explored. The legend contains the permutations of the high and low values of physically meaningful model parameters as well as different meshes were used. The graph demonstrates that with reasonable model coefficients the temperature-based optimal control problem can be solved in real-time in under ten function evaluations. The space-time norm of the the ideal temperature field is $\|u_{ideal}\| = 5.714 + 10$. Normalizing by this value, the error between the computed solution and the ideal temperature field is $\frac{\|u^h - u^h_{ideal}\|}{\|u^h_{ideal}\|} < 1\%$

The ability to modulate the power to produce a desired temperature field was studied over the range of physical model parameters. The optimizer is seen to be capable of converging to a solution for all scenarios considered in under 10 function/gradient evaluations. Using the space-time norm of the ideal field as a normalization factor of the error, reveals an error of $< 1\%$ for both the calibration and temperature based control. However, the difference in the contour plots for the MRTI images and the Pennes model prediction, shown in Figure 5.10, suggest that a better normalization may be needed. The sensitivity study was repeated for damaged based optimal control using the Arrhenius model, and results are given in Figure 5.15. As shown, the optimizer is unable to reliably converge to a solution in under 10 function evaluations.

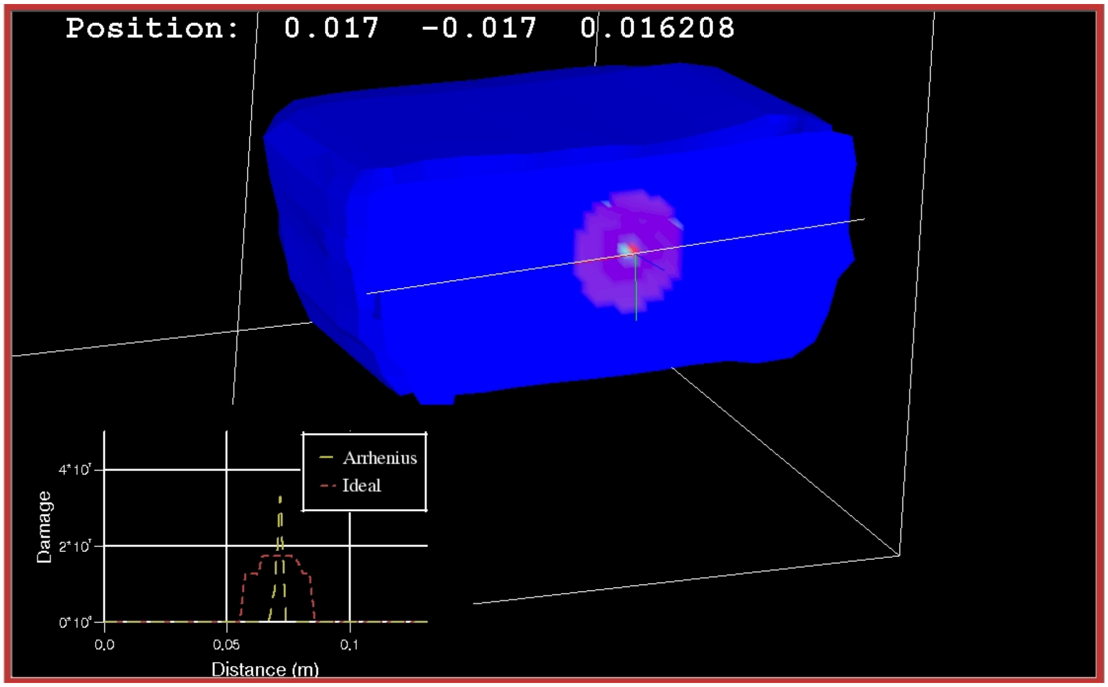

Figure 5.15: Damage based optimal control using Arrhenius damage model. The ideal damage field is compared to the computed damage field.

The large coefficients of the Arrhenius model is to blame, $A \approx 1.e17$. Changes from the initial guess in parameters space are proportional to the gradient.

The gradient is proportional to the large coefficients of the Arrhenius model. Furthermore, a small change in the temperature field produces a large change in the damage. These combined effects result in the drastic changes in the function evaluations seen in Figure 5.16 and the sensitivity in the function evaluation requires more evaluations to converge to a solution.

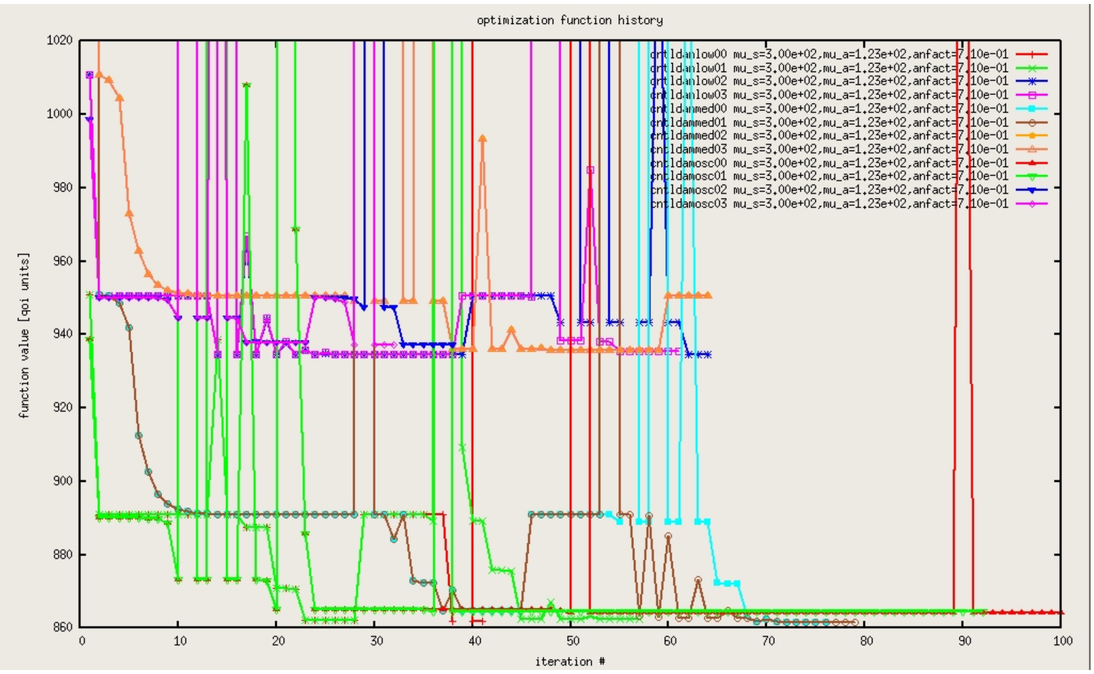

Figure 5.16: Optimization convergence plots for the damage based optimal control problem using an Arrhenius damage model. Permutations of the high and low values of physically meaningful model parameters as well as different meshes are used. The L_2 of the ideal damage field $\|u_{ideal}\| = 8.909563e + 02$. The large coefficients of the Arrhenius model cause small changes in the temperature field to produce large changes in the damage. This results in an unreliable real-time damage optimization.

5.3 *In-Vivo* Experiments

The control system, in its entirety, has been tested on *i*n-vivo canine prostate tissue. Pre-operative imaging data of a canine prostate and the neighboring anatomy was taken and used to create a FEM mesh Figure 5.17. The

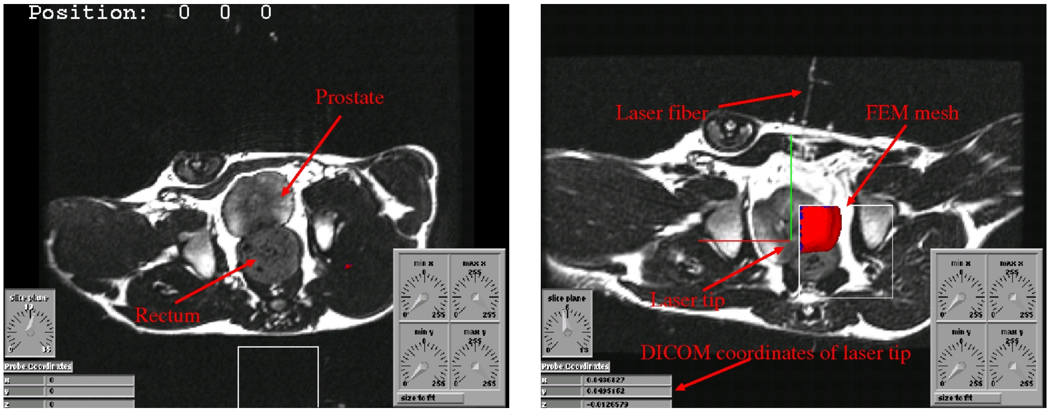

x 0
y 0
z 0

x 0.0436827
y 0.0495162
z -0.0126579

Figure 5.17: Pre-operative and intra-operative imaging data of canine prostate and the neighboring anatomy. The canine is laying on his back with legs upward. The pre-operative data was used to create a 3-D FEM mesh of the prostate consisting of 23,303 dof and 20,064 hexahedral elements. A cropped section of the FEM mesh is shown. The field of view shown in the imaging data is 240mm x 240mm. The resolution of the pre-operative and intra-operative data is 256x256x36 and 256x256x12, respectively. The relative difference in the location of the prostate is due to a bowel movement of the canine. The intra-operative image shown was used to locate the interstitial laser fiber within the DICOM coordinate system.

pre-operative imaging data was taken at a resolution of 256x256x36 voxels with a field of view of 240mm x 240mm and an out of plane spacing of 1.5mm. The FEM mesh consisted of 23,303 dof and 20,064 hexahedral elements. A pipeline of commercial software was used to generate the mesh. AMIRA, www.amiravis.com, was used to perform a semi-automatic segmentation of the prostate and create a low resolution tetrahedral mesh of the prostate. CUBIT,

cubit.sandia.gov, was used to convert the tetrahedral mesh into a hexahedral mesh and apply boundary conditions. Intra-operative imaging data is shown in Figure 5.17. The intra-operative imaging data was taken at a resolution of 256x256x12 voxels with a field of view of 240mm x 240mm and an out of plane spacing of 4mm. Comparison of the pre-operative image and the intra-operative image reveals that the prostate has moved a significant amount. The movement was uncontrollable, and due to a bowel movement that occurred sometime between the acquisition of the two data sets. The movement poses a significant registration problem. Current capabilities permit rigid registration only. The rigid registration is based on detecting the outer surface of the canine, not the prostate within. The rigid registration code found the out-of-plane position but failed in-plane due to the prostate movement. Consequently, under the given circumstances, the mesh was registered manually using AVS for interactive visualization. Furthermore, stringent time constraints on the experiment do not permit the use of the full resolution volume data sets for the rigid registration. The volume data sets must be subsampled to facilitate a reasonable execution time of the serial rigid registration code. However, for rigid registration, subsampling the imaging data by a factor of four in-plane does not loose much information on the outer boundary of the anatomy of the canine and significantly speeds up the registration from 25mins to 2mins with about 1mm difference in the final result. Another unexpected outcome of the registration process was that establishing connections between M.D. Anderson and TACC to send registration data was very time expensive. As a result, it is optimal to run the registration code locally at M.D. Anderson to minimize connections with TACC and only establish connections that are absolutely such as for the FEM computations.

The treatment day complications in the registration resulted in the use of the fail-safe structured mesh for the treatment day computations. The model calibration is dividing into a 180 second data acquisition phase followed by a 180 second computation phase. The canine prostate tissue was heated with a 3 Watt pulse for 90 seconds, 180 seconds worth of imaging is used

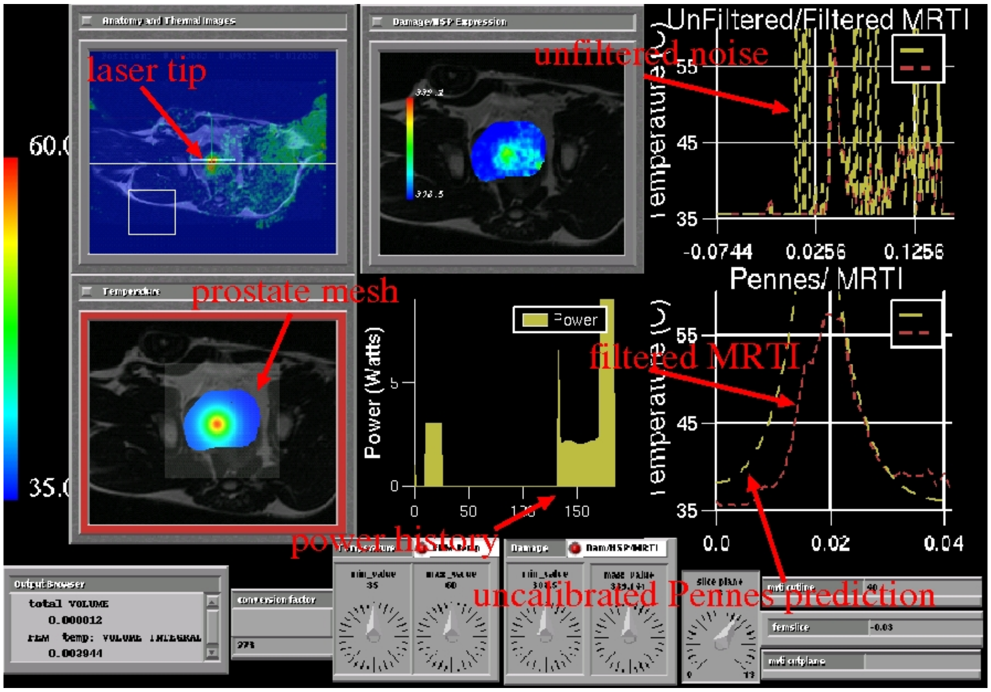

```
total VOLUME
  0.000012
FEM temp: VOLUME INTEGRAL
  0.003944
```

Figure 5.18: Depicted is the real-time visualization provided during the laser treatment. The anatomy, thermal images, FEM temperature prediction, and the power history are shown. Treatment day complications resulted in poor quality thermal imaging. Plenty of noise is seen in the thermal imaging but no discernible heating was detected during the calibration phase. The degree of noise prevalent is clearly seen in the cutlines of the thermal imaging. The power history shown was used in the treatment; it was computed for an uncalibrated model. A late time instance of the treatment is shown. The laser control of the uncalibrated model was manually overridden with the application of 9 Watts of power. The heating shown is due to the manual override.

to capture the cooling of the *i*n-vivo prostate tissue as well as the heating. The acquired imaging data is used for model calibration computations. Further treatment day complications resulted in poor quality thermal imaging data. The treatment imaging data shown in Figure 5.18 uses a space-time filter; in addition to the spatial median-deriche filtering pipeline, if the thermal data at a pixel changes by more than 11°C it is considered noise and filtered. The thermal data shows little heating as a result of the initial 3 Watt calibration pulse. Either, the amount of heating due to a 3 Watt pulse was within the noise range of the thermal imaging or the heating was quickly dissipated by blood perfusion. Consequently, the model calibration was unsuccessful as no discernible heating was detected in the thermal imaging data. The end result was the use of an uncalibrated model for the optimal control. The plan was to use the calibrated bioheat transfer model to create a 1.2cm lesion within the canine prostate. The optimal laser power as a function of time to heat the tissue region to 60°C for 300 seconds is computed. The power is controlled by the computers at TACC to create the lesion. However, as mentioned, the over filtering cascaded to the use of an uncalibrated model to control the heating of the tissue. The actual power history recorded by the visualase is shown in Figure 5.19. A time delay between the expected and actual power control is evident, as a result the initial 15 watt pulse of the optimal control did not occur. However, post-treatment computations show that the delay seen in power control of little consequence. The six second 15 Watts spike missing from the visualase log has an insignificant effect on the model predictions. Figure 5.19 also shows that copying the power control file directly to the mounted visualase directory interferes with visualase power log and instantaneously turns the laser off. The problem is a result of the file system architecture. Overwriting by copying the file instantaneously deletes the file which instantaneously

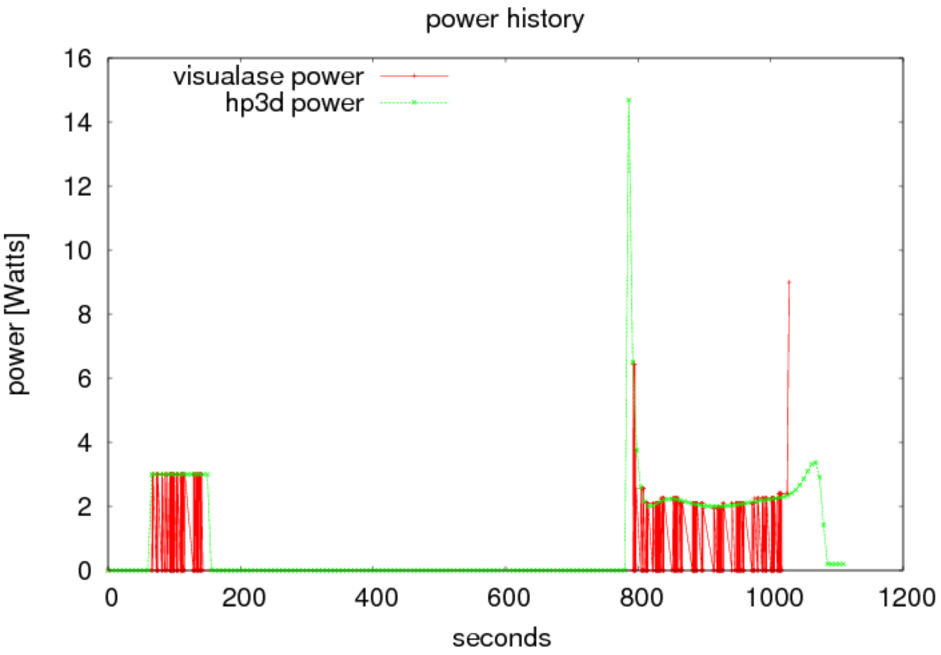

Figure 5.19: A comparison between the expected and actual power history as a function of time is shown. The power history was extracted from the log files of the visualase for comparison with the expected power profile from the FEM code. The graph shows ≈5 second time delay between the expected laser control and the actual laser control. The is evident by the visualase's log file failure to capture the 15 watt pulse at the beginning of the optimal control. The sharp rise in power at the end of the time history of the visualase log file is due to a manual override of the laser control due to the lack of heating seen.

turns the power off. The fix is trivial, overwriting the file by moving does not delete the file and simply changes the file pointers. The sharp rise in power to 9 watts at the end of the time history of the visualase log file, Figure 5.19, is due to a manual override of the laser control due to the lack of heating seen. The predicted heating of the uncalibrated model was greater than seen in reality. Consequently, the model predicted power history was significantly less than needed to achieve the desired treatment plan.

A second *in-vivo* trial of the control system was preformed on a canine. A late time treatment image of the control system applied to *in-vivo* laser treatment of canine prostate is shown in Figure 5.20; the entire duration of the treatment was 18 minutes. As shown, under Ideal Treatment, the goal was to demonstrate that the computational model could control the bioheat transfer and heat a region of 1.2cm in diameter to 60^{o}C. As illustrated in the power history, the treatment protocol is divided into four stages. During the

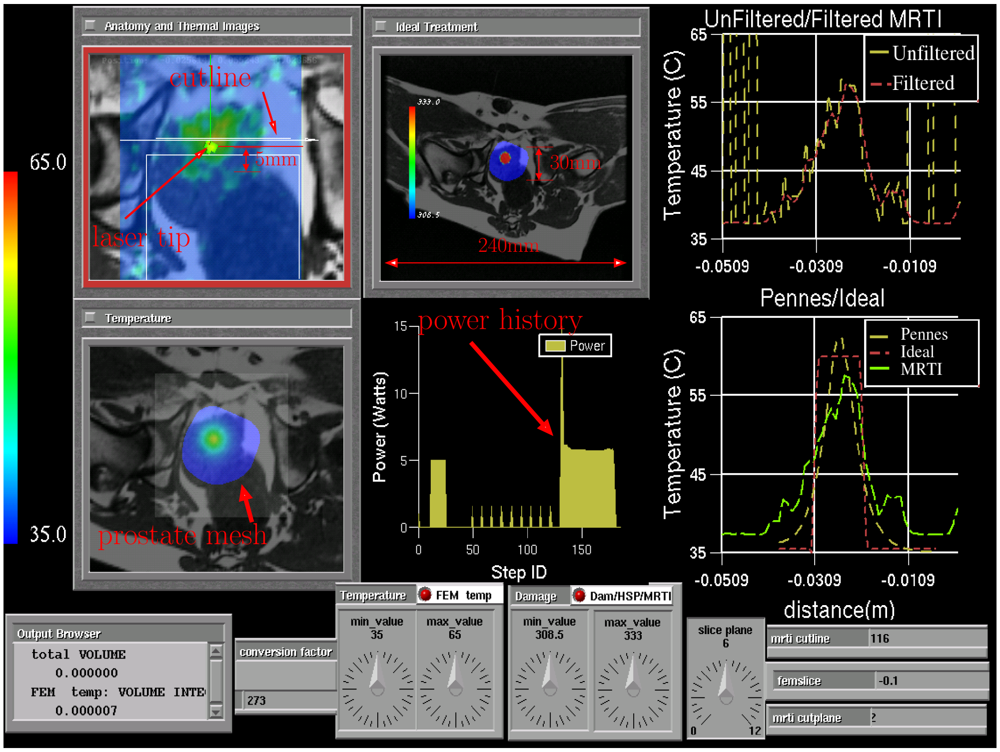

Output Browser

```
total VOLUME
   0.000000
FEM  temp: VOLUME INTE
   0.000007
```

conversion factor 273

min_value 35

max_value 65

min_value 308.5

max_value 333

slice plane 6

mrti cutline 116

femslice -0.1

mrti cutplane 2

Figure 5.20: Depicted is the real-time visualization provided during the laser treatment. The anatomy, thermal images, FEM temperature prediction, and the power history are shown. The field of view in the Ideal Treatment window is 240x240mm. Other windows zoom in to focus on the prostate. The degree of noise prevalent is clearly seen in the cutlines of the thermal imaging. The power history shown was used in the treatment.

first stage, the biological domain is pulse heated and MRTI thermal image data is acquired for the heating as well as the cooling. The second stage of the treatment accounts for the time span of the calculations that use the imaging data for model calibration. The third stage accounts for the time delay to compute the optimal temperature/ damage/ HSP heating protocol. The laser is prevented from entering a standby mode through a series of keep-alive pulses during the computational phase. In the fourth and final stage, the optimal laser control parameters are applied to the biological domain. In the event of the detection of an unexpectedly high temperature within the biological domain, a fail-safe shutoffs the laser power. For this particular trial, the

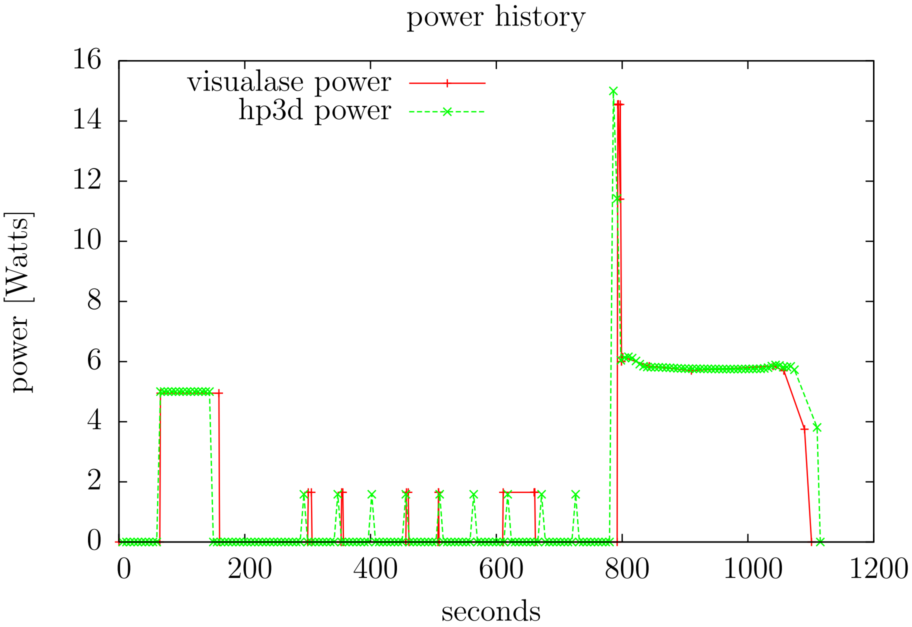

Figure 5.21: A comparison between the expected and actual power history as a function of time is shown. The power history was extracted from the log files of the visualase for comparison with the expected power profile from the FEM code.

perfusion, thermal conductivity, absorption coefficient, and laser position were calibrated. The initial position of the laser tip was taken as the tip of catheter seen in the planning images. However, results of the real-time calibration computations moved the laser tip 5mm from the initial guess. This suggests that the laser tip and the tip of the catheter that hold both the laser and the cooling fluid do not coincide, as expected. Cutlines illustrating the temperature as function of distance are taken through the thermal imaging data and finite element predictions for comparison. The location of the cutline is illustrated in the Anatomy and Thermal Images. The bottom right cutline shows good agreement between the desired treatment plan, the computation prediction, and the experimentally measured MRTI temperature field. Figure 5.21 compares the laser power history recorded on the visualase to the expected power control by hp3d. The actual and expected show very good agreement.

Chapter 6

Conclusions

This study demonstrates that a highly-efficient, parallelized, and robust computational models of bioheat transfer capable of dynamic interaction with imaging data generated during thermal therapies can be developed. Results show that parallel adaptive finite element technology employing modern data transfer infrastructure is capable of dynamic interaction with modern thermal imaging modalities to provide the real-time rigid registration and model calibration necessary to produce a computer controlled temperature field within a biological domain at very good accuracies. Furthermore, reliable finite element model simulations of laser therapies can be computed in a fraction of the time that the actual therapy takes place. This represents a significant milestone for this effort.

The orchestration of all the parameters and variables to successfully perform an *i*n-vivo trial of the control system is viewed as a major accomplishment. Multiple departments must be available to monitor the canine, operate the MRI scanner, and operate the laser. Years of work are embodied within a single 15 minute operation of the developed control system. Moreover, the visualization tools developed to understand and diagnose each new experiment are another contribution of this research. With respect to an FDA approved clinical tool, the current version of the control system is still in a beginning stage. The *in-vivo* results presented within this dissertation only scratch the surface of the full power of this method. Real-time treatment monitoring has been successfully embedded within an FEM framework and it has been shown to be possible to perform a patient specific model calibration and, furthermore, to use the calibrated model to optimally control the bioheat transfer. Throughout this research the nature of questions asked have changed from: Can one use a FEM model to control the bioheat transfer? to: What is the optimal treatment plan that can be imposed by the computational system? Still, optimal treatment plans based on HSP kinetics and cell damage functions will require further development on the commercial scale. However, the culmination of adaptive hp-finite element technology implemented on parallel computing architectures, modern data transfer and visualization infrastructure, thermal imaging modalities, and cellular damage mechanisms as a cancer treatment tool will provide a very powerful methodology for planning and optimizing the thermal therapy delivery for cancer treatments.

6.1 Future Work

This research may represent the beginning of the development of the cyber-infrastructure necessary to create an environment wherein experts in medicine, applied mathematics, computational science, imaging physics, and biomedical engineering can cross geographical and discipline barriers and collaborate to optimize cancer treatment planning for the benefit of the patient. Pursuit of the complex goals in this thesis have uncovered many topics for further research.

- The work focuses on using an isotropic laser source to provide the heating in a thermal therapy for treating prostate cancer. From a computational point of view, changing the thermal delivery modality merely amounts to changing the source term in the governing PDE. This technology has the potential to be extended to many areas of thermal treatment including RF, microwave, ultrasound, and even cryotherapy applicators. Modeling of the current laser source may also be improved by added the ability for real time Monte Carlo simulations to predict the laser fluence distribution.

- The desire to provide a nearly instantaneous solution to the inverse problems discussed provides motivation to develop algorithms capable of exploiting forthcoming peta-scale computers. Techniques may involve the use of a higher-order polynomial finite element method to increase the efficiency of the element matrix/vector computations, SMP architecture specific optimizations, and the development the algorithms necessary for fully automatic real-time adaptivity. High order polynomial finite element solutions would also provide a means to create a patient-specific geometric representation comparable with so called isogeometric analysis.

- The thesis has presented several objective functions used to mathematically represent a desired goal. It may be argued that different objective functions may be used to better represent the desired goal. For example, current damage functions account for only the damage accumulated during heating. Other objective functions may be designed to account for cooling as well as heating. Furthermore, different metrics may be explored to provide better accuracy of the the computed compared to the ideal solutions.

- The objective function evaluation and gradient computation have been the workhorse in this thesis. Adding the functionality for the Hessian computation may enhance the speed and efficiency of the optimization for more complex bioheat models involving larger parameter sets and could add the ability to provide uncertainty analysis for the calibrated model parameters.

Appendicies

Appendix A

Optimization (Lagrangian Approach)

The dissertation uses a pde constrained optimization framework based on the chain rule. An alternative Lagrangian approach is discussed in this appendix. The Lagrangian approach is equivalent under the following assumption.

$$\boxed{\begin{aligned} &\forall \beta \in \mathbb{P} \qquad \exists! u \in \mathcal{V} \text{ s.t.} \\ &B(u,\beta;v) = F(\beta;v) \qquad \forall v \in \mathcal{V} \end{aligned}}$$

The assumption guarantees that the following two problems are equivalent.

$$\boxed{\begin{aligned} &\text{Find } \beta^* \in \mathbb{P} \text{ s.t.} \\ &\qquad Q(u(\beta^*)) = \inf_{\beta \in \mathbb{P}} Q(u(\beta)) \end{aligned}} \iff \boxed{\begin{aligned} &\text{Find}(u^*,\beta^*) \in \mathcal{W} \equiv \mathcal{V} \times \mathbb{P} \text{ s.t.} \\ &\qquad Q(u^*) = \inf_{(u,\beta) \in \mathcal{W}} Q(u) \end{aligned}}$$

The Lagrangian is defined as

$$L((u,\beta);p) \equiv Q(u) + F(\beta;p) - B(u,\beta;p) = Q(u) - C(u,\beta;p)$$

A saddle point of the Lagrangian solves the optimal control problem. Linearity of the Lagrangian with respect to second argument is used in the proof.

Theorem A.0.1. *A saddle point of Lagrangian* $((u,\beta),p) \in \mathcal{W} \times \mathcal{V}$

$$L((u,\beta);q) \leq L((u,\beta);p) \leq L((v,\eta);p) \quad \forall ((v,\eta),q) \in \mathcal{W} \times \mathcal{V}$$

satisfies the optimal control problem

Proof. First we show that the saddle point is actually a minimum for the quantity of interest

$$L((u,\beta);q) \le L((v,\eta);p) \quad \forall((v,\eta),q) \in \mathcal{W} \times \mathcal{V}$$

$$\Rightarrow L((u,\beta);0) \le L((v,\eta);p) \quad \forall(v,\eta) \in \mathcal{W}$$

$$\Rightarrow Q(u) \le Q(v) + F(\eta;p) - B(v,\eta;p) \quad \forall(v,\eta) \in \mathcal{V}$$

$$\Rightarrow Q(u) \le Q(v) \quad \forall(v,\eta) \text{ such that } F(\eta;p) = B(v,\eta;p), \text{ i.e } (v,\eta) \in \mathcal{M}$$

It remains to show that the solution actually belongs to the space of constraints

$$L((u,\beta);q) \le L((u,\beta);p) \quad \forall q \in \mathcal{V}$$

$$\Rightarrow Q(u) + F(\beta;q) - B(u,\beta;q) \le Q(u) + F(\beta,p) - B(v,\beta;p) \quad \forall q \in \mathcal{V}$$

$$\Rightarrow F(\beta;q-p) - B(u,\beta;q-p) \le 0 \quad \forall q \in \mathcal{V}$$

$$\Rightarrow F(\beta;v) - B(u,\beta;v) \le 0 \quad \forall v \in \mathcal{V}$$

$$\Rightarrow F(\beta;v) \le B(u,\beta;v) \quad \forall v \in \mathcal{V}$$

$$\Rightarrow F(\beta;-v) \le B(u,\beta;-v) \quad \forall v \in \mathcal{V}$$

$$\Rightarrow F(\beta;v) \ge B(u,\beta;v) \quad \forall v \in \mathcal{V}$$

$$\Rightarrow F(\beta;v) = B(u,\beta;v) \quad \forall v \in \mathcal{V}$$

Therefore saddle points solve the optimal control problem. □

Furthermore, if there exist two distinct saddle points then each saddle point globally solves the problem and the value of the minimizers are the same.

Proof. suppose $\exists((u_1,\beta_1),p_1),((u_2,\beta_2),p_2)$:

$$L((u_1,\beta_1);q) \le L((u_1,\beta_1);p_1) \le L((v,\eta);p_1) \qquad \forall((v,\eta),q)$$

$$L((u_2,\beta_2);q) \le L((u_2,\beta_2);p_2) \le L((v,\eta);p_2) \qquad \forall((v,\eta),q)$$

this implies that

$$L((u_1,\beta_1);p_2) \le L((u_1,\beta_1);p_1) \le L((u_2,\beta_2);p_1)$$

$$L((u_2,\beta_2);p_1) \le L((u_2,\beta_2);p_2) \le L((u_1,\beta_1);p_2)$$

thus

$$L((u_1,\beta_1);p_1) \leq L((u_2,\beta_2);p_2) \qquad \& \qquad L((u_2,\beta_2);p_2) \leq L((u_1,\beta_1);p_1)$$

implies

$$L((u_1,\beta_1);p_1) = L((u_2,\beta_2);p_2) \qquad \neq \qquad ((u_1,\beta_1);p_1) = ((u_2,\beta_2);p_2)$$

The definition of the Lagrangian and the saddle points imply that

$$Q(u_1) = Q(u_2) \leq Q(v) \qquad \forall v$$

□

Necessary conditions are that a solution is a saddle point of the Lagrangian. The following characterization of the saddle points is useful for finding an optimal solution.

<u>Theorem</u>. A saddle point of the Lagrangian satisfies.

$$\begin{aligned} \lim_{\theta\to 0} \frac{1}{\theta}\left[L((u+\theta\hat{u},\beta);p) - L((u,\beta);p)\right] &= 0 \\ \lim_{\theta\to 0} \frac{1}{\theta}\left[L((u,\beta+\theta\hat{\beta});p) - L((u,\beta);p)\right] &= 0 \\ \lim_{\theta\to 0} \frac{1}{\theta}\left[L((u,\beta);p+\theta q) - L((u,\beta);p)\right] &= 0 \end{aligned} \tag{A.1}$$

Proof. For $\epsilon > 0$,

$$L((u\pm\epsilon\hat{u},\beta);p) - L((u,\beta);p) \geq 0 \qquad \forall \hat{u}$$

$$\Rightarrow \begin{cases} \dfrac{L((u\pm\epsilon\hat{u},\beta);p) - L((u,\beta);p)}{\epsilon} \geq 0 \\ \dfrac{L((u\pm\epsilon\hat{u},\beta);p) - L((u,\beta);p)}{-\epsilon} \leq 0 \end{cases}$$

This leads to the following four cases

$$\begin{aligned}
\lim_{\epsilon\to 0}\frac{L((u+\epsilon\hat{u},\beta);p)-L((u,\beta);p)}{\epsilon} &\geq 0\\
-\lim_{\epsilon\to 0}\frac{L((u+(-\epsilon)\hat{u},\beta);p)-L((u,\beta);p)}{(-\epsilon)} &\geq 0\\
\lim_{\epsilon\to 0}\frac{L((u+(-\epsilon)\hat{u},\beta);p)-L((u,\beta);p)}{(-\epsilon)} &\leq 0\\
-\lim_{\epsilon\to 0}\frac{L((u+\epsilon\hat{u},\beta);p)-L((u,\beta);p)}{\epsilon} &\leq 0
\end{aligned}$$

which implies that

$$\pm\lim_{\theta\to 0}\frac{1}{\theta}\left[L((u\pm\theta\hat{u},\beta);p)-L((u,\beta);p)\right]\geq 0$$

where θ approaches zero from the positive or negative direction. Similar arguments hold for the remaining cases. $\square$

The characterization of the saddle point may be used to recover the same equations as from the chain rule formulation.

$$\boxed{\begin{array}{l}
\text{Find } (u,\beta,p) \text{ s.t.}\\
\delta_u C(u,\beta;\hat{u},p) = \delta_u Q(u,\beta;\hat{u}) \qquad \forall\hat{u}\in\mathcal{V}\\
\delta_\beta C(u,\beta;\hat{\beta},p) = \delta_\beta Q(u,\beta;\hat{\beta}) \qquad \forall\hat{\beta}\in\mathbb{P}\\
\qquad C(u,\beta;v) = 0 \qquad \forall v\in\mathcal{V}
\end{array}}$$

Appendix B

Analysis of the Pennes Model

In this appendix, the method of lines is applied to Pennes equation. Solutions using the method of lines are understood as the mapping from the time interval of interest, $(0, T]$, to the discretized space of finite element function S_h, (4.7). The method of lines serve as an intermediate step between the continuous Pennes model and the fully discretize Pennes model, temporal discretization as well as spatial. Conditions sufficient for establishing the existence of a Galerkin solution to Pennes model under the framework of the method of lines are given. Further, *a priori* error estimates for the Galerkin method of lines solution are provided under the strong assumptions that a solution exists and is sufficiently smooth. The error estimates follow the work of Thomee [41].

B.1 Framework and assumptions

Consider Pennes equation of the form

$$\frac{\partial u}{\partial t} - \nabla \cdot \left(\frac{k(u)}{\rho c_p} \nabla u \right) = \frac{\omega(u)}{\rho c_p} c_{blood}(u_a - u) + \frac{1}{\rho c_p} Q_{laser}(\mathbf{x}, t)$$

subject to the Cauchy boundary conditions and initial conditions

$$k(u)\nabla u \cdot \mathbf{n} = h(u - u_\infty) \qquad \text{on } \partial\Omega$$

$$u(\mathbf{x}, 0) = u^0 \qquad \text{in } \Omega$$

Define

$$a(u) \equiv \frac{k(u)}{\rho c_p}$$

$$f(u,\mathbf{x}) \equiv \frac{\omega(u)}{\rho c_p} c_{blood}(u_a - u) + \frac{1}{\rho c_p} Q_{laser}(\mathbf{x},t)$$

The analysis assumes that $k(u)$ and $\omega(u)$ are smooth and bounded of the form $C_0 + C_1\ atan(C_2\ (u - C_3)$, (B.1)

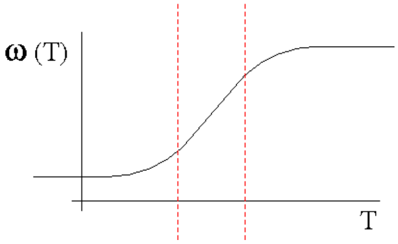

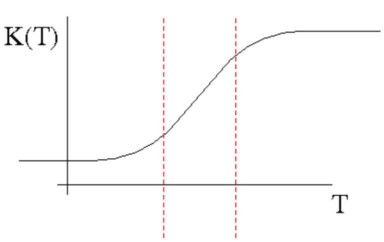

The problem may now be stated as follows.

Given a Lipshitz domain Ω with smooth boundary $\partial\Omega$ find the scalar temperature field $u : [0,T] \rightarrow H^1(\Omega)$ with $u_t : [0,T] \rightarrow L_2(\Omega)$ such that

$$\begin{aligned}(u_t, v) + (a(u)\nabla u, \nabla v) =&(f(u,\mathbf{x}), v)\\ &+ (\tilde{h}(u - u_\infty), v)_{L_2(\partial\Omega)} \qquad \forall v \in H^1(\Omega)\end{aligned} \tag{B.1}$$

$$u(\cdot,0) = u^0 \qquad \text{a.e. in } \Omega \tag{B.2}$$

where $\tilde{h} \equiv \frac{h}{\rho c_p}$ and a satisfies

$$0 < \mu \leq a(u) \leq M \qquad \forall u \in \mathbb{R}$$

The following proposition is used to develop existence of a Galerkin method solution as well as for the a priori error estimates.

Proposition B.1.1. *Coefficients a and f are Lipschitz*

$$\boxed{\begin{aligned} |a(u) - a(v)| &\leq C|u - v| \\ |f(u, \boldsymbol{x}) - f(v, \boldsymbol{x})| &\leq C|u - v| \end{aligned}}$$

Proof: by definition of the coefficients

$$|a(u) - a(v)| = \left| \frac{k(u)}{\rho c_p} - \frac{k(v)}{\rho c_p} \right|$$

by mean value theorem

$$\begin{aligned} &\leq \frac{k'(u^*)}{\rho c_p}|u - v| \qquad \text{where } u^* \in [u, v] \\ &\leq C|u - v| \qquad \text{because } k' \text{ is bounded} \end{aligned}$$

Applying the definition to the source term we have

$$\begin{aligned} |f(u, \mathbf{x}) - f(v, \mathbf{x})| &= \left| \frac{\omega(u)}{\rho c_p}(u_a - u) + Q_{laser}(\mathbf{x}) - \frac{\omega(v)}{\rho c_p}(u_a - v) - Q_{laser}(\mathbf{x}) \right| \\ &\leq \frac{1}{\rho c_p}|\omega(u)u - \omega(v)v| + \frac{|\omega(u) - \omega(v)|}{\rho c_p}u_a \\ &\leq |\frac{C}{\rho c_p}||u - v| \qquad \text{(By mean value theorem)} \end{aligned}$$

where the following bound was used

$$|(\omega(u)u)'| = |\omega'(u)u + \omega(u)| \leq \frac{u}{1 + u^2} + \omega_{max} \leq C$$

□

B.2 Method of Lines

Under the method of lines, the solution is represented as a mapping from the time interval of interest to the finite element space of functions.

$$u_h : (0, T] \to S_h \qquad u_h(\mathbf{x}, t) = \sum_{j=1}^{N_h} \alpha_j(t)\ \varphi_j(\mathbf{x})$$

where the α_j's are continuous in time and the finite element space is defined in (4.7). This section establishes existence of a solution under the method of lines. The problem statement is as follows.

Find the scalar temperature field $u_h : [0,T] \rightarrow S_h(\Omega)$:

$$\begin{aligned}(u_{h,t}, v) + (a(u_h)\nabla u_h, \nabla v) =& (f(u_h, \mathbf{x}), v) \\ &+ (\tilde{h}(u_h - u_\infty), v)_{L_2(\partial\Omega)} \qquad \forall v \in S_h(\Omega)\end{aligned} \tag{B.3}$$

$$u_h(\cdot, 0) = u_h^0 \qquad \text{a.e. in } \Omega_h \tag{B.4}$$

Theorem B.2.1. *There exist a unique Galerkin solution to the method of lines applied to the modified Pennes equation with Lipschitz data for all t.*

Proof: The proof follows from Banach's contraction mapping theorem. Substituting the discrete form of the temperature field into the Galerkin formulation and using Einstein's summation convention gives

$$\begin{aligned}(\alpha'_j(t)\;\varphi_j(\mathbf{x}), \varphi_{,}) + (a(\alpha_j(t)\;\varphi_j(\mathbf{x}))\alpha_j(t)\;\varphi_{j,l}(\mathbf{x})\varphi_{k,l}(\mathbf{x})) &= (f(\alpha_j(t)\;\varphi_j(\mathbf{x}), \mathbf{x}), \varphi_{,}) \\ &+ (\tilde{h}(\alpha_j(t)\;\varphi_j(\mathbf{x}) - u_\infty), \varphi_k)_{L_2(\partial\Omega)} \qquad \forall k = 1, ..., N_h\end{aligned}$$

The discrete approximation may also be viewed in the form

$$A\alpha'(t) = F(\alpha(t))$$

where

$$F(\alpha) = (f(\alpha_j\;\varphi_j, \mathbf{x}), \varphi_k) - (a(\alpha_j\;\varphi_j)\alpha_j\;\varphi_{j,l}, \varphi_{k,l}) + (\tilde{h}(\alpha_j\;\varphi_j - u_\infty), \varphi_k)_{L_2(\partial\Omega)}$$

The corresponding integral equation is

$$\alpha(t) = \alpha_0 + A^{-1}\int_0^t F(\alpha(s))\;ds$$

Viewed as an operator, the mass matrix $A : \mathbb{R}^{N_h} \to \mathbb{R}^{N_h} to$ is positive definite implying that its null space is the zero vector, $\mathcal{N}(A) = 0$. Consequently, by rank and nullity, A is bijective and we have the right to speak of its inverse, A^{-1}.

A solution will be sought in the space of functions with a bounded change from the given initial condition.

$$R \equiv \left\{ \mathbf{x}(t) \in \mathbb{R}^{N_h} : \max_t ||\mathbf{x}(t) - \alpha_0|| \leq a, t \leq T \right\}$$

It will be shown that the mapping

$$\mathbf{B}(\mathbf{x}(t)) = \alpha_0 + A^{-1} \int_0^t F(\mathbf{x}(s))\, ds$$

is a contraction mapping on R. First, B must be shown to be mapping from R to R. The image of a function from R is bounded.

$$||\mathbf{B}(\mathbf{x}(t)) - \alpha_0|| \leq ||A^{-1}|| \int_0^t ||F(\mathbf{x}(s))||\, ds$$

where $||A^{-1}||$ is a matrix norm. Since F is a continuous function on R, the Weierstrass theorem implies that F attains a maximum value. Let

$$\max_s ||F(\mathbf{x}(s))||_1 < K$$

then

$$||\mathbf{B}(\mathbf{x}(t)) - \alpha_0|| \leq ||A^{-1}||\; K\; T \equiv a$$

where $||A^{-1}||\; K\; T = a$, thus $\mathbf{B} : R \to R$.

The Lipschitz property of the source term is used to show that the mapping **B** is a contraction mapping.

$$||F(\alpha_1(s)) - F(\alpha_2(s))||_1 = \sum_k \left| \begin{array}{l} (f(\alpha_j^1\, \varphi_j, \mathbf{x}), \varphi_k) - (a(\alpha_j^1\, \varphi_j)\alpha_j^1\, \varphi_{j,l}, \varphi_{k,l}) \\ \quad + (\tilde{h}(\alpha_j^1\, \varphi_j - u_\infty), \varphi_k)_{L_2(\partial\Omega)} \\ \quad - (f(\alpha_j^2\, \varphi_j, \mathbf{x}), \varphi_k) \\ \quad + (a(\alpha_j^2\, \varphi_j)\alpha_j^2\, \varphi_{j,l}, \varphi_{k,l}) \\ \quad - (\tilde{h}(\alpha_j^2\, \varphi_j - u_\infty), \varphi_k)_{L_2(\partial\Omega)} \end{array} \right|$$

using linearity of the inner product

$$||F(\alpha_1(s)) - F(\alpha_2(s))||_1 = \sum_k \left| \begin{array}{l} (f(\alpha_j^1\, \varphi_j, \mathbf{x}) - f(\alpha_j^2\, \varphi_j, \mathbf{x}), \varphi_k) \\ \quad - (a(\alpha_j^1\, \varphi_j)\alpha_j^1\, \varphi_{j,l} - a(\alpha_j^2\, \varphi_j)\alpha_j^2\, \varphi_{j,l}, \varphi_{k,l}) \\ \quad - (\tilde{h}(\alpha_j^1\, \varphi_j - \alpha_j^2\, \varphi_j), \varphi_k)_{L_2(\partial\Omega)}| \end{array} \right| \tag{B.5}$$

We now look at each term of (B.5) individually and use proposition B.1.1. For the source term we have

$$\begin{aligned} \sum_k |(f(\alpha_j^1\, \varphi_j, \mathbf{x}) - f(\alpha_j^2\, \varphi_j, \mathbf{x}), \varphi_k)| &\leq \int_\Omega \sum_k C|\alpha_j^1\, \varphi_j - \alpha_j^2\, \varphi_j||\varphi_k| \\ &\leq C\int_\Omega \sum_k C|\alpha_j^1 - \alpha_j^2||\varphi_j||\varphi_k| \\ &\leq C\sum_j |\alpha_j^1 - \alpha_j^2| \int_\Omega |\varphi_j| \sum_k |\varphi_k| \\ &\leq \tilde{C}\sum_j |\alpha_j^1 - \alpha_j^2| \end{aligned}$$

For the diffusive term

$$\begin{aligned} &\sum_k |(a(\alpha_j^1\, \varphi_j)\alpha_j^1\, \varphi_{j,l} - a(\alpha_j^2\, \varphi_j)\alpha_j^2\, \varphi_{j,l}, \varphi_{k,l})| \\ &\qquad = \sum_k |\int_\Omega (a(u^1)u^1 - a(u^2)u^2)\varphi_{k,l}\, dx| \end{aligned}$$

by mean value theorem

$$
\begin{aligned}
&= \sum_k \Big| \int_\Omega \left[(a(u^2) + a'(u^*)(u^1 - u^2))u^1 - a(u^2)u^2\right] \varphi_{k,l} \, dx \Big| \\
&= \sum_k \Big| \int_\Omega \left[a(u^2)(u^1 - u^2) + u^1 a'(u^*)(u^1 - u^2)\right] \varphi_{k,l} \, dx \Big|
\end{aligned}
$$

using that a, a', and u^1 are bounded

$$
\begin{aligned}
&\leq \sum_k C \int_\Omega |u^1 - u^2||\varphi_{k,l}| \, dx| \\
&\leq \sum_k C \int_\Omega |\alpha_j^2 - \alpha_j^1||\varphi_j||\varphi_{k,l}| \, dx| \\
&\leq \tilde{C} \sum_j |\alpha_j^1 - \alpha_j^2|
\end{aligned}
$$

Finally, for the boundary term

$$
\sum_k |(\tilde{h}(\alpha_j^1 \, \varphi_j - \alpha_j^2 \, \varphi_j, \varphi_k)_{L_2(\partial\Omega)}| = \qquad \sum_k \Big| \int_{\partial\Omega} \tilde{h}\gamma[(\alpha_j^1 - \alpha_j^2)\varphi_j]\gamma\varphi_k \, dA \Big|
$$

by linearity of trace operator

$$
\begin{aligned}
&\leq \quad \tilde{h} \sum_j |\alpha_j^1 - \alpha_j^2| \sum_k \Big| \int_{\partial\Omega} \gamma\varphi_j\gamma\varphi_k \, dA \Big| \\
&\leq \quad \tilde{h} \sum_j |\alpha_j^1 - \alpha_j^2| \sum_k ||\varphi_j||_{H^1} ||\varphi_k||_{H^1} \\
&\leq \quad C \sum_j |\alpha_j^1 - \alpha_j^2|
\end{aligned}
$$

The final result being

$$
||F(\alpha_1(s)) - F(\alpha_2(s))||_1 \leq \quad \tilde{C}||\alpha_1(s) - \alpha_2(s)||_1
$$

therefore

$$\begin{aligned}\max_t ||\mathbf{B}(\alpha_1(t)) - \mathbf{B}(\alpha_2(t))||_1 &\leq \max_t ||A^{-1} \int_0^t F(\alpha_1(s)) - F(\alpha_2(s))\, ds|| \\ &\leq ||A^{-1}|| \max_t \int_0^t ||F(\alpha_1(s)) - F(\alpha_2(s))||_1\, ds \\ &\leq ||A^{-1}||\tilde{C}u \max_t ||\alpha_1(t) - \alpha_2(t)||_1\end{aligned}$$

□

Notice that the above proof shows that for a given initial condition and with small enough time steps, there should be no problem with a computer simulation of the Pennes Bioheat transfer equation with Cauchy boundary conditions.

B.3 Error Estimates

A-priori error estimates are provided for the method of lines solution developed in the previous section under the assumptions that the corresponding continuous problem admits a unique solution that is sufficiently smooth. In obtaining the estimates, the spaces of trial and test functions will have to be restricted to functions that vanish on the boundary of the domain, $S_h^0 \subset H_0^1(\Omega)$. The restriction provides necessary Poincare inequalities and makes dealing with the boundary terms tractable. As a result, the problem formulation is over slightly different function spaces.

Given a finite element mesh Ω_h find the scalar temperature field $u_h : [0,T] \rightarrow S_h^0(\Omega) \subset H_0^1(\Omega)$ such that

$$(u_{h,t}, v) + (a(u_h)\nabla u_h, \nabla v) = (f(u_h, \mathbf{x}), v) \qquad \forall v \in S_h^0(\Omega) \qquad \text{(B.6)}$$

$$u_h(\cdot, 0) = u^0 \qquad \text{a.e. in } \Omega_h \qquad \text{(B.7)}$$

The error estimates are derived for the following problem. Unless explicitly stated, all norms are taken to be the $L_2(\Omega)$ norm. The interpolation estimate given in (4.8) are used in this section.

The following lemma for the elliptic projection of the solution is a critical step in obtaining the a-priori estimates.

Lemma B.3.1. *let $\tilde{u}_h \in S_h^0(\Omega)$ be defined as the elliptic projection of the solution, u, i.e.*

$$(a(u)\nabla(\tilde{u}_h - u), \nabla\chi) = 0 \qquad \forall\chi \in S_h^0$$

then

$$\begin{aligned} ||\nabla(\tilde{u}_h - u)|| &\leq C\frac{h}{p}||u||_{H^2(\Omega)} \\ ||\tilde{u}_h - u)|| &\leq C\left(\frac{h}{p}\right)^2 ||u||_{H^2(\Omega)} \end{aligned}$$

Proof. given $\chi \in S_h^0$

$$\begin{aligned} \mu||\nabla(\tilde{u}_h - u)||^2 &= \mu(\nabla(\tilde{u}_h - u), \nabla(\tilde{u}_h - u)) \\ &\leq (a(u)\nabla(\tilde{u}_h - u), \nabla(\tilde{u}_h - u)) \end{aligned}$$

by property of elliptic projector because $\tilde{u}_h \in S_h^0(\Omega)$

$$\begin{aligned} &= -(a(u)\nabla(\tilde{u}_h - u), \nabla u) \\ &= (a(u)\nabla(\tilde{u}_h - u), \nabla(\chi - u)) \qquad \forall\chi \in S_h^0(\Omega) \\ &\leq M||\nabla(\tilde{u}_h - u)||\,||\nabla(\chi - u)|| \qquad \forall\chi \in S_h^0(\Omega) \end{aligned}$$

which implies that

$$||\nabla(\tilde{u}_h - u)|| \leq \frac{M}{\mu}||\nabla(\chi - u)|| \qquad \forall\chi$$

let $\chi = \Pi^{hp} u$

$$\begin{aligned} ||\nabla(\tilde{u}_h - u)|| &\leq \frac{M}{\mu} ||\nabla(\Pi^{hp} u - u)|| \\ &\leq \frac{M}{\mu} \tilde{C} ||\nabla(\Pi^{hp} u - u)||_{H^1(\Omega)} \\ &\leq \frac{M}{\mu} C \frac{h}{p} ||u||_{H^2(\Omega)} \end{aligned}$$

for the lower order estimate, an additional bound on the solution u is needed.

$$||u||_{H^2} \leq C||\varphi||$$

where

$$\varphi \equiv -\nabla \cdot (a(u)\nabla u) = -a(u)\triangle u - \nabla a(u) \cdot \nabla u$$

this follows from

$$\begin{aligned} \mu||\nabla u||^2 &\leq |(a(u)\nabla u, \nabla u)| \\ &= |(\varphi, u)| \\ &\leq ||\varphi|| \; ||u|| \\ &\leq ||\varphi|| \; ||u||_{H^2(\Omega)} \end{aligned}$$

we need a Poincare inequality here

$$\leq ||\varphi|| \; ||\nabla u||$$

therefore

$$||\nabla u|| \leq C||\varphi||$$

using a Poincare inequality again

$$\begin{aligned}||u||_{H^2(\Omega)} &\leq C||\triangle u||\\ &\leq C||a(u)\triangle u||\\ &= C||\varphi + \nabla a(u)\cdot\nabla u||\\ &= C||\varphi|| + ||\nabla a(u)||\ ||\nabla u||\end{aligned}$$

using the previous inequality and that ∇a is bounded because of the regularity assumptions on the solution

$$||u||_{H^2(\Omega)} \leq C||\varphi||$$

finally we have

$$\begin{aligned}(\tilde{u}_h - u, \varphi) &= (a(u)\nabla(\tilde{u}_h - u), \nabla u)\\ &= (a(u)\nabla(\tilde{u}_h - u), \nabla(u-\chi))\\ &\leq C||\nabla(\tilde{u}_h - u)||\ ||\nabla(u-\chi)||\end{aligned}$$

using the previous result, and interpolation inequality again

$$\leq C\left(\frac{h}{p}||u||_{H^2(\Omega)}\right)\left(\frac{h}{p}||u||_{H^2(\Omega)}\right)$$

which implies

$$\frac{|(\tilde{u}_h - u, \varphi)|}{||\varphi||} \leq C\left(\frac{h}{p}\right)^2 ||u||_{H^2(\Omega)}$$

using duality and definition of least upper bound

$$||\tilde{u}_h - u|| = \sup_{f\in L_2}\frac{|(\tilde{u} - u, f)|}{||f||} \leq C\left(\frac{h}{p}\right)^2 ||u||_{H^2(\Omega)}$$

□

Remark B.3.1. Notice in the proof that the regularity requirements on the solution is $C_0^1(\Omega)$ and that the restriction that the functions vanish on the boundary is used heavily, otherwise the boundary terms would be intractable.

Defining the error in the elliptic projection as $\rho = \tilde{u}_h - u$ we have

$$||\rho|| + \left(\frac{h}{p}\right)||\nabla\rho|| \leq C(u)\left(\frac{h}{p}\right)^2 \tag{B.8}$$

The following bound on the time derivative of the error in the elliptic projection is also needed.

Lemma B.3.2.

$$||\rho_t|| + \left(\frac{h}{p}\right)||\nabla\rho_t|| \leq C(u)\left(\frac{h}{p}\right)^2$$

Proof.

$$\begin{aligned}
\mu||\nabla\rho_t||^2 &\leq |(a(u)\nabla\rho_t, \nabla\rho_t)| \\
&= |(a(u)\nabla\rho_t, \nabla(\rho_t + \chi - \chi))| \\
&= |(a(u)\nabla\rho_t, \nabla(\tilde{u}_{h,t} - \chi)) + (a(u)\nabla\rho_t, \nabla(\chi - u_t))|
\end{aligned}$$

using that $\tilde{u}_{h,t} - \chi \in S_h^0(\Omega)$

and $(a(u)\nabla\rho_t, \nabla\chi) = -(a_t(u)\nabla\rho, \nabla\chi) \qquad \forall\chi \in S_h^0(\Omega)$

$$\begin{aligned}
&\leq |(a(u)\nabla\rho_t, \nabla(\chi - u_t)) + (a_t(u)\nabla\rho, \nabla(\chi - \tilde{u}_{h,t}))| \\
&\leq C\left(||\nabla\rho_t||\,||\nabla(\chi - u_t)|| + ||\nabla\rho||\,||\nabla(\chi - \tilde{u}_{h,t})||\right) \\
&\leq C||\nabla\rho_t||\ \left(\frac{h}{p}\right)||u_t||_{H^2(\Omega)} \\
&\qquad + ||\nabla\rho||\,||\nabla(\chi - u_t + u_t - \tilde{u}_{h,t})|| \\
&\leq C||\nabla\rho_t||\ \left(\frac{h}{p}\right)||u_t||_{H^2(\Omega)} \\
&\qquad + ||\nabla\rho||\ \left(\left(\frac{h}{p}\right)||u_t||_{H^2(\Omega)} + ||\nabla\rho_t||\right)
\end{aligned}$$

using Young's inequality

$$\leq C\left(\epsilon_1||\nabla\rho_t||^2 + \frac{\left(\frac{h}{p}\right)^2||u_t||^2_{H^2(\Omega)}}{4\epsilon_1}\right)$$

$$+ C\left(\epsilon_2||\nabla\rho||^2 + \frac{\left(\frac{h}{p}\right)^2||u_t||^2_{H^2(\Omega)}}{4\epsilon_2}\right)$$

$$+ C\left(\epsilon_3||\nabla\rho_t||^2 + \frac{||\nabla\rho||^2}{4\epsilon_3}\right)$$

with $\epsilon_1 = \frac{\mu}{4C}$, $\epsilon_2 = 1$, and $\epsilon_3 = \frac{\mu}{4}$

$$\mu||\nabla\rho_t||^2 \leq \frac{\mu}{2}||\nabla\rho_t||^2 + C\left(||\nabla\rho||^2 + \left(\frac{h}{p}\right)^2||u_t||^2_{H^2(\Omega)}\right)$$

Therefore we have that

$$||\nabla\rho_t|| \leq C(u)\left(\frac{h}{p}\right)$$

for the lower order estimate

$$\begin{aligned}
(\rho_t, \varphi) &= (a(u)\nabla\rho_t, \nabla u) \\
&= (a(u)\nabla\rho_t, \nabla u) - (a(u)\nabla\rho_t, \nabla\chi) - (a_t(u)\nabla\rho, \nabla\chi) \\
&\qquad + (\nabla\rho, a_t(u)\nabla u) - (\nabla\rho, a_t(u)\nabla u) \\
&= (a(u)\nabla\rho_t, \nabla(u-\chi)) + (a_t(u)\nabla\rho, \nabla(u-\chi)) - (\nabla\rho, a_t(u)\nabla u)
\end{aligned}$$

again let $\chi = \Pi^{hp}u$ and using integration by parts

$$\begin{aligned}
|(\rho_t, \varphi)| &\leq C||\nabla\rho_t||\left(\frac{h}{p}\right)||u||_{H^2} \\
&\qquad + C||\nabla\rho||\left(\frac{h}{p}\right)||u||_{H^2} \\
&\qquad + C||\rho||\,||u||_{H^2}
\end{aligned}$$

using previous results and last lemma

$$|(\rho_t, \varphi)| \leq C(u) \left(\frac{h}{p}\right)^2 ||\varphi||$$

and by duality

$$||\rho_t|| \leq C(u) \left(\frac{h}{p}\right)^2$$

$\square$

The following bound on the norm of the gradient of the elliptic projection of the solution will also be needed

Lemma B.3.3.

$$||\nabla \tilde{u}_h||_{L_\infty} \leq C(u)$$

Proof.

$$||\nabla \tilde{u}_h||_{L_\infty} \leq ||\nabla(\tilde{u}_h - I_h u)||_{L_\infty} + ||\nabla I_h u||_{L_\infty}$$

where I_h is the nodal interpolant. Looking at each term separately,

$$\begin{aligned} ||\nabla(\tilde{u}_h - I_h u)||_{L_\infty} &\leq ||\nabla(\tilde{u}_h - I_h u)||_{W_{1,\infty}} \\ &\leq Ch^{-1}||\nabla(\tilde{u}_h - I_h u)|| \qquad \text{Inverse inequality (see [19] pg 76)} \\ &\leq Ch^{-1}\left(||\nabla\rho|| + ||\nabla(I_h u - u)||\right) \\ &\leq C(u) \qquad \text{Lemma B.3.1 p=1} \end{aligned}$$

and

$$||\nabla I_h u||_{L_\infty} = ||I_h \nabla u||_{L_\infty} \leq C||\nabla u||_{L_\infty} \qquad \text{by continuity}$$

$\square$

Finally, the error between the Galerkin solution to the method of lines and the exact solution may be shown to be bounded.

Theorem B.3.4. *The error in the solution the the semidiscrete problem is bounded.*

$$||u_h(t) - u(t)|| \leq C \left\{ ||u_h^0 - u^0|| + \left(\frac{h}{p}\right)^2 \right\}$$

Proof. let $\theta = u_h - \tilde{u}_h$

$$\begin{aligned}
&(\theta_t, \chi) + (a(u_h)\nabla\theta, \nabla\chi) \\
&\quad = (u_{h,t}, \chi) + (a(u_h)\nabla u_h, \nabla\chi) - (\tilde{u}_{h,t}, \chi) - (a(u_h)\nabla\tilde{u}_h, \nabla\chi)
\end{aligned}$$

using that $(f(u_h, \mathbf{x}), \chi) = (u_{h,t}, \chi) + (a(u_h)\nabla u_h, \nabla\chi)$

$$\begin{aligned}
&= (f(u_h, \mathbf{x}), \chi) - (\rho_t, \chi) - (u_t, \chi) \\
&\quad - (a(u)\nabla\tilde{u}_h, \nabla\chi) + ((a(u) - a(u_h))\nabla\tilde{u}_h, \nabla\chi)
\end{aligned}$$

using that $(a(u)(\nabla\tilde{u}_h - \nabla u), \nabla\chi) = 0$

$$\begin{aligned}
&= (f(u_h, \mathbf{x}), \chi) - (\rho_t, \chi) - (u_t, \chi) \\
&\quad - (a(u)\nabla u, \nabla\chi) + ((a(u) - a(u_h))\nabla\tilde{u}_h, \nabla\chi) \\
&= (f(u_h, \mathbf{x}) - f(u, \mathbf{x}), \chi) + ((a(u) - a(u_h))\nabla\tilde{u}_h, \nabla\chi) - (\rho_t, \chi)
\end{aligned}$$

let $\chi = \theta$ and using Lemma B.3.3

$$\frac{1}{2}\frac{d}{dt}\|\theta\|^2 + \mu\|\nabla\theta\|^2 \leq C\left(\|u_h - u\|(\|\theta\| + \|\nabla\theta\|) + \|\rho_t\|\ \|\theta\|\right)$$

Poincare inequality

$$\leq C(\|\theta\| + \|\rho\| + \|\rho_t\|)\|\nabla\theta\|$$

Young's inequality

$$\leq \mu\|\nabla\theta\|^2 + C(\|\theta\|^2 + \|\rho\|^2 + \|\rho_t\|^2)$$

By Gronwall's inequality

$$\begin{aligned} ||\theta(t)||^2 &\leq \tilde{C}e^{\beta\, t}||\theta(0)||^2 + \tilde{C}\int_0^t e^{\beta\, t}\left(||\rho||^2 + ||\rho_t||^2\right)\, ds \\ &\leq C||\theta(0)||^2 + C\int_0^t \left(||\rho||^2 + ||\rho_t||^2\right)\, ds \end{aligned}$$

thus

$$||\theta(t)|| \leq C\left[||u_h^0 - u^0|| + \left(\frac{h}{p}\right)^2\right]$$

$\square$

Appendix C

Fully Discretized Equations

The equations for the calibration problem are explicitly written out in this appendix. The equations for the optimal control and mesh refinements are a straight forward extension.

C.1 Direct Sensitivity and Adjoint Methods

Start with Crank-Nicholson on Pennes Equation

$$\begin{aligned}&\int_\Omega \rho c_p \frac{u_k - u_{k-1}}{\Delta t} v_{k-\frac{1}{2}} + k(u_{k-\frac{1}{2}},\beta)\nabla u_{k-\frac{1}{2}} \cdot \nabla v_{k-\frac{1}{2}}\; dx \\ &\quad - \int_\Omega \omega(u_{k-\frac{1}{2}},\beta) c_{blood}(u_a - u_{k-\frac{1}{2}})\; v_{k-\frac{1}{2}}\; dx - \int_{\partial\Omega} h u_{k-\frac{1}{2}}\; v_{k-\frac{1}{2}}\; dA \\ &\quad = \int_\Omega Q_{laser}(\mathbf{x}) v_{k-\frac{1}{2}}\; dx - \int_{\partial\Omega} h u_\infty\; v_{k-\frac{1}{2}}\; dA \qquad \forall v_{k-\frac{1}{2}}\; k = 1,...,n\end{aligned}$$

with $u_0 = u^0(\mathbf{x})$, and $u_{k-\frac{1}{2}} = \frac{u_k + u_{k-1}}{2}$. Let

$$u_k = \sum_{i=1}^m \alpha_i^k \phi_i \qquad v_{k-\frac{1}{2}} = \sum_{i=1}^m v_i^{k-\frac{1}{2}} \phi_i$$

Then the discretized Pennes equation is equivalent to

$$M(\vec{\alpha}^k - \vec{\alpha}^{k-1}) + \vec{g}\left(\frac{\vec{\alpha}^k + \vec{\alpha}^{k-1}}{2}, \vec{\beta}\right) = \vec{f}^{k-\frac{1}{2}} \qquad k = 1,...,n \tag{C.1}$$

Where M is the mass matrix

$$M \equiv \left[\int_\Omega \rho c_p \phi_i \phi_j dx\right]$$

the vector valued function $\vec{g}$ is defined as

$$\begin{aligned} g_i(\vec{y}, \beta) \equiv & \int_\Omega k\left(\sum_j y_j \phi_j, k_0, k_1\right) \nabla\left(\sum_j y_j \phi_j\right) \cdot \nabla \phi_i \, dx \\ & + \int_\Omega -\omega\left(\sum_j y_j \phi_j, \omega_0, \omega_1\right) c_{blood}\left(u_a - \sum_j y_j \phi_j\right) \phi_i \, dx \\ & - \int_{\partial\Omega} h \sum_j y_j \phi_j \; \phi_i \, dA \end{aligned}$$

and the source term is

$$\vec{f}^{k-\frac{1}{2}} \equiv \left[\int_\Omega Q_{laser}(\mathbf{x}, t_{k-\frac{1}{2}}) \phi_i \, dx - \int_{\partial\Omega} h u_\infty \; \phi_i \, dA\right]$$

Note that

$$B(u, \beta; v) \approx B^h(u^h, \beta, v^h) \equiv \sum_{k=1}^n \Delta t \left\langle M(\vec{\alpha}^k - \vec{\alpha}^{k-1}) + \vec{g}\left(\frac{\vec{\alpha}^k + \vec{\alpha}^{k-1}}{2}, \vec{\beta}\right), \vec{v}^{k-\frac{1}{2}} \right\rangle$$

and

$$F(v) \approx F^h(v^h) \equiv \sum_{k=1}^n \Delta t \left\langle \vec{f}^{k-\frac{1}{2}}, \vec{v}^{k-\frac{1}{2}} \right\rangle$$

where $< \cdot, \cdot >$ denotes the inner product on $\mathbb{R}^m$. For the calibration problem the objective function may be written as

$$Q^h(u^h, \beta) = \sum_k \frac{1}{2} \int_\Omega \left(\sum_i \alpha_i^k \phi_i - u_{exp}^{t_k}\right)^2 dx$$

Optimization of the model parameters requires the computation of the gradient with respect to the model parameters. Formally, computation of the gradient utilizes chain rule differentiation.

$$\frac{dQ^h}{d\beta_\nu} = \frac{\partial Q^h}{\partial \beta_\nu} + \frac{\partial Q^h}{\partial u^h} \frac{\partial u^h}{\partial \beta_\nu}$$

explicitly written is

$$\frac{dQ^h}{d\beta_\nu} = \sum_{k=1}^{n} \left\langle \vec{r}(\vec{\alpha}^n), \frac{\partial \vec{\alpha}^k}{\partial \beta_\nu} \right\rangle \tag{C.2}$$

with the residual, $\vec{r}(\vec{\alpha}^k)$, defined as

$$\vec{r}(\vec{\alpha}^k) \equiv \left[\int_\Omega \left(\sum_j \alpha_j^k \phi_j - u_{exp}^{t_k} \right) \phi_i \, dx \right]$$

The *Direct Sensitivity* method of computing the gradient of the objective function is

- Differentiate (C.1) with respect to β and solve for the sensitivities of the state variables with respect to the model coefficients, $\frac{\partial \vec{\alpha}^k}{\partial \beta_\nu}$. The sensitivities may be used in (C.2) to compute the gradient.

The *Adjoint* method of computing the gradient requires solving the adjoint problem of (C.1) by stepping backwards in time. The adjoint/dual solution is used to compute the gradient. To prove that the dual solution may be used to compute the gradient exactly begin with the discretized Lagrangian.

$$\begin{aligned} L^h(u^h, \beta; p^h) = & \sum_{k=1}^{n} \frac{1}{2} \int_\Omega \left(\sum_i \alpha_i^k \phi_i - u_{exp}^{t_k} \right)^2 dx \\ & + \sum_{k=1}^{n} \Delta t \left\langle \vec{f}^{k-\frac{1}{2}} - M(\vec{\alpha}^k - \vec{\alpha}^{k-1}) - \vec{g}\left(\frac{\vec{\alpha}^k + \vec{\alpha}^{k-1}}{2}, \vec{\beta} \right), \vec{\lambda}^{k-\frac{1}{2}} \right\rangle \end{aligned}$$

with

$$p_{k-\frac{1}{2}} = \sum_{i=1}^{m} \lambda_i^{k-\frac{1}{2}} \phi_i$$

Notice that the Discretized Lagrangian is of the classical form

$$L(x, \lambda) = f(x) - \sum_i \lambda_i c_i(x)$$

where the constraints, c_i, are simply the equations of the forward problem. Computing the first order necessary conditions, the partial of the Lagrangian with respect to the adjoint variables, $\vec{\lambda}^{k-\frac{1}{2}}$, recovers the forward problem (C.1). The partial of the discretized Lagrangian with respect to the temperature field

$$\frac{\partial L^h}{\partial \alpha^k} = 0$$

yields

$$\vec{r}(\vec{\alpha}^n) = \begin{cases} M(\vec{\lambda}^{k-\frac{1}{2}} - \vec{\lambda}^{k+\frac{1}{2}}) + \frac{1}{2}\left[\frac{\partial g_i}{\partial y_j}\left(\frac{\vec{\alpha}^k + \vec{\alpha}^{k-1}}{2}, \vec{\beta}\right)\right]^T \vec{\lambda}^{k-\frac{1}{2}} & \\ \qquad + \frac{1}{2}\left[\frac{\partial g_i}{\partial y_j}\left(\frac{\vec{\alpha}^{k+1} + \vec{\alpha}^k}{2}, \vec{\beta}\right)\right]^T \vec{\lambda}^{k+\frac{1}{2}} & k = 1, ..., n-1 \\ M\vec{\lambda}^{n-\frac{1}{2}} + \frac{1}{2}\left[\frac{\partial g_i}{\partial y_j}\left(\frac{\vec{\alpha}^n + \vec{\alpha}^{n-1}}{2}, \vec{\beta}\right)\right]^T \vec{\lambda}^{n-\frac{1}{2}} & k = n \end{cases} \tag{C.3}$$

Which is a discretized form (4.6). For an *arbitrary test function in space time* the partial of the discretized semilinear form with respect to the control parameters yields

$$\frac{\partial B^h}{\partial \beta_\nu} = \sum_{k=1}^{n} \left\langle \begin{array}{l} M\left(\frac{\partial \vec{\alpha}^k}{\partial \beta_\nu} - \frac{\partial \vec{\alpha}^{k-1}}{\partial \beta_\nu}\right) \\ + \frac{1}{2}\left[\frac{\partial g_i}{\partial y_j}\left(\frac{\vec{\alpha}^k + \vec{\alpha}^{k-1}}{2}, \vec{\beta}\right)\right]\left(\frac{\partial \vec{\alpha}^k}{\partial \beta_\nu} + \frac{\partial \vec{\alpha}^{k-1}}{\partial \beta_\nu}\right) \end{array}, \vec{v}^{k-\frac{1}{2}} \right\rangle$$

rearranging and using the identity $\langle y, Ax\rangle = \langle A^T y, x\rangle$

$$\begin{aligned} = \sum_{k=1}^{n} \Bigg\langle M\left(\vec{v}^{k-\frac{1}{2}} - \vec{v}^{k+\frac{1}{2}}\right) + \frac{1}{2}\left[\frac{\partial g_i}{\partial y_j}\left(\frac{\vec{\alpha}^k + \vec{\alpha}^{k-1}}{2}, \vec{\beta}\right)\right]^T \vec{v}^{k-\frac{1}{2}} & \\ + \frac{1}{2}\left[\frac{\partial g_i}{\partial y_j}\left(\frac{\vec{\alpha}^k + \vec{\alpha}^{k-1}}{2}, \vec{\beta}\right)\right]^T \vec{v}^{k+\frac{1}{2}}, \frac{\partial \vec{\alpha}^k}{\partial \beta_\nu} \Bigg\rangle & \\ + \sum_{k=1}^{n} \left\langle \frac{\partial \vec{g}}{\partial \beta_\nu}\left(\frac{\vec{\alpha}^k + \vec{\alpha}^{k-1}}{2}, \vec{\beta}\right), \vec{v}^{k-\frac{1}{2}} \right\rangle & \end{aligned}$$

letting $\vec{v}^{k-\frac{1}{2}} = \vec{\lambda}^{k-\frac{1}{2}}$

$$\begin{aligned} &= \sum_{k=1}^{n} \left\langle \vec{r}(\vec{\alpha}^n), \frac{\partial \vec{\alpha}^k}{\partial \beta_\nu} \right\rangle + \sum_{k=1}^{n} \left\langle \frac{\partial \vec{g}}{\partial \beta_\nu} \left(\frac{\vec{\alpha}^k + \vec{\alpha}^{k-1}}{2}, \vec{\beta} \right), \vec{\lambda}^{k-\frac{1}{2}} \right\rangle \qquad \text{(C.4)} \\ &= 0 \end{aligned}$$

Notice that (C.2) appears in (C.4), thus the gradient of the objective function with respect to the control parameters may be computed *exactly* through

$$\frac{\partial Q^h}{\partial \beta_\nu} = -\sum_{k=1}^{n} \left\langle \frac{\partial \vec{g}}{\partial \beta_\nu} \left(\frac{\vec{\alpha}^k + \vec{\alpha}^{k-1}}{2}, \vec{\beta} \right), \vec{\lambda}^{k-\frac{1}{2}} \right\rangle$$

where $\vec{\lambda}^{k-\frac{1}{2}}, k = 1, ..., n$ is the solution of the adjoint formulation. From an algorithmic point of view this is equivalent to solving

$$\frac{\partial L^h}{\partial \lambda^{k-\frac{1}{2}}} = 0 \qquad \text{and} \qquad \frac{\partial L^h}{\partial \alpha^k} = 0$$

for a particular β. Then iteratively updating β to satisfy $\frac{\partial L^h}{\partial \beta_\nu} = 0$. When a β that satisfies the first order optimality conditions for the constrained problem is found, the first order necessary conditions for the unconstrained problem is recovered.

$$\frac{\partial L^h}{\partial \beta_\nu} = \sum_{k=1}^{n} \left\langle \frac{\partial \vec{g}}{\partial \beta_\nu} \left(\frac{\vec{\alpha}^k + \vec{\alpha}^{k-1}}{2}, \vec{\beta} \right), \vec{\lambda}^{k-\frac{1}{2}} \right\rangle = -\frac{\partial Q_h}{\partial \beta_\nu} = 0 \qquad \text{(C.5)}$$

The explicit discretization of the gradient for the linear terms of the constitutive equations may be written as follows.

$$\frac{\partial Q_h}{\partial k_0} = \sum_{i=1}^{n} \int_\Omega \frac{\partial k}{\partial k_0} \nabla u_i \cdot \nabla p_i dx \Delta t_i$$

$$\frac{\partial Q_h}{\partial \omega_0} = \sum_{i=1}^{n} \int_\Omega \frac{\partial \omega}{\partial \omega_0} c_b (u_a - u_i) p_i dx \Delta t_i$$

The nonlinear terms are similar

C.2 Sum Factorization

The element matrix and vector computations are a very significant portion of the overall finite element computation. Efficient schemes are needed for higher order polynomial computations. An element computation scheme based on sum factorization [25] is presented in this section. Denote $T_e : \mathbb{R}^3 \to \mathbb{R}^3$ as the mapping from he master element to physical space. The following identities are utilized throughout this section.

$$
\begin{array}{cc}
T_e(\vec{\xi}) = \vec{x} & T_e(T_e^{-1}(\vec{x})) = \vec{x} \\
T_e^{-1}(\vec{x}) = \vec{\xi} & T_e^{-1}(T_e(\vec{\xi})) = \vec{\xi}
\end{array}
$$

A basis function $\hat{\phi}$ written as the tensor product of the 1-D basis function $\hat{\phi}_i$.

$$\hat{\phi}(\vec{\xi}) = \hat{\phi}_1(\xi_1)\hat{\phi}_2(\xi_2)\hat{\phi}_3(\xi_3)$$

composed with

$$T_e^{-1}(\vec{x}) = \vec{\xi}$$

yields

$$\phi(\vec{x}) = \hat{\phi}(T_e^{-1}(\vec{x})) = \hat{\phi}_1((T_e^{-1}(\vec{x}))_1)\hat{\phi}_2((T_e^{-1}(\vec{x}))_2)\hat{\phi}_3((T_e^{-1}(\vec{x}))_3)$$

The properties of the inverse $\phi(\vec{x})$ composed with $T_e(\vec{\xi})$ yields the original function

$$\phi(T_e(\vec{\xi})) = \hat{\phi}_1(\xi_1)\hat{\phi}_2(\xi_2)\hat{\phi}_3(\xi_3)$$

The chain rule is used to obtain physical derivatives of the basis function.

$$
\begin{aligned}
\frac{\partial}{\partial x}\left(\phi(\vec{x})\right) = {} & \hat{\phi}_1'((T_e^{-1}(\vec{x}))_1)\hat{\phi}_2((T_e^{-1}(\vec{x}))_2)\hat{\phi}_3((T_e^{-1}(\vec{x}))_3)\frac{\partial (T_e^{-1}(\vec{x}))_1}{\partial x} \\
& + \hat{\phi}_1((T_e^{-1}(\vec{x}))_1)\hat{\phi}_2'((T_e^{-1}(\vec{x}))_2)\hat{\phi}_3((T_e^{-1}(\vec{x}))_3)\frac{\partial (T_e^{-1}(\vec{x}))_2}{\partial x} \\
& + \hat{\phi}_1((T_e^{-1}(\vec{x}))_1)\hat{\phi}_2((T_e^{-1}(\vec{x}))_2)\hat{\phi}_3'((T_e^{-1}(\vec{x}))_3)\frac{\partial (T_e^{-1}(\vec{x}))_3}{\partial x}
\end{aligned}
$$

$$\begin{aligned}\frac{\partial}{\partial y}\left(\phi(\vec{x})\right) = {} & \hat{\phi}_1'((T_e^{-1}(\vec{x}))_1)\hat{\phi}_2((T_e^{-1}(\vec{x}))_2)\hat{\phi}_3((T_e^{-1}(\vec{x}))_3)\frac{\partial(T_e^{-1}(\vec{x}))_1}{\partial y} \\ & + \hat{\phi}_1((T_e^{-1}(\vec{x}))_1)\hat{\phi}_2'((T_e^{-1}(\vec{x}))_2)\hat{\phi}_3((T_e^{-1}(\vec{x}))_3)\frac{\partial(T_e^{-1}(\vec{x}))_2}{\partial y} \\ & + \hat{\phi}_1((T_e^{-1}(\vec{x}))_1)\hat{\phi}_2((T_e^{-1}(\vec{x}))_2)\hat{\phi}_3'((T_e^{-1}(\vec{x}))_3)\frac{\partial(T_e^{-1}(\vec{x}))_3}{\partial y}\end{aligned}$$

$$\begin{aligned}\frac{\partial}{\partial z}\left(\phi(\vec{x})\right) = {} & \hat{\phi}_1'((T_e^{-1}(\vec{x}))_1)\hat{\phi}_2((T_e^{-1}(\vec{x}))_2)\hat{\phi}_3((T_e^{-1}(\vec{x}))_3)\frac{\partial(T_e^{-1}(\vec{x}))_1}{\partial z} \\ & + \hat{\phi}_1((T_e^{-1}(\vec{x}))_1)\hat{\phi}_2'((T_e^{-1}(\vec{x}))_2)\hat{\phi}_3((T_e^{-1}(\vec{x}))_3)\frac{\partial(T_e^{-1}(\vec{x}))_2}{\partial z} \\ & + \hat{\phi}_1((T_e^{-1}(\vec{x}))_1)\hat{\phi}_2((T_e^{-1}(\vec{x}))_2)\hat{\phi}_3'((T_e^{-1}(\vec{x}))_3)\frac{\partial(T_e^{-1}(\vec{x}))_3}{\partial z}\end{aligned}$$

to find derivatives

$$\frac{\partial(T_e^{-1}(\vec{x}))_i}{\partial x_j}$$

note that

$$\frac{\partial}{\partial x}\vec{x} = \begin{bmatrix}1\\0\\0\end{bmatrix} = \begin{bmatrix}\frac{\partial(T_e(\vec{\xi}))_1}{\partial \xi_1} & \frac{\partial(T_e(\vec{\xi}))_1}{\partial \xi_2} & \frac{\partial(T_e(\vec{\xi}))_1}{\partial \xi_3} \\ \frac{\partial(T_e(\vec{\xi}))_2}{\partial \xi_1} & \frac{\partial(T_e(\vec{\xi}))_2}{\partial \xi_2} & \frac{\partial(T_e(\vec{\xi}))_2}{\partial \xi_3} \\ \frac{\partial(T_e(\vec{\xi}))_3}{\partial \xi_1} & \frac{\partial(T_e(\vec{\xi}))_3}{\partial \xi_2} & \frac{\partial(T_e(\vec{\xi}))_3}{\partial \xi_3}\end{bmatrix}\begin{bmatrix}\frac{\partial(T_e^{-1}(\vec{x}))_1}{\partial x} \\ \frac{\partial(T_e^{-1}(\vec{x}))_2}{\partial x} \\ \frac{\partial(T_e^{-1}(\vec{x}))_3}{\partial x}\end{bmatrix}$$

$$\frac{\partial}{\partial y}\vec{x} = \begin{bmatrix}0\\1\\0\end{bmatrix} = \begin{bmatrix}\frac{\partial(T_e(\vec{\xi}))_1}{\partial \xi_1} & \frac{\partial(T_e(\vec{\xi}))_1}{\partial \xi_2} & \frac{\partial(T_e(\vec{\xi}))_1}{\partial \xi_3} \\ \frac{\partial(T_e(\vec{\xi}))_2}{\partial \xi_1} & \frac{\partial(T_e(\vec{\xi}))_2}{\partial \xi_2} & \frac{\partial(T_e(\vec{\xi}))_2}{\partial \xi_3} \\ \frac{\partial(T_e(\vec{\xi}))_3}{\partial \xi_1} & \frac{\partial(T_e(\vec{\xi}))_3}{\partial \xi_2} & \frac{\partial(T_e(\vec{\xi}))_3}{\partial \xi_3}\end{bmatrix}\begin{bmatrix}\frac{\partial(T_e^{-1}(\vec{x}))_1}{\partial y} \\ \frac{\partial(T_e^{-1}(\vec{x}))_2}{\partial y} \\ \frac{\partial(T_e^{-1}(\vec{x}))_3}{\partial y}\end{bmatrix}$$

$$\frac{\partial}{\partial z}\vec{x} = \begin{bmatrix} 0 \\ 0 \\ 1 \end{bmatrix} = \begin{bmatrix} \frac{\partial (T_e(\vec{\xi}))_1}{\partial \xi_1} & \frac{\partial (T_e(\vec{\xi}))_1}{\partial \xi_2} & \frac{\partial (T_e(\vec{\xi}))_1}{\partial \xi_3} \\ \frac{\partial (T_e(\vec{\xi}))_2}{\partial \xi_1} & \frac{\partial (T_e(\vec{\xi}))_2}{\partial \xi_2} & \frac{\partial (T_e(\vec{\xi}))_2}{\partial \xi_3} \\ \frac{\partial (T_e(\vec{\xi}))_3}{\partial \xi_1} & \frac{\partial (T_e(\vec{\xi}))_3}{\partial \xi_2} & \frac{\partial (T_e(\vec{\xi}))_3}{\partial \xi_3} \end{bmatrix} \begin{bmatrix} \frac{\partial (T_e^{-1}(\vec{x}))_1}{\partial z} \\ \frac{\partial (T_e^{-1}(\vec{x}))_2}{\partial z} \\ \frac{\partial (T_e^{-1}(\vec{x}))_3}{\partial z} \end{bmatrix}$$

The diffusion, advection, and reaction terms involved in the optimization of Pennes model must be explicitly written out in terms of the 1-D basis functions to understand how to exploit the tensor product structure. For the stiffness matrix

$$\int_\Omega k(u)\nabla\phi_i(\vec{x})\cdot\nabla\phi_j(\vec{x})\;dx = \int_\Omega k(u)(\phi_{i,x}\phi_{j,x}+\phi_{i,y}\phi_{j,y}+\phi_{i,z}\phi_{j,z})\;dx$$

$$= \int_{\hat{\Omega}} k(u) \left\{ \begin{array}{l}
\begin{pmatrix} \hat{\phi}'_{i1}(\xi_1)\hat{\phi}_{i2}(\xi_2)\hat{\phi}_{i3}(\xi_3)\frac{\partial(T_e^{-1}(\vec{x}))_1}{\partial x} \\ +\,\hat{\phi}_{i1}(\xi_1)\hat{\phi}'_{i2}(\xi_2)\hat{\phi}_{i3}(\xi_3)\frac{\partial(T_e^{-1}(\vec{x}))_2}{\partial x} \\ +\,\hat{\phi}_{i1}(\xi_1)\hat{\phi}_{i2}(\xi_2)\hat{\phi}'_{i3}(\xi_3)\frac{\partial(T_e^{-1}(\vec{x}))_3}{\partial x} \end{pmatrix}
\begin{pmatrix} \hat{\phi}'_{j1}(\xi_1)\hat{\phi}_{j2}(\xi_2)\hat{\phi}_{j3}(\xi_3)\frac{\partial(T_e^{-1}(\vec{x}))_1}{\partial x} \\ +\,\hat{\phi}_{j1}(\xi_1)\hat{\phi}'_{j2}(\xi_2)\hat{\phi}_{j3}(\xi_3)\frac{\partial(T_e^{-1}(\vec{x}))_2}{\partial x} \\ +\,\hat{\phi}_{j1}(\xi_1)\hat{\phi}_{j2}(\xi_2)\hat{\phi}'_{j3}(\xi_3)\frac{\partial(T_e^{-1}(\vec{x}))_3}{\partial x} \end{pmatrix} \\
+\begin{pmatrix} \hat{\phi}'_{i1}(\xi_1)\hat{\phi}_{i2}(\xi_2)\hat{\phi}_{i3}(\xi_3)\frac{\partial(T_e^{-1}(\vec{x}))_1}{\partial y} \\ +\,\hat{\phi}_{i1}(\xi_1)\hat{\phi}'_{i2}(\xi_2)\hat{\phi}_{i3}(\xi_3)\frac{\partial(T_e^{-1}(\vec{x}))_2}{\partial y} \\ +\,\hat{\phi}_{i1}(\xi_1)\hat{\phi}_{i2}(\xi_2)\hat{\phi}'_{i3}(\xi_3)\frac{\partial(T_e^{-1}(\vec{x}))_3}{\partial y} \end{pmatrix}
\begin{pmatrix} \hat{\phi}'_{j1}(\xi_1)\hat{\phi}_{j2}(\xi_2)\hat{\phi}_{j3}(\xi_3)\frac{\partial(T_e^{-1}(\vec{x}))_1}{\partial y} \\ +\,\hat{\phi}_{j1}(\xi_1)\hat{\phi}'_{j2}(\xi_2)\hat{\phi}_{j3}(\xi_3)\frac{\partial(T_e^{-1}(\vec{x}))_2}{\partial y} \\ +\,\hat{\phi}_{j1}(\xi_1)\hat{\phi}_{j2}(\xi_2)\hat{\phi}'_{j3}(\xi_3)\frac{\partial(T_e^{-1}(\vec{x}))_3}{\partial y} \end{pmatrix} \\
+\begin{pmatrix} \hat{\phi}'_{i1}(\xi_1)\hat{\phi}_{i2}(\xi_2)\hat{\phi}_{i3}(\xi_3)\frac{\partial(T_e^{-1}(\vec{x}))_1}{\partial z} \\ +\,\hat{\phi}_{i1}(\xi_1)\hat{\phi}'_{i2}(\xi_2)\hat{\phi}_{i3}(\xi_3)\frac{\partial(T_e^{-1}(\vec{x}))_2}{\partial z} \\ +\,\hat{\phi}_{i1}(\xi_1)\hat{\phi}_{i2}(\xi_2)\hat{\phi}'_{i3}(\xi_3)\frac{\partial(T_e^{-1}(\vec{x}))_3}{\partial z} \end{pmatrix}
\begin{pmatrix} \hat{\phi}'_{j1}(\xi_1)\hat{\phi}_{j2}(\xi_2)\hat{\phi}_{j3}(\xi_3)\frac{\partial(T_e^{-1}(\vec{x}))_1}{\partial z} \\ +\,\hat{\phi}_{j1}(\xi_1)\hat{\phi}'_{j2}(\xi_2)\hat{\phi}_{j3}(\xi_3)\frac{\partial(T_e^{-1}(\vec{x}))_2}{\partial z} \\ +\,\hat{\phi}_{j1}(\xi_1)\hat{\phi}_{j2}(\xi_2)\hat{\phi}'_{j3}(\xi_3)\frac{\partial(T_e^{-1}(\vec{x}))_3}{\partial z} \end{pmatrix}
\end{array} \right\} J(\vec{\xi})d\xi$$

$$= \int_{\hat{\Omega}} k(u) \sum_{k=1}^{3} \left\{ \begin{array}{l}
\hat{\phi}'_{i1}(\xi_1)\hat{\phi}_{i2}(\xi_2)\hat{\phi}_{i3}(\xi_3)\frac{\partial(T_e^{-1}(\vec{x}))_1}{\partial x_k}\hat{\phi}'_{j1}(\xi_1)\hat{\phi}_{j2}(\xi_2)\hat{\phi}_{j3}(\xi_3)\frac{\partial(T_e^{-1}(\vec{x}))_1}{\partial x_k} \\
+\hat{\phi}_{i1}(\xi_1)\hat{\phi}'_{i2}(\xi_2)\hat{\phi}_{i3}(\xi_3)\frac{\partial(T_e^{-1}(\vec{x}))_2}{\partial x_k}\hat{\phi}'_{j1}(\xi_1)\hat{\phi}_{j2}(\xi_2)\hat{\phi}_{j3}(\xi_3)\frac{\partial(T_e^{-1}(\vec{x}))_1}{\partial x_k} \\
+\hat{\phi}_{i1}(\xi_1)\hat{\phi}_{i2}(\xi_2)\hat{\phi}'_{i3}(\xi_3)\frac{\partial(T_e^{-1}(\vec{x}))_3}{\partial x_k}\hat{\phi}'_{j1}(\xi_1)\hat{\phi}_{j2}(\xi_2)\hat{\phi}_{j3}(\xi_3)\frac{\partial(T_e^{-1}(\vec{x}))_1}{\partial x_k} \\
+\hat{\phi}'_{i1}(\xi_1)\hat{\phi}_{i2}(\xi_2)\hat{\phi}_{i3}(\xi_3)\frac{\partial(T_e^{-1}(\vec{x}))_1}{\partial x_k}\hat{\phi}_{j1}(\xi_1)\hat{\phi}'_{j2}(\xi_2)\hat{\phi}_{j3}(\xi_3)\frac{\partial(T_e^{-1}(\vec{x}))_2}{\partial x_k} \\
+\hat{\phi}_{i1}(\xi_1)\hat{\phi}'_{i2}(\xi_2)\hat{\phi}_{i3}(\xi_3)\frac{\partial(T_e^{-1}(\vec{x}))_2}{\partial x_k}\hat{\phi}_{j1}(\xi_1)\hat{\phi}'_{j2}(\xi_2)\hat{\phi}_{j3}(\xi_3)\frac{\partial(T_e^{-1}(\vec{x}))_2}{\partial x_k} \\
+\hat{\phi}_{i1}(\xi_1)\hat{\phi}_{i2}(\xi_2)\hat{\phi}'_{i3}(\xi_3)\frac{\partial(T_e^{-1}(\vec{x}))_3}{\partial x_k}\hat{\phi}_{j1}(\xi_1)\hat{\phi}'_{j2}(\xi_2)\hat{\phi}_{j3}(\xi_3)\frac{\partial(T_e^{-1}(\vec{x}))_2}{\partial x_k} \\
+\hat{\phi}'_{i1}(\xi_1)\hat{\phi}_{i2}(\xi_2)\hat{\phi}_{i3}(\xi_3)\frac{\partial(T_e^{-1}(\vec{x}))_1}{\partial x_k}\hat{\phi}_{j1}(\xi_1)\hat{\phi}_{j2}(\xi_2)\hat{\phi}'_{j3}(\xi_3)\frac{\partial(T_e^{-1}(\vec{x}))_3}{\partial x_k} \\
+\hat{\phi}_{i1}(\xi_1)\hat{\phi}'_{i2}(\xi_2)\hat{\phi}_{i3}(\xi_3)\frac{\partial(T_e^{-1}(\vec{x}))_2}{\partial x_k}\hat{\phi}_{j1}(\xi_1)\hat{\phi}_{j2}(\xi_2)\hat{\phi}'_{j3}(\xi_3)\frac{\partial(T_e^{-1}(\vec{x}))_3}{\partial x_k} \\
+\hat{\phi}_{i1}(\xi_1)\hat{\phi}_{i2}(\xi_2)\hat{\phi}'_{i3}(\xi_3)\frac{\partial(T_e^{-1}(\vec{x}))_3}{\partial x_k}\hat{\phi}_{j1}(\xi_1)\hat{\phi}_{j2}(\xi_2)\hat{\phi}'_{j3}(\xi_3)\frac{\partial(T_e^{-1}(\vec{x}))_3}{\partial x_k}
\end{array} \right\} J(\vec{\xi})d\xi$$

For the damping matrix

$$
\begin{aligned}
\int_\Omega \frac{dk}{du}(u)\nabla u \cdot \nabla \phi_i(\vec{x})\phi_j \; dx &= \int_\Omega \frac{dk}{du}(u)(u_x\phi_{i,x} + u_y\phi_{i,y} + u_z\phi_{i,z}) \; \phi_j \; dx \\
&= \int_{\hat{\Omega}} \frac{dk}{du}(u) \left\{ \begin{array}{rl}
u_x & \begin{pmatrix} \hat{\phi}'_{i1}(\xi_1)\hat{\phi}_{i2}(\xi_2)\hat{\phi}_{i3}(\xi_3)\frac{\partial(T_e^{-1}(\vec{x}))_1}{\partial x} \\ + \hat{\phi}_{i1}(\xi_1)\hat{\phi}'_{i2}(\xi_2)\hat{\phi}_{i3}(\xi_3)\frac{\partial(T_e^{-1}(\vec{x}))_2}{\partial x} \\ + \hat{\phi}_{i1}(\xi_1)\hat{\phi}_{i2}(\xi_2)\hat{\phi}'_{i3}(\xi_3)\frac{\partial(T_e^{-1}(\vec{x}))_3}{\partial x} \end{pmatrix} \\
+u_y & \begin{pmatrix} \hat{\phi}'_{i1}(\xi_1)\hat{\phi}_{i2}(\xi_2)\hat{\phi}_{i3}(\xi_3)\frac{\partial(T_e^{-1}(\vec{x}))_1}{\partial y} \\ + \hat{\phi}_{i1}(\xi_1)\hat{\phi}'_{i2}(\xi_2)\hat{\phi}_{i3}(\xi_3)\frac{\partial(T_e^{-1}(\vec{x}))_2}{\partial y} \\ + \hat{\phi}_{i1}(\xi_1)\hat{\phi}_{i2}(\xi_2)\hat{\phi}'_{i3}(\xi_3)\frac{\partial(T_e^{-1}(\vec{x}))_3}{\partial y} \end{pmatrix} \\
+u_z & \begin{pmatrix} \hat{\phi}'_{i1}(\xi_1)\hat{\phi}_{i2}(\xi_2)\hat{\phi}_{i3}(\xi_3)\frac{\partial(T_e^{-1}(\vec{x}))_1}{\partial z} \\ + \hat{\phi}_{i1}(\xi_1)\hat{\phi}'_{i2}(\xi_2)\hat{\phi}_{i3}(\xi_3)\frac{\partial(T_e^{-1}(\vec{x}))_2}{\partial z} \\ + \hat{\phi}_{i1}(\xi_1)\hat{\phi}_{i2}(\xi_2)\hat{\phi}'_{i3}(\xi_3)\frac{\partial(T_e^{-1}(\vec{x}))_3}{\partial z} \end{pmatrix}
\end{array} \right\} \hat{\phi}_{j1}(\xi_1)\hat{\phi}_{j2}(\xi_2)\hat{\phi}_{j3}(\xi_3) \; J(\vec{\xi})d\xi
\end{aligned}
$$

Finally for the reaction term

$$
\int_\Omega \omega(u)\phi_i \; \phi_j \; dx = \int_{\hat{\Omega}} \omega(u)\hat{\phi}_{i1}(\xi_1)\hat{\phi}_{i2}(\xi_2)\hat{\phi}_{i3}(\xi_3)\hat{\phi}_{j1}(\xi_1)\hat{\phi}_{j2}(\xi_2)\hat{\phi}_{j3}(\xi_3) \; J(\vec{\xi})d\xi
$$

Algorithms C.1 and C.2 compare a naive $\mathcal{O}(p^9)$ element matrix computation implementation to the sum factorization $\mathcal{O}(p^7)$ implementation.

C.3 Penalty Term

The graph shown in Figure C.1 is an example of the observed calibration objective function, equation (3.1), plotted against the x_0 and y_0 laser parameters. Figure C.1 shows no clear minimum, implying that a pure unconstrained optimization algorithm would not work for model calibration. Early versions of the optimization algorithms utilized a penalty term with the objective functions to keep the model parameters within physically acceptable bounds. However, the bound constrained optimization algorithms within TAO [6] were

Algorithm C.1 Naive Implementation

```
$A(:,:,:,:,:,:) = ZERO$
for $i1 = 0, 1, 2, ..., p_x$ do
  for $j1 = 0, 1, 2, ..., p_x$ do
    for $i2 = 0, 1, 2, ..., p_y$ do
      for $j2 = 0, 1, 2, ..., p_y$ do
        for $i3 = 0, 1, 2, ..., p_z$ do
          for $j3 = 0, 1, 2, ..., p_z$ do
            for $l = 0, 1, 2, ..., p_x$ do
              for $m = 0, 1, 2, ..., p_y$ do
                for $n = 0, 1, 2, ..., p_z$ do
                  $A(i1, j1, i2, j2, i3, j3) = A(i1, j1, i2, j2, i3, j3) + D(\xi_{1,l}, \xi_{2,m}, \xi_{3,n}) \cdot \phi_{i_1}(\xi_{1,l})\chi_{j_1}(\xi_{1,l})\ \phi_{i_2}(\xi_{2,m})\chi_{j_2}(\xi_{2,m})\ \phi_{i_3}(\xi_{3,n})\chi_{j_3}(\xi_{3,n})$
                end for
              end for
            end for
          end for
        end for
      end for
    end for
  end for
end for
```

found to be far superior to the penalty approach. The penalty term method is briefly discussed for completeness. The penalty function, $\Phi(\beta)$, considered was of the form

$$\Phi(\beta) = \sum_{i=1}^{N_{params}} \exp\left(\gamma \frac{\beta_i - \beta_i^{UB}}{\beta_i^{UB} - \beta_i^{LB}}\right) + \exp\left(-\gamma \frac{\beta_i - \beta_i^{LB}}{\beta_i^{UB} - \beta_i^{LB}}\right)$$

The dimension of the parameter space is denoted N_{params}. β_i denotes a particular parameter. The physically acceptable lower and upper bounds of the parameter, β_i, is denoted by β_i^{LB} and β_i^{UB}, respectively. The penalty term is scaled by $\gamma = 1000.0$. Large values of gamma is seen to make the unconstrained optimization algorithms unstable.

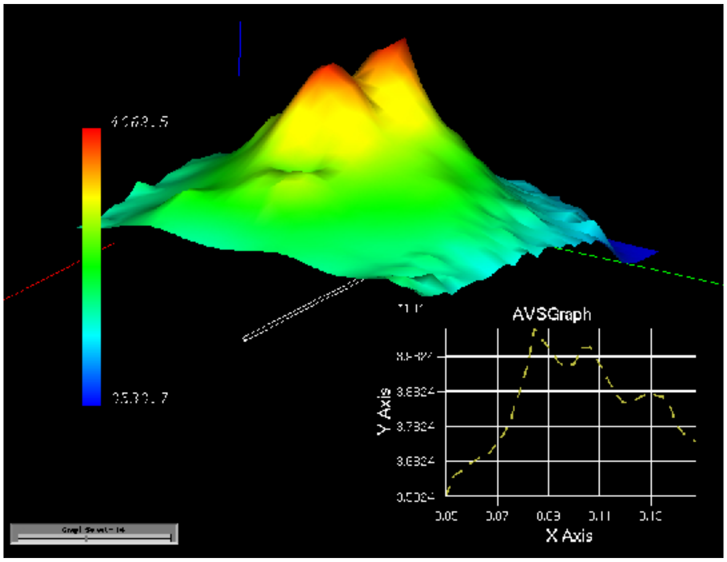

Figure C.1: Objective Function

C.4 Higher Accuracy Discretization of Equations

A higher accuracy discretization of Pennes model is developed in this section. The following Galerkin representation of the temperature field and adjoint variable is assumed.

$$u(\mathbf{x},t) = \sum_{k=1}^{N_{step}} \sum_{j=1}^{N_{dof}} \alpha_j^k(t)\phi_j(\mathbf{x}) \qquad\qquad p(\mathbf{x},t) = \sum_{k=1}^{N_{step}} \sum_{i=1}^{N_{dof}} \lambda_i^k(t)\phi_i(\mathbf{x})$$

where

$$\alpha_j^k(t) = \begin{cases} \dfrac{t_k - t}{t_k - t_{k-1}}\alpha_j^{k-1} + \dfrac{t - t_{k-1}}{t_k - t_{k-1}}\alpha_j^k, & t \in [t_{k-1}, t_k) \\ 0 & , \quad \text{otherwise} \end{cases}$$

$$\lambda_i^k(t) = \begin{cases} \lambda_i^k, \ t \in [t_{k-1}, t_k) \\ 0, \quad \text{otherwise} \end{cases}$$

The governing PDE equation is

$$\begin{aligned} C(u, \beta; v) = &\int_0^T \int_\Omega \rho c_p \frac{\partial u}{\partial t} \ v \ dxdt + \int_0^T \int_\Omega k(u, \beta) \nabla u \cdot \nabla v \ dxdt \\ &+ \int_0^T \int_\Omega \omega(u, \beta) c_{blood}(u - u_a) \ v \ dxdt + \int_0^T \int_{\partial\Omega_C} h(u - u_\infty) \ v \ dxdt \\ &- \int_0^T \int_\Omega Q_{laser}(\mathbf{x}, t, \beta) v \ dxdt + \int_0^T \int_{\partial\Omega_N} \mathcal{G} \ v \ dAdt \end{aligned}$$

with the initial condition given as

$$(u^0 - u_0, v) = \left(\sum_{j=1}^{N_{dof}} \alpha_j^0 \phi_j - u_0, v \right) = 0 \qquad \forall v \in H^1(\Omega)$$

Assuming that the test function and laser source term are piece-wise constant in time

$$v(\mathbf{x}, t) = \sum_{k=1}^{N_{step}} \sum_{i=1}^{N_{dof}} v_i^k(t) \phi_i(\mathbf{x}) \qquad v_i^k(t) = \begin{cases} v_i^k, & t \in [t_{k-1}, t_k) \\ 0, & \text{otherwise} \end{cases}$$

$$Q_{laser}(\mathbf{x}, t) = 3 P_k \mu_a \mu_{tr} \frac{\exp(-\mu_{eff} \|\mathbf{x} - \mathbf{x}_0\|)}{4\pi \|\mathbf{x} - \mathbf{x}_0\|} \qquad t \in [t_{k-1}, t_k)$$

the governing equations may be solved with the following time stepping scheme

$$\begin{aligned} \Delta t_k \ &\int_\Omega \rho c_p \frac{u_k - u_{k-1}}{\Delta t_k} v_k + \int_{t_{k-1}}^{t_k} \int_\Omega k(u, \beta) \nabla u \cdot \nabla v_k + \omega(u, \beta) c_{blood}(u - u_a) \ v_k \ dxdt \\ &+ \Delta t_k \int_{\partial\Omega_C} h(u_{k-\frac{1}{2}} - u_\infty) \ v_k \ dA = \Delta t_k \ \int_\Omega Q_{laser}(\mathbf{x}, t_k, \beta) v_k \ dx \\ &- \int_{t_{k-1}}^{t_k} \int_{\partial\Omega_N} g \ v_k \ dA \qquad \forall v_k \qquad k = 1, 2, ..., N_{step} \end{aligned}$$

where (using Einstein summation notation)

$$u_k = \alpha_j^k \phi_j(\mathbf{x}) \qquad u_{k-\frac{1}{2}} = \frac{\alpha_j^{k-1} + \alpha_j^k}{2} \phi_j(\mathbf{x}) \qquad v_k = v_i^k \phi_i(\mathbf{x})$$

Under the following assumptions on the thermal conductivity and blood perfusivity

$$
\begin{aligned}
k(u,\beta) &= \frac{t_k - t}{t_k - t_{k-1}} k(u_{k-1}) + \frac{t - t_{k-1}}{t_k - t_{k-1}} k(u_k) \\
\omega(u,\beta) &= \frac{t_k - t}{t_k - t_{k-1}} \omega(u_{k-1}) + \frac{t - t_{k-1}}{t_k - t_{k-1}} \omega(u_k)
\end{aligned}
$$

the equations further reduce to

$$
\begin{aligned}
\Delta t_k \ \int_\Omega \rho c_p \frac{u_k - u_{k-1}}{\Delta t_k} v_k \ dx + \Delta t_k \int_\Omega
\left(\begin{array}{c}
\left[\begin{array}{l} \dfrac{1}{3} k(u_{k-1},\beta) \\ + \dfrac{1}{6} k(u_k,\beta) \end{array} \right] \nabla u_{k-1} \\
+ \left[\begin{array}{l} \dfrac{1}{6} k(u_{k-1},\beta) \\ + \dfrac{1}{3} k(u_k,\beta) \end{array} \right] \nabla u_k
\end{array} \right) \cdot \nabla v_k \ dx \\
+ \Delta t_k \int_\Omega c_{blood}
\left(\begin{array}{l}
\left[\dfrac{1}{3} \omega(u_{k-1},\beta) + \dfrac{1}{6} \omega(u_k,\beta) \right] u_{k-1} \\
+ \left[\dfrac{1}{6} \omega(u_{k-1},\beta) + \dfrac{1}{3} \omega(u_k,\beta) \right] u_k \\
- \dfrac{\omega(u_{k-1},\beta) + \omega(u_k,\beta)}{2} u_a
\end{array} \right) v_k \ dx \\
+ \Delta t_k \int_{\partial\Omega_C} h(u_{k-\frac{1}{2}} - u_\infty) \ v_k \ dA \\
= \Delta t_k \ \int_\Omega Q_{laser}(\mathbf{x}, t_k, \beta) v_k \ dx - \int_{t_{k-1}}^{t_k} \int_{\partial\Omega_N} g \ v_k \ dA \qquad \forall v_k \ k = 1, 2, ..., n
\end{aligned}
$$

At every time step, the temperature from the previous timestep is known. The resulting set of nonlinear equations for u_k at every time step is

$$
\begin{aligned}
&\Delta t_k \int_\Omega \rho c_p \frac{u_k - u_{k-1}}{\Delta t_k} \phi_i \, dx + \Delta t_k \int_\Omega \left(\begin{array}{c} \left[\begin{array}{l} \frac{1}{3} k(u_{k-1}, \beta) \\ + \frac{1}{6} k(u_k, \beta) \end{array} \right] \nabla u_{k-1} \\ + \left[\begin{array}{l} \frac{1}{6} k(u_{k-1}, \beta) \\ + \frac{1}{3} k(u_k, \beta) \end{array} \right] \nabla u_k \end{array} \right) \cdot \nabla \phi_i \, dx \\
&\quad + \Delta t_k \int_\Omega c_{blood} \left(\begin{array}{l} \left[\frac{1}{3} \omega(u_{k-1}, \beta) + \frac{1}{6} \omega(u_k, \beta) \right] u_{k-1} \\ + \left[\frac{1}{6} \omega(u_{k-1}, \beta) + \frac{1}{3} \omega(u_k, \beta) \right] u_k \\ - \frac{\omega(u_{k-1}, \beta) + \omega(u_k, \beta)}{2} u_a \end{array} \right) \phi_i \, dx \\
&\quad + \Delta t_k \int_{\partial \Omega_C} h(u_{k-\frac{1}{2}} - u_\infty) \, \phi_i \, dA - \Delta t_k \int_\Omega Q_{laser}(\mathbf{x}, t_k, \beta) \phi_i \, dx \\
&\quad + \int_{t_{k-1}}^{t_k} \int_{\partial \Omega_N} g \, \phi_i \, dA = 0 \qquad i = 1, 2, ..., N_{dof}
\end{aligned}
$$

which is of the form: find $\vec{\alpha}^k = (\alpha_1^k, \alpha_2^k, ...)$ such that

$$\vec{f}(\vec{\alpha}^k) = \vec{0}$$

the Jacobian of this system of equations is

$$
\begin{aligned}
\frac{\partial f_i}{\partial \alpha_j^k} = & \Delta t_k \int_\Omega \frac{\rho c_p}{\Delta t_k} \phi_j \phi_i \, dx + \Delta t_k \int_\Omega \left(\begin{array}{l} \frac{1}{6}\frac{\partial k}{\partial u}(u_k,\beta)\phi_j \nabla u_{k-1} \\ + \frac{1}{3}\frac{\partial k}{\partial u}(u_k,\beta)\phi_j \nabla u_k \\ + \left[\begin{array}{l} \frac{1}{6} k(u_{k-1},\beta) \\ + \frac{1}{3} k(u_k,\beta) \end{array} \right] \nabla \phi_j \end{array} \right) \cdot \nabla \phi_i \, dx \\
& + \Delta t_k \int_\Omega c_{blood} \left(\begin{array}{l} \frac{1}{6}\frac{\partial \omega}{\partial u}(u_k,\beta)\phi_j u_{k-1} + \frac{1}{3}\frac{\partial \omega}{\partial u}(u_k,\beta)\phi_j u_k \\ + \left[\begin{array}{l} \frac{1}{6}\omega(u_{k-1},\beta) \\ + \frac{1}{3}\omega(u_k,\beta) \end{array} \right] \phi_j - \frac{1}{2}\frac{\partial \omega}{\partial u}(u_k,\beta)\phi_j u_a \end{array} \right) \phi_i \, dx \\
& + \Delta t_k \frac{1}{2} \int_{\partial \Omega_C} h \phi_j \, \phi_i \, dA
\end{aligned}
$$

simplifying

$$
\begin{aligned}
\frac{\partial f_i}{\partial \alpha_j^k} = & \Delta t_k \int_\Omega \frac{\rho c_p}{\Delta t_k} \phi_j \phi_i \, dx + \Delta t_k \int_\Omega \left(\begin{array}{l} \frac{\partial k}{\partial u}(u_k,\beta) \nabla u_{k-\frac{1}{2}} \phi_j \\ + \left[\begin{array}{l} \frac{1}{6} k(u_{k-1},\beta) \\ + \frac{1}{3} k(u_k,\beta) \end{array} \right] \nabla \phi_j \end{array} \right) \cdot \nabla \phi_i \, dx \\
& + \Delta t_k \int_\Omega c_{blood} \left(\begin{array}{l} \left[\frac{\partial \omega}{\partial u}(u_k,\beta) u_{k-\frac{1}{2}} - \frac{1}{2}\frac{\partial \omega}{\partial u}(u_k,\beta) u_a \right] \phi_j \\ + \left[\frac{1}{6}\omega(u_{k-1},\beta) + \frac{1}{3}\omega(u_k,\beta) \right] \phi_j \end{array} \right) \phi_i \, dx \\
& + \Delta t_k \frac{1}{2} \int_{\partial \Omega_C} h \phi_j \, \phi_i \, dA
\end{aligned}
$$

Note that for the case of constant coefficients the method reduces to a Crank-Nicolson approach.

Assuming the same Galerkin representation as before

$$\begin{aligned}
Q(u,\beta) &= \frac{1}{2}\int_0^T \int_\Omega \rho c_p \chi(\mathbf{x})(u(\mathbf{x},t) - u^{exp}(\mathbf{x},t))^2 \; dxdt \\
&= \frac{1}{2}\sum_{k=1}^{N_{step}} \int_{t_{k-1}}^{t_k} \int_\Omega \rho c_p \chi(\mathbf{x})(u(\mathbf{x},t) - u^{exp}(\mathbf{x},t))^2 \; dxdt \\
&= \frac{1}{6}\sum_{k=1}^{N_{step}} \Delta t_k \int_\Omega \rho c_p \chi(\mathbf{x}) \frac{(u_k - u_k^{exp})^3 - (u_{k-1} - u_{k-1}^{exp})^3}{(u_k - u_k^{exp}) - (u_{k-1} - u_{k-1}^{exp})} \; dx
\end{aligned}$$

The gradient of the quantity of interest is needed for calibration.

$$\begin{aligned}
\frac{\partial Q(u,\beta)}{\partial \beta} &= \sum_{k=1}^{N_{step}} \int_{t_{k-1}}^{t_k} \int_\Omega \rho c_p \chi(\mathbf{x})(u(\mathbf{x},t) - u^{exp}(\mathbf{x},t)) \frac{\partial u}{\partial \beta} \; dxdt \\
&= \sum_{k=1}^{N_{step}} \Delta t_k \int_\Omega \rho c_p \chi(\mathbf{x}) \begin{pmatrix} \left[\frac{1}{3}(u_{k-1} - u_{k-1}^{exp}) + \frac{1}{6}(u_k - u_k^{exp})\right] \frac{\partial u_{k-1}}{\partial \beta} \\ + \left[\frac{1}{6}(u_{k-1} - u_{k-1}^{exp}) + \frac{1}{3}(u_k - u_k^{exp})\right] \frac{\partial u_k}{\partial \beta} \end{pmatrix} \; dx
\end{aligned}$$

Taking the derivative of the discretized equations with respect to the calibration variable yields the following:

$$\begin{aligned}
&\Delta t_k \int_\Omega \frac{\rho c_p}{\Delta t_k} \left(\frac{\partial u_k}{\partial \beta} - \frac{\partial u_{k-1}}{\partial \beta} \right) v_k \; dx \\
&\quad + \Delta t_k \int_\Omega \left(\left[\frac{1}{3}\frac{\partial k}{\partial u}(u_{k-1},\beta)\frac{\partial u_{k-1}}{\partial \beta} + \frac{1}{6}\frac{\partial k}{\partial u}(u_k,\beta)\frac{\partial u_k}{\partial \beta} \right] \nabla u_{k-1} + \left[\frac{1}{3}k(u_{k-1},\beta) + \frac{1}{6}k(u_k,\beta) \right] \nabla \frac{\partial u_{k-1}}{\partial \beta} \right) \cdot \nabla v_k \; dx \\
&\quad + \Delta t_k \int_\Omega \left(\left[\frac{1}{6}\frac{\partial k}{\partial u}(u_{k-1},\beta)\frac{\partial u_{k-1}}{\partial \beta} + \frac{1}{3}\frac{\partial k}{\partial u}(u_k,\beta)\frac{\partial u_k}{\partial \beta} \right] \nabla u_k + \left[\frac{1}{6}k(u_{k-1},\beta) + \frac{1}{3}k(u_k,\beta) \right] \nabla \frac{\partial u_k}{\partial \beta} \right) \cdot \nabla v_k \; dx \\
&\quad + \Delta t_k \int_\Omega c_{blood} \left(\left[\frac{1}{3}\frac{\partial \omega}{\partial u}(u_{k-1},\beta)\frac{\partial u_{k-1}}{\partial \beta} + \frac{1}{6}\frac{\partial \omega}{\partial u}(u_k,\beta)\frac{\partial u_k}{\partial \beta} \right] u_{k-1} + \left[\frac{1}{3}\omega(u_{k-1},\beta) + \frac{1}{6}\omega(u_k,\beta) \right] \frac{\partial u_{k-1}}{\partial \beta} \right) v_k \; dx \\
&\quad + \Delta t_k \int_\Omega c_{blood} \left(\left[\frac{1}{6}\frac{\partial \omega}{\partial u}(u_{k-1},\beta)\frac{\partial u_{k-1}}{\partial \beta} + \frac{1}{3}\frac{\partial \omega}{\partial u}(u_k,\beta)\frac{\partial u_k}{\partial \beta} \right] u_k + \left[\frac{1}{6}\omega(u_{k-1},\beta) + \frac{1}{3}\omega(u_k,\beta) \right] \frac{\partial u_k}{\partial \beta} \right) v_k \; dx \\
&\quad - \Delta t_k \int_\Omega c_{blood} \left(\frac{1}{2} \left[\frac{\partial \omega}{\partial u}(u_{k-1},\beta)\frac{\partial u_{k-1}}{\partial \beta} + \frac{\partial \omega}{\partial u}(u_k,\beta)\frac{\partial u_k}{\partial \beta} \right] u_a \right) v_k \; dx + \Delta t_k \int_{\partial\Omega_C} \frac{h}{2} \left[\frac{\partial u_{k-1}}{\partial \beta} + \frac{\partial u_k}{\partial \beta} \right] \; v_k \; dA \\
&\quad + \Delta t_k \int_\Omega \left(\left[\frac{1}{3}\frac{\partial k}{\partial \beta}(u_{k-1},\beta) + \frac{1}{6}\frac{\partial k}{\partial \beta}(u_k,\beta) \right] \nabla u_{k-1} + \left[\frac{1}{6}\frac{\partial k}{\partial \beta}(u_{k-1},\beta) + \frac{1}{3}\frac{\partial k}{\partial \beta}(u_k,\beta) \right] \nabla u_k \right) \cdot \nabla v_k \; dx \\
&\quad + \Delta t_k \int_\Omega c_{blood} \left(\left[\frac{1}{3}\frac{\partial \omega}{\partial \beta}(u_{k-1},\beta) + \frac{1}{6}\frac{\partial \omega}{\partial \beta}(u_k,\beta) \right] u_{k-1} + \left[\frac{1}{6}\frac{\partial \omega}{\partial \beta}(u_{k-1},\beta) + \frac{1}{3}\frac{\partial \omega}{\partial \beta}(u_k,\beta) \right] u_k \right) v_k \; dx \\
&\quad - \Delta t_k \int_\Omega c_{blood} \left(\frac{\frac{\partial \omega}{\partial \beta}(u_{k-1},\beta) + \frac{\partial \omega}{\partial \beta}(u_k,\beta)}{2} \right) u_a \; v_k \; dx - \Delta t_k \; \int_\Omega \frac{\partial Q_{laser}}{\partial \beta}(\mathbf{x},t_k,\beta) v_k \; dx = 0 \qquad k = 1, 2, ..., N_{step}
\end{aligned}$$

rearranging yields

$$\begin{aligned}
\Delta t_k \ \int_\Omega & \frac{\rho c_p}{\Delta t_k} \frac{\partial u_k}{\partial \beta} v_k + \frac{1}{6} \frac{\partial k}{\partial u}(u_k, \beta) \frac{\partial u_k}{\partial \beta} \nabla u_{k-1} \cdot \nabla v_k + \frac{1}{6} \frac{\partial \omega}{\partial u}(u_k, \beta) \frac{\partial u_k}{\partial \beta} u_{k-1} v_k \ dx \\
& + \Delta t_k \int_\Omega \left(\frac{1}{3} \frac{\partial k}{\partial u}(u_k, \beta) \frac{\partial u_k}{\partial \beta} \nabla u_k + \left[\frac{1}{6} k(u_{k-1}, \beta) + \frac{1}{3} k(u_k, \beta) \right] \nabla \frac{\partial u_k}{\partial \beta} \right) \cdot \nabla v_k \ dx \\
& + \Delta t_k \int_\Omega c_{blood} \left(\frac{1}{3} \frac{\partial \omega}{\partial u}(u_k, \beta) \frac{\partial u_k}{\partial \beta} u_k + \left[\frac{1}{6} \omega(u_{k-1}, \beta) + \frac{1}{3} \omega(u_k, \beta) \right] \frac{\partial u_k}{\partial \beta} \right) v_k \ dx \\
& - \Delta t_k \int_\Omega \frac{c_{blood}}{2} \frac{\partial \omega}{\partial u}(u_k, \beta) \frac{\partial u_k}{\partial \beta} u_a v_k \ dx + \Delta t_k \int_{\partial \Omega_C} \frac{h}{2} \frac{\partial u_k}{\partial \beta} v_k \ dA \\
-\Delta t_k \ \int_\Omega & \frac{\rho c_p}{\Delta t_k} \frac{\partial u_{k-1}}{\partial \beta} v_k + \frac{1}{6} \frac{\partial k}{\partial u}(u_{k-1}, \beta) \frac{\partial u_{k-1}}{\partial \beta} \nabla u_k \cdot \nabla v_k \frac{1}{6} \frac{\partial \omega}{\partial u}(u_{k-1}, \beta) \frac{\partial u_{k-1}}{\partial \beta} u_k v_k \ dx \\
& + \Delta t_k \ \int_\Omega \left(\frac{1}{3} \frac{\partial k}{\partial u}(u_{k-1}, \beta) \frac{\partial u_{k-1}}{\partial \beta} \nabla u_{k-1} + \left[\frac{1}{3} k(u_{k-1}, \beta) + \frac{1}{6} k(u_k, \beta) \right] \nabla \frac{\partial u_{k-1}}{\partial \beta} \right) \cdot \nabla v_k \ dx \\
& + \Delta t_k \int_\Omega c_{blood} \left(\frac{1}{3} \frac{\partial \omega}{\partial u}(u_{k-1}, \beta) \frac{\partial u_{k-1}}{\partial \beta} u_{k-1} + \left[\frac{1}{3} \omega(u_{k-1}, \beta) + \frac{1}{6} \omega(u_k, \beta) \right] \frac{\partial u_{k-1}}{\partial \beta} \right) v_k \ dx \\
& - \Delta t_k \int_\Omega \frac{c_{blood}}{2} \frac{\partial \omega}{\partial u}(u_{k-1}, \beta) \frac{\partial u_{k-1}}{\partial \beta} u_a v_k \ dx + \Delta t_k \int_{\partial \Omega_C} \frac{h}{2} \frac{\partial u_{k-1}}{\partial \beta} v_k \ dA \\
+\Delta t_k \int_\Omega & \left(\left[\frac{1}{3} \frac{\partial k}{\partial \beta}(u_{k-1}, \beta) + \frac{1}{6} \frac{\partial k}{\partial \beta}(u_k, \beta) \right] \nabla u_{k-1} + \left[\frac{1}{6} \frac{\partial k}{\partial \beta}(u_{k-1}, \beta) + \frac{1}{3} \frac{\partial k}{\partial \beta}(u_k, \beta) \right] \nabla u_k \right) \cdot \nabla v_k \ dx \\
+\Delta t_k \int_\Omega & c_{blood} \left(\left[\frac{1}{3} \frac{\partial \omega}{\partial \beta}(u_{k-1}, \beta) + \frac{1}{6} \frac{\partial \omega}{\partial \beta}(u_k, \beta) \right] u_{k-1} + \left[\frac{1}{6} \frac{\partial \omega}{\partial \beta}(u_{k-1}, \beta) + \frac{1}{3} \frac{\partial \omega}{\partial \beta}(u_k, \beta) \right] u_k \right) v_k \ dx \\
-\Delta t_k \int_\Omega & c_{blood} \left(\frac{\frac{\partial \omega}{\partial \beta}(u_{k-1}, \beta) + \frac{\partial \omega}{\partial \beta}(u_k, \beta)}{2} \right) u_a \ v_k \ dx - \Delta t_k \ \int_\Omega \frac{\partial Q_{laser}}{\partial \beta}(\mathbf{x}, t_k, \beta) v_k \ dx = 0 \qquad k = 1, 2, ..., N_{step}
\end{aligned}$$

Notice that solving for p_k such that

$$\begin{aligned}
\Delta t_k \ \int_\Omega & \frac{\rho c_p}{\Delta t_k} \hat{u} p_k + \frac{1}{6} \frac{\partial k}{\partial u}(u_k, \beta) \hat{u} \nabla u_{k-1} \cdot \nabla p_k + \frac{1}{6} \frac{\partial \omega}{\partial u}(u_k, \beta) \hat{u} u_{k-1} p_k \ dx \\
& + \Delta t_k \int_\Omega \left(\frac{1}{3} \frac{\partial k}{\partial u}(u_k, \beta) \hat{u} \nabla u_k + \left[\frac{1}{6} k(u_{k-1}, \beta) + \frac{1}{3} k(u_k, \beta) \right] \nabla \hat{u} \right) \cdot \nabla p_k \ dx \\
& + \Delta t_k \int_\Omega c_{blood} \left(\frac{1}{3} \frac{\partial \omega}{\partial u}(u_k, \beta) \hat{u} u_k + \left[\frac{1}{6} \omega(u_{k-1}, \beta) + \frac{1}{3} \omega(u_k, \beta) \right] \hat{u} \right) p_k \ dx \\
& - \Delta t_k \int_\Omega \frac{c_{blood}}{2} \frac{\partial \omega}{\partial u}(u_k, \beta) \hat{u} u_a p_k \ dx + \Delta t_k \int_{\partial \Omega_C} \frac{h}{2} \hat{u} p_k \ dA \\
& = \Delta t_k \int_\Omega \rho c_p \chi(\mathbf{x}) \left[\frac{1}{6}(u_{k-1} - u_{k-1}^{exp}) - \frac{1}{3}(u_k - u_k^{exp}) \right] \hat{u} \forall \hat{u}, \qquad k = N_{step}
\end{aligned}$$

and

$$
\begin{aligned}
&\Delta t_k \int_\Omega \frac{\rho c_p}{\Delta t_k}\hat{u}p_k + \frac{1}{6}\frac{\partial k}{\partial u}(u_k,\beta)\hat{u}\nabla u_{k-1}\cdot\nabla p_k + \frac{1}{6}\frac{\partial \omega}{\partial u}(u_k,\beta)\hat{u}u_{k-1}p_k \; dx \\
&\quad + \Delta t_k \int_\Omega \left(\frac{1}{3}\frac{\partial k}{\partial u}(u_k,\beta)\hat{u}\nabla u_k + \left[\frac{1}{6}k(u_{k-1},\beta) + \frac{1}{3}k(u_k,\beta)\right]\nabla\hat{u}\right)\cdot\nabla p_k \; dx \\
&\quad + \Delta t_k \int_\Omega c_{blood}\left(\frac{1}{3}\frac{\partial \omega}{\partial u}(u_k,\beta)\hat{u}u_k + \left[\frac{1}{6}\omega(u_{k-1},\beta) + \frac{1}{3}\omega(u_k,\beta)\right]\hat{u}\right)p_k \; dx \\
&\quad - \Delta t_k \int_\Omega \frac{c_{blood}}{2}\frac{\partial \omega}{\partial u}(u_k,\beta)\hat{u}u_a p_k \; dx + \Delta t_k \int_{\partial\Omega_C} \frac{h}{2}\hat{u}p_k \; dA \\
&\quad = \int_\Omega \rho c_p \chi(\mathbf{x}) \begin{pmatrix} \Delta t_k \left[\frac{1}{6}(u_{k-1} - u_{k-1}^{exp}) + \frac{1}{3}(u_k - u_k^{exp})\right]\hat{u} \\ + \Delta t_{k+1}\left[\frac{1}{3}(u_k - u_k^{exp}) + \frac{1}{6}(u_{k+1} - u_{k+1}^{exp})\right] \end{pmatrix} \hat{u} \; dx \\
&\qquad - \begin{pmatrix}
-\Delta t_{k+1} \displaystyle\int_\Omega \begin{pmatrix} \frac{\rho c_p}{\Delta t_{k+1}}\hat{u}p_{k+1} \\ + \frac{1}{6}\frac{\partial k}{\partial u}(u_k,\beta)\hat{u}\nabla u_{k+1}\cdot\nabla p_{k+1} \\ + \frac{1}{6}\frac{\partial \omega}{\partial u}(u_k,\beta)\hat{u}u_{k+1}p_{k+1} \end{pmatrix} dx \\
+ \Delta t_{k+1} \displaystyle\int_\Omega \begin{pmatrix} \frac{1}{3}\frac{\partial k}{\partial u}(u_k,\beta)\hat{u}\nabla u_k \\ + \begin{bmatrix} \frac{1}{3}k(u_k,\beta) \\ + \frac{1}{6}k(u_{k+1},\beta) \end{bmatrix} \nabla\hat{u} \end{pmatrix} \cdot\nabla p_{k+1} \; dx \\
+ \Delta t_{k+1} \displaystyle\int_\Omega c_{blood} \begin{pmatrix} \frac{1}{3}\frac{\partial \omega}{\partial u}(u_k,\beta)\hat{u}u_k \\ + \begin{bmatrix} \frac{1}{3}\omega(u_k,\beta) \\ + \frac{1}{6}\omega(u_{k+1},\beta) \end{bmatrix} \hat{u} \end{pmatrix} p_{k+1} \; dx \\
- \Delta t_{k+1} \displaystyle\int_\Omega \frac{c_{blood}}{2}\frac{\partial \omega}{\partial u}(u_k,\beta)\hat{u}u_a p_{k+1} \; dx \\
+ \Delta t_{k+1} \displaystyle\int_{\partial\Omega_C} \frac{h}{2}\hat{u}p_{k+1} \; dA
\end{pmatrix} \\
&\qquad\qquad \forall \hat{u}, \qquad k = N_{step}-1, N_{step}-2, ..., 1
\end{aligned}
$$

implies that

$$\frac{\partial Q(u,\beta)}{\partial \beta} = \sum_{k=1}^{N_{step}} \left(\begin{array}{c} -\Delta t_k \int_\Omega \left(\begin{array}{c} \left[\begin{array}{c} \frac{1}{3}\frac{\partial k}{\partial \beta}(u_{k-1},\beta) \\ +\frac{1}{6}\frac{\partial k}{\partial \beta}(u_k,\beta) \end{array} \right] \nabla u_{k-1} \\ + \left[\begin{array}{c} \frac{1}{6}\frac{\partial k}{\partial \beta}(u_{k-1},\beta) \\ +\frac{1}{3}\frac{\partial k}{\partial \beta}(u_k,\beta) \end{array} \right] \nabla u_k \end{array} \right) \cdot \nabla p_k \; dx \\ -\Delta t_k \int_\Omega c_{blood} \left(\begin{array}{c} \left[\begin{array}{c} \frac{1}{3}\frac{\partial \omega}{\partial \beta}(u_{k-1},\beta) \\ +\frac{1}{6}\frac{\partial \omega}{\partial \beta}(u_k,\beta) \end{array} \right] u_{k-1} \\ + \left[\begin{array}{c} \frac{1}{6}\frac{\partial \omega}{\partial \beta}(u_{k-1},\beta) \\ +\frac{1}{3}\frac{\partial \omega}{\partial \beta}(u_k,\beta) \end{array} \right] u_k \end{array} \right) p_k \; dx \\ +\Delta t_k \int_\Omega \frac{c_{blood}}{2} \left(\frac{\partial \omega}{\partial \beta}(u_{k-1},\beta) + \frac{\partial \omega}{\partial \beta}(u_k,\beta) \right) u_a \; p_k \; dx \\ +\Delta t_k \int_\Omega \frac{\partial Q_{laser}}{\partial \beta}(\mathbf{x},t_k,\beta) p_k \; dx \end{array} \right)$$

Algorithm C.2 Sum Factorization

```
$A(:,:,:,:,:,:) = ZERO$
for $i1 = 0, 1, 2, ..., p_x$ do
  for $j1 = 0, 1, 2, ..., p_x$ do
    for $n = 0, 1, 2, ..., p_z$ do
      for $m = 0, 1, 2, ..., p_y$ do
        for $l = 0, 1, 2, ..., p_x$ do
          $A^1_{aux}(i1, j1, m, n) = A^1_{aux}(i1, j1, m, n) + D(\xi_{1,l}, \xi_{2,m}, \xi_{3,n})\ \phi_{i_1}(\xi_{1,l})\chi_{j_1}(\xi_{1,l})$
        end for
        for $i2 = 0, 1, 2, ..., p_y$ do
          for $j2 = 0, 1, 2, ..., p_y$ do
            $A^2_{aux}(i1, j1, i2, j2, n) = A^2_{aux}(i1, j1, i2, j2, n) + A^1_{aux}(i1, j1, m, n)\ \phi_{i_2}(\xi_{2,m})\chi_{j_2}(\xi_{2,m})$
          end for
        end for
      end for
      for $i3 = 0, 1, 2, ..., p_z$ do
        for $j3 = 0, 1, 2, ..., p_z$ do
          for $i2 = 0, 1, 2, ..., p_y$ do
            for $j2 = 0, 1, 2, ..., p_y$ do
              $A(i1, j1, i2, j2, i3, j3) = A(i1, j1, i2, j2, i3, j3) + A^2_{aux}(i1, j1, i2, j2, n)\ \phi_{i_3}(\xi_{3,n})\chi_{j_3}(\xi_{3,n})$
            end for
          end for
        end for
      end for
    end for
  end for
end for
```

Appendix D

Relevant Cell Biology

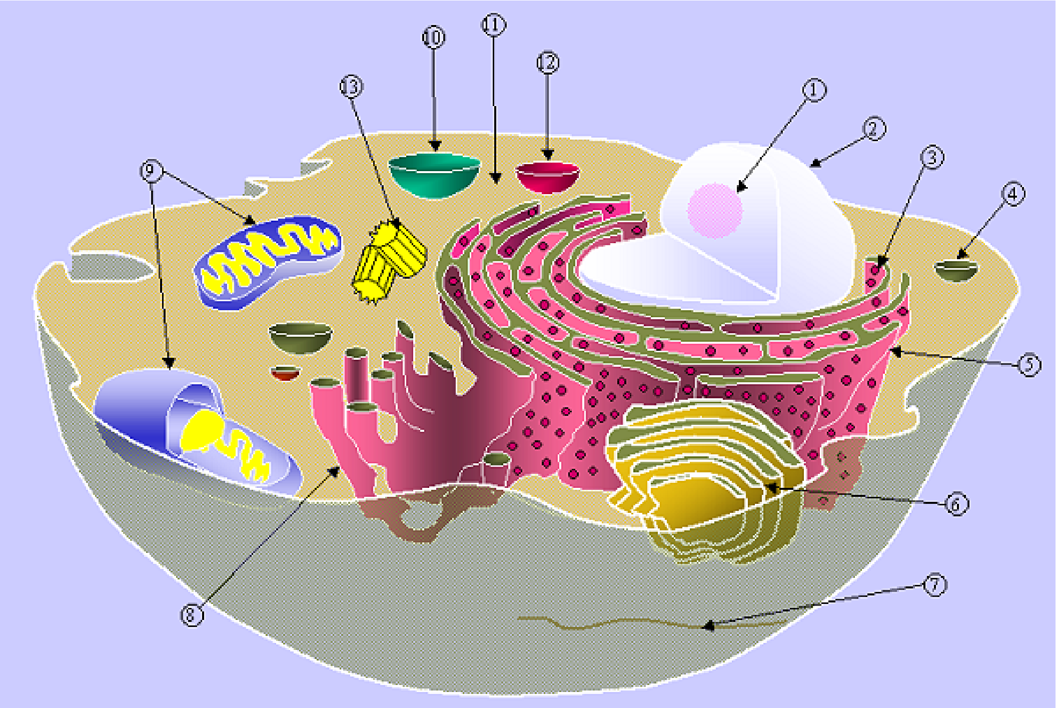

1. nucleolus
2.nucleus
3. ribosome
4. vesicle
5. rough endoplasmic reticulum (ER)
6. Golgi apparatus
7. Cytoskeleton
8. smooth ER
9. mitochondria
10. vacuole
11. cytoplasm
12. lyosome
13. centrioles

Figure D.1: Eucaryotic Cell. Image by Magnus Manske, reproduced under the terms of the GNU Free Documentation License.

A healthy body body is a strange society, wherein self-sacrifice as opposed to survival of the fittest is the rule. Somatic cells dedicate their existence to support germ cells, which are really the only cells that leave descendants. Cancerous cells defy the normals rules in that they proliferate without bound. A full appreciation of cancer cells and their relation to heat shock proteins, begins with the study of basic cellular biology.

The human body is composed of more than 10^{17} cells with more than 200 different types of cells, but within each cell the total genetic information embodied within its DNA sequence is exactly the same, otherwise known as the genome of the cell. Different cells come into being though different genes, which are particular segments of the DNA corresponding to a single protein through the process of transcription and translation, that are expressed within the cell. Transcription refers to the process by which DNA is copied to a complementary MRNA and translation refers to the process by which the sequence of nulceotides on and MRNA molecule encode the amino acid sequence of a protein through TRNA. Expression of individual genes is regulated within the cell, instead of manufacturing its full repertoire of possible proteins at full potential all the time, the cell adjusts the rates of transcription and translation as needed. The definition of a **cell** is as follows:

> *minuscule membrane-bound corpuscles filled with a concentrated aqueous solution of chemicals and endowed with an extraordinary ability to gather and utilize materials from their environment to create copies of themselves by growing and dividing in two. The copy has the exact same hereditary information.*

Figure D.1 shows a diagram of the constituents of a eucaryotic cell, that is a cell with an identifiable cell nucleus. Table D.1 compares the length scales of the cell to more familiar length scales. The order of magnitude of the length scale for the diameter of cells within the human body is roughly between 2 μm to 200 μm. Compared to the length scale of atoms, whose atomic radii is $\approx$ 0.2nm, and the average diameter of various molecules with diameters ranging from 0.2nm to 20.0nm, the size of a cell is rather large. As shown, within the cell membrane, approximately 5nm thick, exists smaller membrane bound entities identified as **organelles**. Using the language of chemical reactions, the organelles within the cell, each with a specific task, collectively work and interact with one another to generate life as it is known to mankind.

Table D.1: Length scale.

1 femtometre (fm)	size of a proton/classical electron radius
25 picometre (pm)	radius of hydrogen atom
154 pm (0.154 nm)	length of a typical covalent bond (CC).
500 pm (0.50 nm)	width of protein α helix
2 nanometre (nm)	diameter of DNA helix
3.4 nm	length of a DNA turn
24 nm	size of an albumin protein molecule
6 - 10 nm	thickness of cell membrane
20 nm	thickness of bacterial flagellum
40 nm	extreme ultraviolet wavelength
20 nm - 450 nm	viruses
100 nm	size of chromosomes
625-740 nm	wavelength of red light
1 micrometre (μm)	diameter of typical bacterium
68 μm	diameter of a human red blood cell
7 μm	diameter of the nucleus of typical eukariotic cell
80 μm	average width of human hair (ranges from 18 to 180 μm)
500 μm	typical length of Amoeba proteus, an amoeboid protist
5 millimetre (mm)	length of average red ant

A further division of the constituents of the cell would reveal that 70% of the total cellular mass is comprised of water and 28% can be attributed to the organic molecules: amino acids, fatty acids, nucleotides, and sugars. Of the organic molecules, proteins, composed of amino acids, constitute the majority of the dry mass of the cell. Proteins are the building blocks from which the cell is built. The cytoskeleton, made of proteins, serves as the bones and muscles of the cell. Proteins are embedded in the cell membranes and membranes of the organelles to allow a specific means of molecular transport. They carry messages between organelles and even between cells. Other proteins act as antibodies, toxins, hormones, elastic fibers, or even sources of light. The enzymes that catalyze the chemical reactions necessary for life are also proteins.

Study of the structure of proteins gives insight to understanding how proteins preform their multitude of tasks. A **protein** consists of chain of 30-10000 covalently bonded amino acids. However, the majority of proteins consist of 50-2000 amino acids. Amino acids are characterized as a class of molecules each possessing a carboxyl and amino group covalently bonded to a single carbon atom. The generic formula of an amino acid is shown in Figure D.2, ”R” represents 1 of the 20 different side chain of molecules that distinguish amino acids. Of the numerous amounts of amino acids a subset of 20 occur repeatedly in bacteria, plants, and animals; the exact reason these were chosen is an evolutionary mystery. The different side chains of the polypeptide back bone give

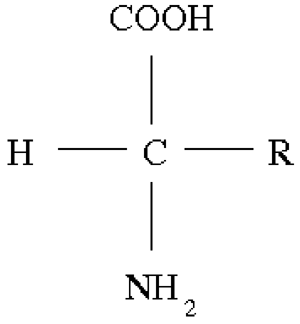

$$\begin{array}{c} COOH \\ | \\ H - C - R \\ | \\ NH_2 \end{array}$$

Figure D.2: Generic Amino Acid Structure.

the protein its unique three dimensional structure. The shape of the folded protein is determined by the noncovalent bonding of the side chains attached to the polypeptide backbone, Figure D.3.

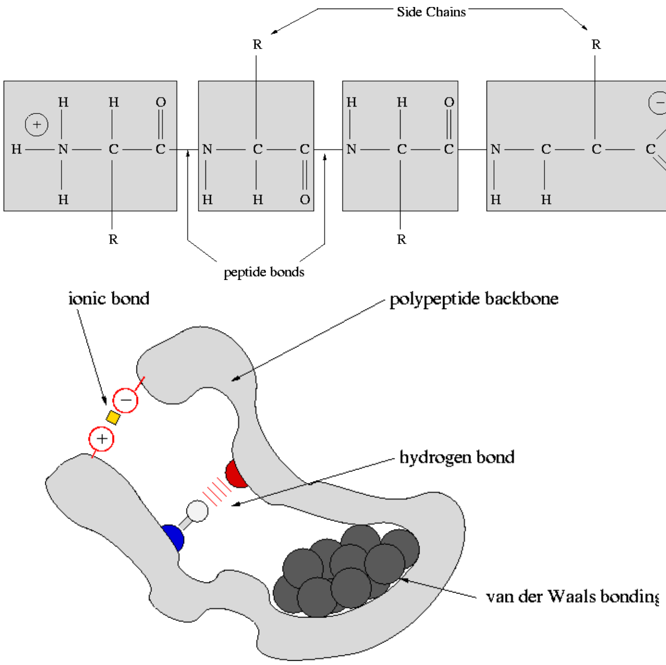

Figure D.3: Protein Structure.

The initial appearance of the three dimensional conformation of the protein appears to be random. However a closer look reveals that the shape of the protein is absolutely essential to its biological function. As an example consider the cartoon shown in Figure D.4. Suppose that the molecule labeled ”A” is a binding site of an antibody, meaning its job is to bind to a specific germ or antigen within the body signaling the immune system for its destruction. Also suppose that the molecules labeled ”B”, ”C”, and ”D” are the antigen. The strong covalent bonds withstand the molecular collisions of thermal motion, but many non-covalent bonds must occur for the antibody to

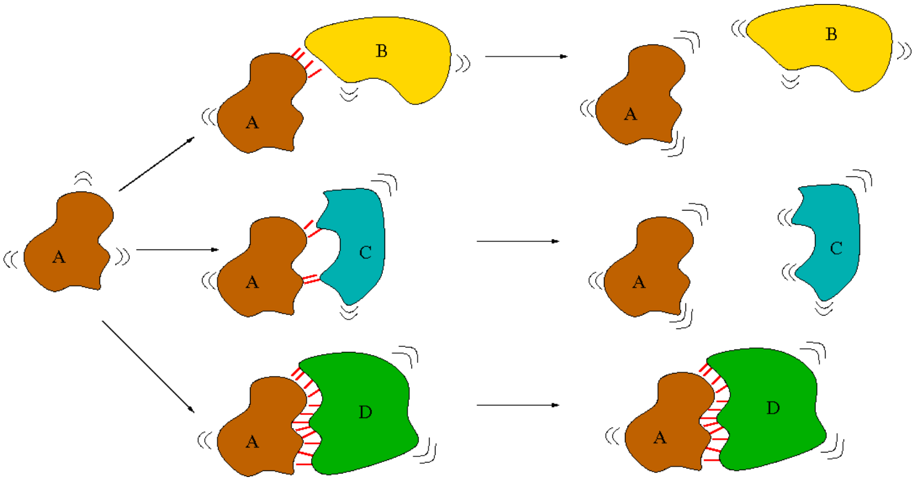

Figure D.4: Noncovalent binding.

bind with the antigen; the shape of the binding site and antigen determine the quantity of non-covalent bonds that may form. The relative strength of the different bonds is quantified in the Table D.2. A bond strength of 1 kcal/mole implies that 1 kilocalorie of energy must be supplied to break 6×10^{23} of these bonds.

Table D.2: Bond Strengths

bond type	length (nm)	strength in vacuum (kcal/mole)	strength in water (kcal/mole)
covalent	0.15	90	90
non-covalent: ionic	0.25	80	3
non-covalent: hydrogen	0.30	4	1
non-covalent: van der Waals	0.35	0.1	0.1

Bibliography

[1] National Cancer Institute. www.cancer.gov.

[2] T. Arbogast and J. Bona. Methods of applied mathematics. University of Texas at Austin, Dept. of Mathematics, Applied Mathematics Course Notes, 2004.

[3] Satish Balay, William D. Gropp, Lois C. McInnes, and Barry F. Smith. Petsc users manual. Technical Report ANL-95/11 - Revision 2.1.5, Argonne National Laboratory, 2003.

[4] W. Bangerth and R. Rannacher. *Adaptive Finite Element Methods for Solving Differential Equations.* Birkhäuser Verlag, 2003.

[5] Roland Becker and Rolf Rannacher. An optimal control approach to a posteriori error estimation in finite element methods. *Acta Numerica*, 10:1–102, 2001.

[6] Steven J. Benson, Lois Curfman McInnes, Jorge Moré, and Jason Sarich. TAO user manual (revision 1.8). Technical Report ANL/MCS-TM-242, Mathematics and Computer Science Division, Argonne National Laboratory, 2005. http://www.mcs.anl.gov/tao.

[7] M. Braack and A. Ern. A posteriori control of modeling errors and discretization errors. *Multiscale Model. Simul.*, 1:221–238, 2003.

[8] American Cancer Society. *Cancer Facts and Figures 2007.* Atlanta: American Cancer Society, 2007.

[9] C. K. Charny and R. L. Levin. Bioheat transfer in a branching countercurrent network during hyperthermia. *J. Biomech. Eng.*, 111:263–270, 1989.

[10] C. K. Charny, S. Weinbaum, and R. L. Levin. An evaluation of the Weinbaum-Jiji bioheat equation for normal and hyperthermia conditions. *J. of Biomechanical Eng.-Transactions of the ASME*, 112:80–87, 1990.

[11] C.K. Charny. Mathematical models of bioheat transfer. *Adv. Heat Trans.*, 22:19–155, 1992.

[12] J.C. Chato. Heat transfer to blood vessels. *ASME J. Biomech. Eng.*, 102:110, 1980.

[13] M.M. Chen and K.R. Holmes. Microvascular contributions in tissue heat transfer. *Ann. N.Y. Acad. Sci.*, 335:137, 1980.

[14] F. Darema. DDDAS: Dynamic data driven applications systems. website: www.nsf.gov/cise/cns/dddas.

[15] L. Demkowicz. Projection-based interpolation. *ICES Report*, 04-03, 2004.

[16] L. Demkowicz. *Computing with hp-Adaptive Finite Elements: Volume 1-One and Two Dimensional Elliptic and Maxwell Problems.* Chapman & Hall/CRC Applied Sciences, 2007.

[17] W.C. Dewey, M.L. Freeman, G.P. Raaphorst, E.P. Clark, R.S.L Wond, and D.P. Highfield. Cell biology of hyperthermia and radiation. In R.E. Meyn and H.R. Withers, editors, *Radiation Biology in Cancer Research*, pages 589–621, New York, 1980. Raven Press.

[18] K. R. Diller, J. W. Valvano, and J. A. Pearce. Bioheat transfer. In F. Kreith and Y. Goswami, editors, *The CRC Handbook of Mechanical Engineering, 2nd Ed.*, pages 4–278–4–357. CRC Press, Boca Raton, 2005.

[19] A. Ern and J.L. Guermond. *Theory and Practice of Finite Elements.* Springer Verlag, 2004.

[20] Y. Feng, J.T. Oden, and M.N. Rylander. A statistical thermodynamics based cell damage models and its validation in vitro. *J. Biomech. Eng.*, Accepted for publication, 2007.

[21] Advanced Visual Systems Inc. AVS user's guide, May 1992. National Congress on Computational Mechanics. San Francisco, California, Conference Presentation.

[22] L.M. Jiji, S. Weinbaum, and D.E. Lemons. Theory and experiment for the effect of vascular microstructure on surface tissue heat transfer. part ii. model formulation and solution. *ASME J. Biomech. Eng.*, 106:333, 1984.

[23] M. Kangasniemi et al. Dynamic gadolinium uptake in thermally treated canine brain tissue and experimental cerebral tumors. *Invest. Radiol.*, 38(2):102–107, 2003.

[24] H.B. Klinger. Heat transfer in perfused biological tissue. I. General Theory. *Bull. Math. Biol.*, 36:403, 1974.

[25] J. Kurtz. *Fully Automatic hp-Adaptivity for Acoustic and Electromagnetic Scattering in Three Dimensions.* PhD thesis, The University of Texas at Austin, May 2007.

[26] J. T. Oden, K. R. Diller, C. Bajaj, J. C. Browne, J. Hazle, I. Babuška, J. Bass, L. Demkowicz, Y. Feng, D. Fuentes, S. Prudhomme, M. N. Rylander, R. J. Stafford, and Y. Zhang. Dynamic data-driven finite element models for laser treatment of prostate cancer. *Num. Meth. PDE,*, Accepted for publication, 2007.

[27] J. T. Oden and S. Prudhomme. Goal-oriented error estimation and adaptavity for the finite element method. *Computers and Mathematics with Applications*, 41(5–6):735–756, 2001.

[28] J. T. Oden and S. Prudhomme. Estimation of modeling error in computational mechanics. *Journal of Computational Physics*, 182:496–515, 2002.

[29] J. T. Oden, S. Prudhomme, D. C. Hammerand, and M. S. Kuczma. Modeling error and adaptivity in nonlinear continuum mechanics. *Comput. Meth. Appl. Mech. Engrg.*, 190:6663–6684, 2001.

[30] J. T. Oden and K. Vemaganti. Adaptive hierarchical modeling of heterogeneous structures. Predictability: quantifying uncertainty in models of complex phenomena. *Phys. D*, 133:404–415, 1999.

[31] J. T. Oden and Tarek I. Zohdi. Analysis and adaptive modeling of highly heterogeneous elastic structures. *Comput. Methods Appl. Mech. Eng.*, 148(3–4):367–391, 1997.

[32] H. H. Pennes. Analysis of tissue and arterial blood temperatures in the resting forearm. *J. Appl. Physiol.*, 1:93–122, 1948.

[33] Serge Prudhomme and J. T. Oden. On goal-oriented error estimation for elliptic problems: Applications to the control of pointwise errors. *Comput. Methods Appl. Mech. Eng.*, 176:313–331, 1999.

[34] R. B. Roemer and A. W. Dutton. A generic tissue convective energy balance equation: Part 1 - Theory and Derivation. *J. Biomech. Eng.*, 120:395–404, 1998.

[35] R.B. Roemer. Engineering aspects of hyperthermia therapy. In *Ann. Rev. Biomed. Eng*, pages 347–376. Annual Review, 1999.

[36] M.N. Rylander. *Design of Hyperthermia Protocols for Inducing Cardiac Protection and Tumor Destruction by Controlling Heat Shock Protein Expression.* PhD thesis, The University of Texas at Austin, 2005.

[37] R. Salomir et al. Hyperthermia by MR-guided focused ultrasound: accurate temperature control based on fast MRI and a physical model of local energy deposition and heat conduction. *Magn. Reson. Med.*, 43(3):342–347, 2000.

[38] K. Shinohara. Thermal ablation of prostate diseases: advantages and limitations. *Int. J. Hyperthermia*, 20(7):679–697, 2004.

[39] R.E. Showalter. *Monotone Operators in Banach Space and Nonlinear Partial Differential Equations.* American Mathematical Society, 1997.

[40] D.U. Silverthorn. *Human Physiology: An Integrated Approach.* Pearson Education, 3 edition, 2004.

[41] V. Thommee. *Galerkin Finite Element Methods for Parabolic Problems.* Springer Verlag, 1984.

[42] J.W. Valvano and et al. An isolated rat liver model for the evaluation of thermal techniques to measure perfusion. *ASME J. Biomech. Eng.*, 106:187–191, 1984.

[43] F. C. Vimeux et al. Real-time control of focused ultrasound heating based on rapid MR thermometry. *Invest. Radiol.*, 34(3):190–193, 1999.

[44] S. Weinbaum, L.M. Jiji, and D.E. Lemons. Theory and experiment for the effect of vascular microstructure on surface tissue heat transfer. part i. anatomical foundation and model conceptualization. *ASME J. Biomech. Eng.*, 106:321, 1984.

[45] A. J. Welch and M. J. C. van Gemert. *Optical-Thermal Response of Laser-Irradiated Tissue.* New York: Plenum Press, 1995.

[46] E. H. Wissler. Pennes' 1948 paper revisited. *J. Appl. Physiol.*, 85:35–41, 1998.

[47] W. Wulff. The energy conservation equation for living tissue. *IEEE Trans. Biomed. Eng.*, BME-21:494–495, 1974.

[48] L. Xu, M.M. Chen, K.R. Holmes, and H. Arkin. The evaluation of the pennes, the chen-holmes, the weinbaum-jiji bioheat transfer models in the pig kidney vortex. *ASME HTD*, 189:15–21, 1991.

[49] Tarek I. Zohdi, J. Tinsley Oden, and G. J. Rodin. Hierarchical modeling of heterogeneous bodies. *Comput. Methods Appl. Mech. Eng.*, 138:273–298, 1996.

Vita

David Fuentes was born in Galveston, Texas on 10 May 1981, the son of David A. Fuentes and Norma G. Fuentes. He graduated high school in May of 1999 and immediately began pursuit of a college degree in June of 1999. He received the Bachelor of Science degree in Aerospace Engineering in December 2002 from the University of Texas at Austin. He began graduate studies in January 2003 and received a Master of Science in Computational and Applied Mathematics in August 2005.

Permanent address: 5001 Ave. R$\frac{1}{2}$ Galveston, Texas 77551

This dissertation was typeset with LaTeX[†] by the author.

[†] LaTeX is a document preparation system developed by Leslie Lamport as a special version of Donald Knuth's TeX Program.